Structural Basis for Protein Recognition, Acyl-substrate Delivery, and Product Release by ACP in the Biosynthesis of Lipid A

by

S. Ali Masoudi

Department of Biochemistry
Duke University

Date:_______________________

Approved:

____
Pei Zhou, Co-supervisor

____
Richard Brennan, Co-supervisor

____
K.V. Rajagopalan

____
Meta J. Kuehn

____
M. Stephen Trent

____
Charles W. Pemble, IV

Dissertation submitted in partial fulfillment of
the requirements for the degree of
Doctor of Philosophy
in the Department of Biochemistry in the Graduate School
of Duke University
2014

ABSTRACT

Structural Basis for Protein Recognition, Acyl-substrate Delivery, and Product Release by ACP in the Biosynthesis of Lipid A

by

S. Ali Masoudi

Department of Biochemistry
Duke University

Date:_______________________

Approved:

____
Pei Zhou, Co-supervisor

____
Richard Brennan, Co-supervisor

____
K.V. Rajagopalan

____
Meta J. Kuehn

____
M. Stephen Trent

____
Charles W. Pemble, IV

An abstract of a dissertation submitted in partial fulfillment
of the requirements for the degree of Doctor of Philosophy in the
Department of Biochemistry in the Graduate School
of Duke University
2014

Abstract

Acyl-carrier-protein (ACP) is the principal transporter of fatty acids, coordinating acyl-transfer among a vast network of diverse enzymes and biochemical processes. ACP association with protein partners is thought to be exceedingly transient. This paradigm has posed challenges for understanding the molecular basis for acyl-delivery and dissociation. During biosynthesis of the lipid A component (endotoxin) of lipopolysaccharides, ACP shuttles acyl-intermediates thioester-linked to its 4′-phosphopantetheine arm among four acyltransferases: LpxA, LpxD, LpxL, and LpxM. LpxA and LpxD are essential cytoplasmic enzymes, which not only provide an excellent model system to study the ACP-based interaction, but also offer an important therapeutic target for development of novel antibiotics. This dissertation reports the crystal structures of three forms of *Escherichia coli* ACP engaging LpxD, which represent stalled substrate and breakage products along the reaction coordinate. The structures reveal the intricate interactions at the interface that optimally position ACP for acyl-delivery and directly involve the pantetheinyl group. Conformational differences among the stalled ACPs provide the molecular basis for the association-dissociation process. An unanticipated conformational shift of 4′-phosphopantetheine groups within the LpxD catalytic chamber reveals an unprecedented role of ACP in product release. Moreover, the crystal structure of *E. coli* LpxA in complex with one form of ACP (*holo*-ACP) is presented. The structure reveals three molecules of *holo*-ACP localize to the C-terminal domain of the LpxA homotrimer, and shows the functional role of this domain is two-fold: ACP recognition and nucleotide binding of UDP-GlcNAc. A comparison with the LpxD:ACP complexes uncovers that ACP utilizes different surface residues for recognition even amongst closely related acyltransferases, yet still relies on "electrostatic steering" for docking to its enzyme partner. Insights gleaned from the presented structures have provided not only a better understanding of ACP interaction with acyltransferases, but also has identified the "drugable molecular landscape" for the development of novel antibiotics against infective Gram-negative bacteria.

Table of Contents

List of Tables

List of Figures

List of Abbreviations

4′-PPT, 4'-phosphopantetheine

AasS: soluble acyl-ACP synthetase

ACP, acyl-carrier-protein

ACPS: holo-ACP synthase

ARD, ACP recognition domain

ATP, adenosine triphosphate

CD14, cluster differentiation antigen 14

CoA, coenzyme A

CTD, C-terminal domain

CtLpxD, *Chlamydia trachomatis* LpxD

DH, dehydratase

DTT, dithiothreitol

EcLpxD, *Escherichia coli* LpxD

ER, β-enoyl reductase

HEPES, 4-(2-hydroxyethyl)-1-piperazineethanesulfonic acid

IC_{50}, half maximal inhibitory concentration

IFN, interferon

IRF3, interferon response factor 3

k_B, Boltzmann constant

K_d, dissociation constant

K_i, inhibitory constant

K_M, Michaelis constant

Kdo, 3-deoxy-D-*manno*-oct-2-ulosonic acid

KR, β-ketoacyl reductase

KS, β-ketoacyl synthase

LβH, left-handed β-helix

LBP, LPS-binding protein

LPS, lipopolysaccharide

Lpt protein, LPS transport protein

MAL, MyD88-adaptor-like

MAT, malonyl/acetyl-CoA–ACP transacylase

MyD88, myeloid differentiation primary response protein 88

MD2, Myeloid differentiation factor 2

MES, 2-(N-morpholino)ethanesulfonic acid

MPD, 2-methyl-2,4-pentanediol

N-linked, amide-linked

NaCl, Sodium Chloride

NADPH, nicotinamide adenine dinucleotide phosphate (reduced)

NF-κB, nuclear factor κ-B

NTD, N-terminal domain

O-linked, ester-linked

PEG, polyethylene glycol

R-3OH-C10-ACP, *R*-3-hydroxydecanoyl-ACP

R-3OH-C12-ACP, *R*-3-hydroxylauroyl-ACP

R-3OH-C14-ACP, *R*-3-hydroxymyristoyl-ACP

R-3-OH-C16-ACP, R-3-hydroxypalmitoyl-ACP

RMSD, root-mean-square deviation

SDS-PAGE, Sodium dodecyl sulfate-polyacrylamide gel electrophoresis

TCEP, tris(2-chloroethyl) phosphate

TIR, toll/interleukin (IL)-1 receptor

TLC, thin-layer chromatography

TLR4, toll-like receptor 4

TLS, translation/liberation/screw

TNF-α, tumor necrosis factor-α

TRAM, TRIF-related adaptor molecule

TRIF, TIR domain-containing adaptor inducing interferon-β

Tris, 2-amino-2-(hydroxymethyl)-1,3-propanediol

UBD, uridine binding domain

UDP, uridine diphosphate

UDP-3-*O*-acyl-GlcN, UDP-3-*O*-(*R*-3-hydroxymyristoyl)-glucosamine

UDP-GlcNAc, UDP-*N*-acetylglucosamine

Acknowledgments

I would like to begin by thanking my advisor, Chris Raetz, who shaped the lipid field with his curiosity and efforts during his renowned career. He helped me to strengthen my interest in research by providing an intellectually challenging and motivating environment. I will be always grateful for his support and mentorship. Secondly, I would like to thank all of the members of the Raetz lab, especially Jinshi Zhao, Hak-Suk Chung, and Hayley Young for their scientific support and friendship. I would also like to extend my appreciation to my co-advisors, Pei Zhou and Dick Brennan, who have been truly supportive of the Raetz lab and me. To Pei Zhou and Dick Brennan, thank you so much for your mentorship and help throughout my graduate career. Special thanks to Charlie Pemble for his support and friendship. His scientific contribution was fundamental to the success of my research project. I am also thankful to Dr. Ziquiang Guan for the help with the mass spectrometry of ACP. Finally, I would like to thank my family, who has always supported my educational endeavors.

Crystal screening, data collection, and data processing were conducted in collaboration with the Duke Macromolecular X-ray Crystallography Shared Resource. Diffraction data were collected remotely at the Southeast Regional Collaborative Access Team 22-BM and 22-ID beamlines at the Advanced Photon Source, Argonne National Laboratory supported by the US Department of Energy, Office of Science, and the Office

of Basic Energy Sciences under Contract No. W-31-109-Eng-38. The NIH Grant GM-51310 awarded to Drs. C. R. H. Raetz and Pei Zhou supported this work.

Chapter 1. Introduction

1.1 Lipopolysaccharide and innate immune response

The cell envelope of Gram-negative bacteria is a complex structure that provides protection against internal turgor pressure and external stressors such as detergents and antibiotics (1, 2). This structural feature is characterized by the presence of an inner and an outer membrane that are separated by a thin layer of peptidoglycan and membrane-derived oligosaccharides (Fig. 1.1) (3, 4). The inner membrane bilayer as well as the inner monolayer of the outer membrane is composed mainly of phospholipids such as phosphatidylglycerol, and phosphatidylethanolamine, whereas the outer monolayer of the outer membrane is primarily made of lipopolysaccharide (LPS) (4). Gram-positive bacteria lack the outer membrane and alternatively possess a thicker layer of peptidoglycan. LPS of Gram-negatives is comprised of a hydrophilic and hydrophobic domain. The hydrophilic domain can be subdivided into two parts: distal O-antigen polysaccharide, and core oligosaccharide (4, 5). The O-antigen structure is highly variable among different Gram-negative serotypes. In *Escherichia coli*, for example, approximately 170 forms of O-antigen stereotypes have been identified (4). Conversely, variation in the composition and structure of core oligosaccharides within a given species is limited (4, 6). The O-antigen and core saccharides are not necessary for growth (7, 8); yet, they are needed for maintaining an effective permeability barrier and virulence (2, 9), and in their absence bacteria do not correctly insert porins (10, 11), and are more susceptible to antibiotics such as polymyxins (2, 12). The hydrophobic domain of LPS is a disaccharide glucosamine-based lipid, termed lipid A (endotoxin). With a few exceptions, lipid A is essential for bacterial growth and its structure is highly conserved (5, 8, 13-15). In *E. coli*, the diglucosamine backbone is decorated with two phosphoryl groups at positions 1 and 4′, and contains four primary and two secondary acyl-chains (Fig. 1.2) (5).

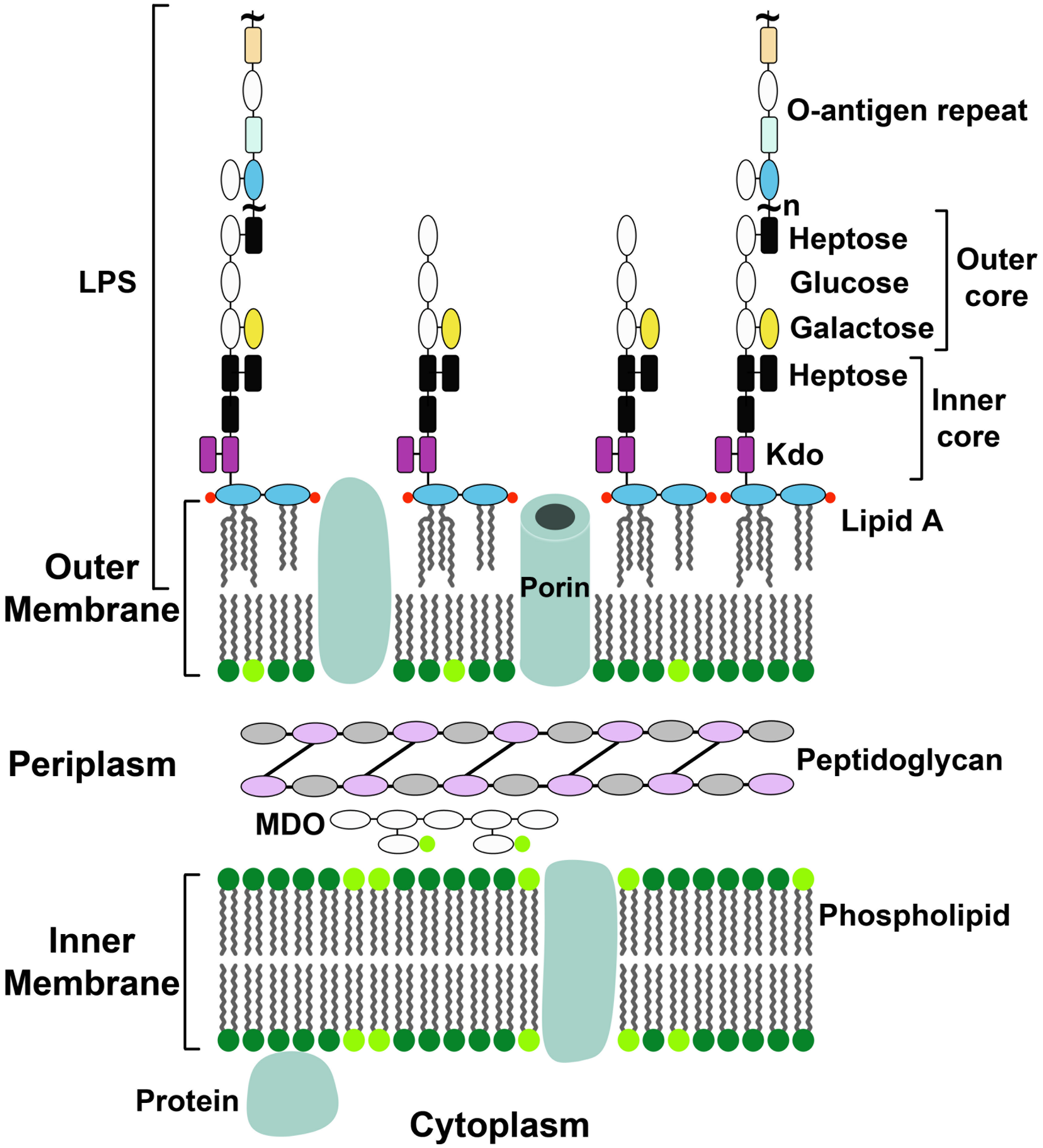
O-antigen repeat
n
LPS
Heptose
Glucose
Galactose
Outer core
Heptose
Inner core
Kdo
Lipid A
Outer Membrane
Porin
Periplasm
Peptidoglycan
MDO
Phospholipid
Inner Membrane
Protein
Cytoplasm

Figure 1.1: Schematic structure of the *E. coli* cell envelope. The cell envelope is composed of the inner and outer membranes separated by peptidoglycan and membrane-derived oligosaccharide (MDO). The inner membrane is comprised of phospholipids such as phosphatidylethanolamine (dark green) and phosphatidylglycerol (light green), and peripheral and integral membrane proteins (cyan). The inner leaflet of the outer membrane is composed mainly of phospholipids, whereas the outer leaflet is composed mostly of lipopolysaccharide (LPS). Lipid A is a hexa-acylated disaccharide that anchors LPS into the outer membrane. The inner core is linked to lipid A through a 3-deoxy-D-*manno*-oct-2-ulosonic acid sugar (Kdo) molecule. The composition of the O-antigen varies among Gram-negative serotypes. *E. coli* K-12 strains do not produce O-antigen except when a point mutation in the O-antigen operon is fixed. Kdo_2-lipid A is the minimal LPS structure sufficient for growth of Gram-negative bacteria.

Figure is adapted from Raetz and Reynolds 2007.

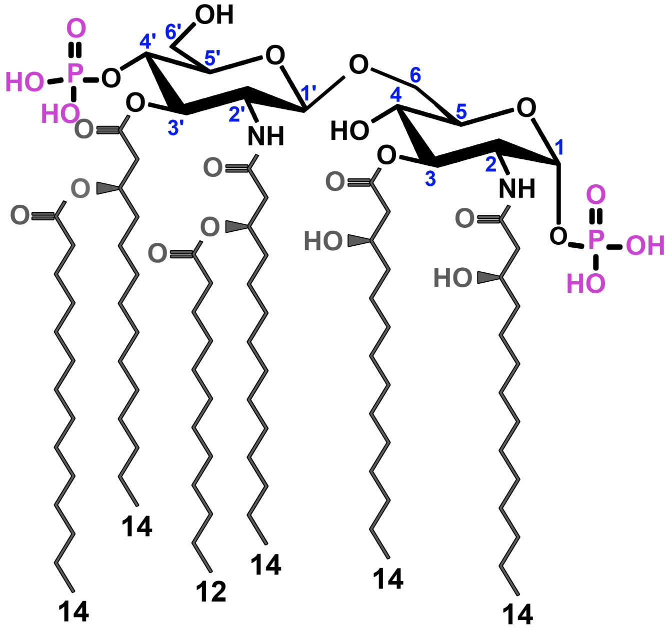

Figure 1.2: Chemical composition of *E. coli* lipid A. The lengths of attached acyl-chains are indicated. The glucosamine backbone can vary in some Gram-negative bacteria. In *Leptospira interrogans* and *Acidithiobacillus ferrooxidans* the acyl-chains at position 3 and 3′ are amide-linked instead of ester-linked. The length of acyl-chains can also vary in different bacteria. *Rhizobium leguminosarum*, and *Sinorhizobum meliloti* can incorporate a secondary acyl-chain at the 2′ position that measures 28-carbons in length. Lipid A can be modified after synthesis. For example, a phosphoethanolamine or an L-4-amino-4-deoxy-arabisone molecule can be added to the 1 and 4′ positions, respectively. In *Francisella tularensis* and various *Rhizhobium* species lipid A can be dephosphorylated.

During Gram-negative infection of the mammalian host, LPS is transferred to surface of monocytes, lymphocytes, and endothelial cells through the actions of LPS-binding protein (LBP), cluster differentiation antigen 14 (CD14), myeloid differentiation 2 (MD2), and toll-like receptor 4 (TLR4) to initiate a series of events that leads to production of inflammatory mediators and eventual clearance of infection (16-19). LPS is extracted from the surface of bacterium by LBP, and subsequently transferred to the phosphatidylinositol-anchored CD14 protein, and MD2/TLR4 complex (19). MD2 is a soluble protein that binds the extracellular domain of TLR4 to form a heterodimer (18). Upon recognition of lipid A moiety of LPS by MD2, the MD2/TLR4 complex dimerizes to form a $(\mathrm{LPS/MD2/TLR4})_2$ multimer. The crystal structure of $(\mathrm{LPS/MD2/TLR4\text{-}extracellular\ domain})_2$ multimer has been recently reported, which revealed the details of interactions between all subunits (Fig. 1.3a) (20). MD2 is predominantly composed of antiparallel β-strands and possesses a narrow hydrophobic pocket that is capable of accommodating five acyl-chains of lipid A (Fig 1.3b). The sixth acyl-chain interacts with a hydrophobic surface feature provided by the second TLR4 subunit, and the two phosphates of lipid A are coordinated by MD2 and two TLR4 subunits. The dimerization of MD2/TLR4 triggers the homodimerization of the intracellular toll/interleukin (IL)-1 receptor (TIR) domains of TLR4 subunits, which in turn activates two major signaling pathways (21). One pathway involves the recruitment of myeloid differentiation primary response protein 88 (MyD88) and MyD88-adaptor-like protein (MAL), and another response pathway involves TIR domain-containing adaptor inducing interferon-β (TRIF) and TRIF-related adaptor molecule (TRAM) (Fig. 1.4) (19, 22). The MyD88/MAL cascade signals through a kinase-dependent pathway, which leads to the activation and translocation of nuclear factor κ-B (NF-κB) to the nucleus where it induces the production of pro-inflammatory cytokines such as tumor necrosis factor α (TNF-α), interleukin 6 (IL-6), and IL-12. Overproduction of pro-inflammatory cytokines can lead to septic shock, a life-threatening clinical syndrome that can be characterized by organ dysfunction and failure, as well as severe blood pressure drop (4, 23).

The TRIF/TRAM signaling pathway is less inflammatory. This pathway leads to expression of interferon (IFN)-inducible genes through the activation of IFN regulatory factor 3 (IRF3), and results in adaptive immunity and adjuvanticity. The degree of acylation and phosphorylation of lipid A appears to affect the extent of pro-inflammatory response by TLR4/MD2 complex (24-26). Missing acyl or phosphate groups from the lipid A backbone compromises the dimerization of TLR4/MD2 complex and leads to partial activation of the TIR domain. For example, underacylated lipid A (lipid IV_A), and monophosphorylated lipid A act as partial agonists of human TLR4 to block pro-inflammatory cytokine production and promote adaptive immunity (27, 28). It is worth mentioning that monophosphorylated lipid A has been recently approved by US Food and Drug Agency to be used as vaccine adjuvant (28, 29).

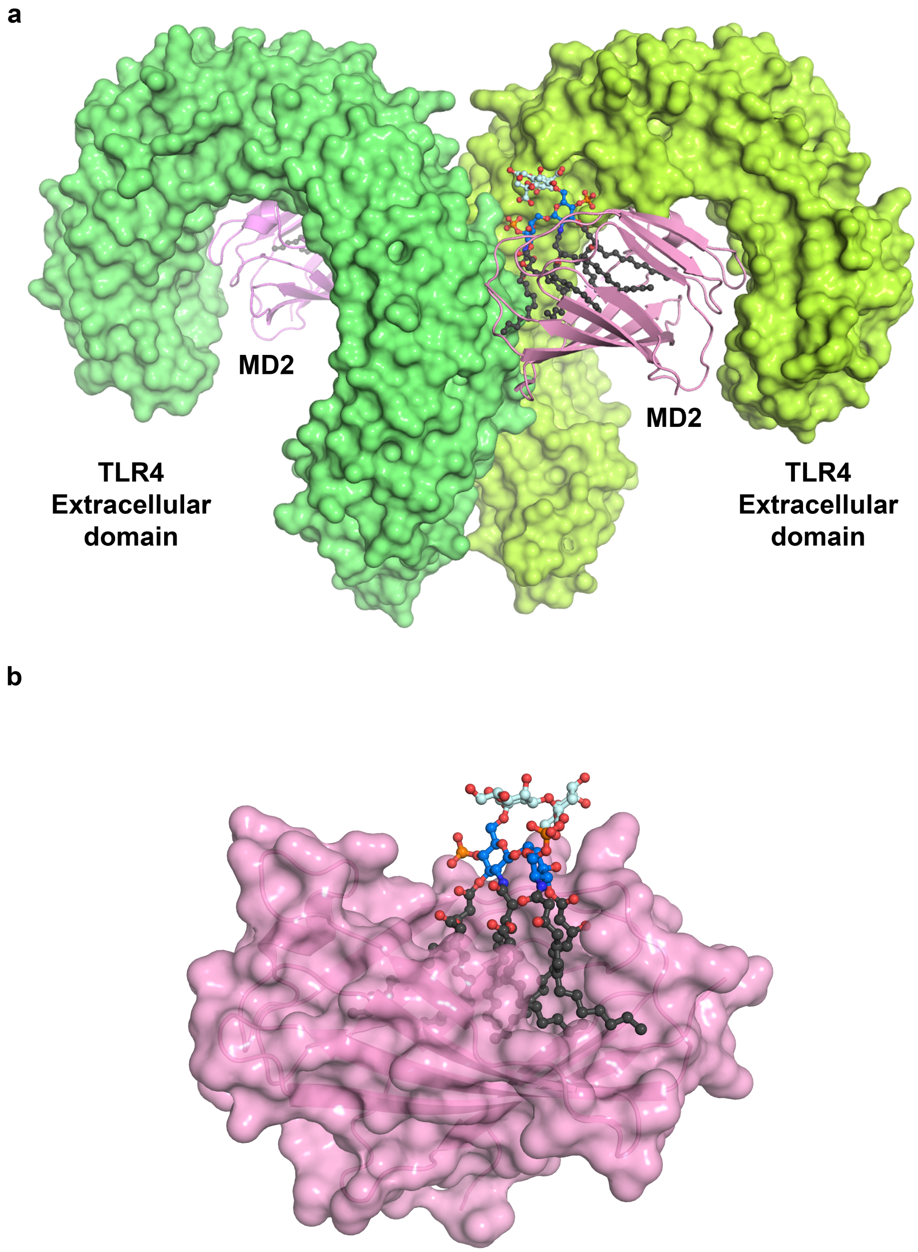

Figure 1.3: Structure of human TLR4/MD2 in complex with lipid A. **(a)** Kdo$_2$-lipid A bound to MD2 (pink) and the extracellular domain of TLR4 (green). The acyl-chains of Kdo$_2$-lipid A (ball and stick representation) are colored black, the glucosamine rings are in blue, and the Kdo$_2$ sugars are in light cyan and colored by atom. **(b)** The acyl-chains are packed inside MD2. The molecular surface of MD2 is shown with semitransparency.

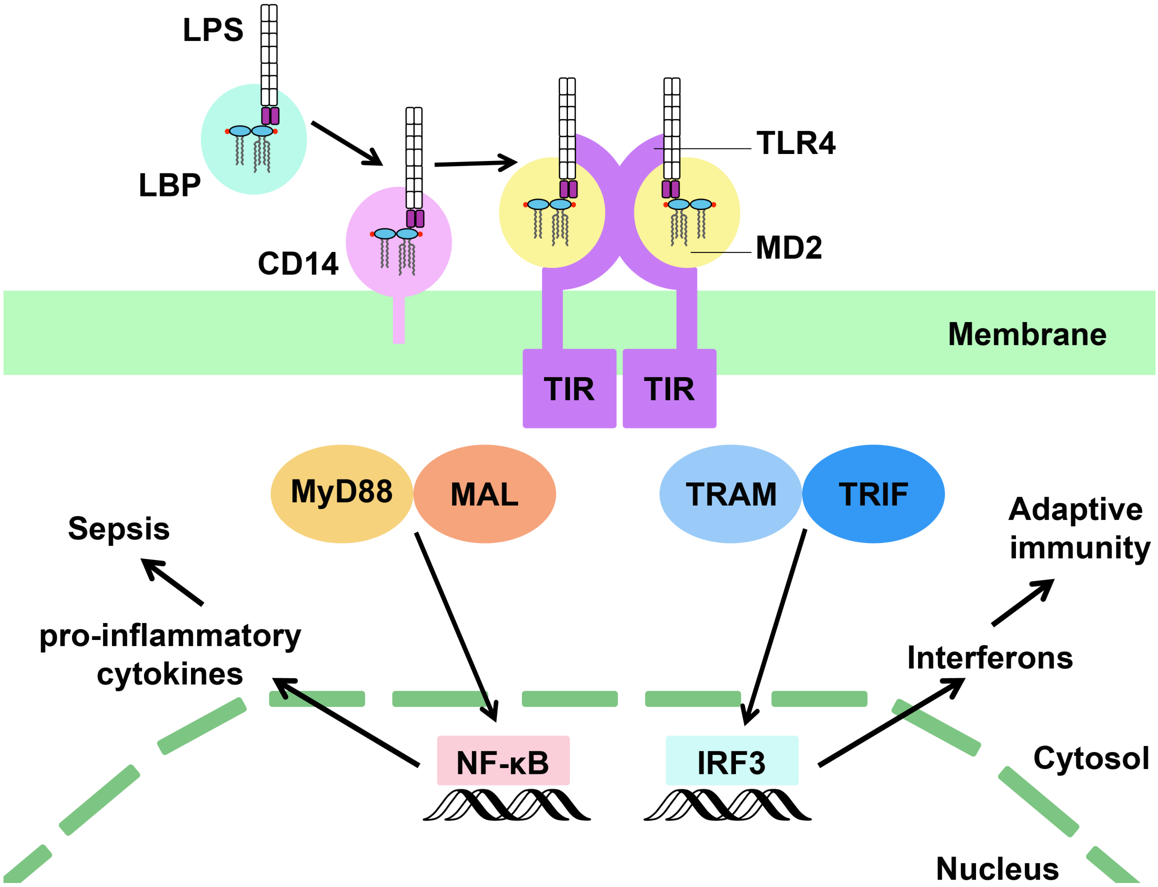

Figure 1.4: Human immune response to LPS. LBP enhances transfer of the LPS to CD14, which in turn delivers LPS to the MD2 portion of TLR4/MD2 heterodimer on the surface of macrophages. Upon binding, two TLR4/MD2 complexes dimerize, and the TLR4s cytoplasmic domain activates MyD88/MAL or TRIF/TRAM signaling pathway. These events lead to production of pro-inflammatory cytokines and interferons mediated by NF-κB and IRF3 transcription factors, respectively. Interferons are important for adaptive immunity, whereas overproduction of pro-inflammatory cytokines can cause sepsis and be lethal.

Bacterial infection caused by Gram-negative pathogens is a major public concern (30). This is especially true with infections caused by multi-drug resistant Gram-negative bacteria (31). Historically, antibacterial agents combat infectious bacteria through targeting three essential cell processes that include DNA replication and repair, protein synthesis, and peptidoglycan biosynthesis. However, the rapid development of antibiotic resistance by bacteria demands new biosynthetic pathways to be explored for discovery of novel antibiotics (32, 33). Given the essential role of lipid A in viability and pathogenesis of Gram-negative microorganisms, understanding lipid A biosynthesis is of great interest.

1.2 Raetz pathway of lipid A biosynthesis

The biosynthesis of lipid A has been studied and characterized over the past three decades by Raetz and coworkers. In *E. coli*, nine conserved constitutively expressed enzymes convert uridine diphosphate *N*-acetylglucosamine (UDP-GlcNAc) to a hexa-acylated glucosamine-based disaccharide termed Kdo_2-lipid A (Fig. 1.5) (5). LpxA catalyzes the first step of lipid A production by transferring an *R*-hydroxymyristoyl group from acyl-carrier-protein (ACP) to the 3-position hydroxy group of UDP-GlcNAc. The 3-*O*-acylation of UDP-GlcNAc by LpxA is thermodynamically unfavorable ($K_{eq} \cong 0.01$) (34), therefore, the deacetylation of the LpxA product, UDP-3-*O*-(*R*-3-

hydroxymyristoyl)-GlcNAc, by the zinc-dependent deacetylase, termed LpxC, is the committed reaction of the lipid A pathway (35). LpxD is responsible for transferring another β-hydroxy containing acyl-chain that measures 14-carbons in length from ACP to the 2-position amino group of UDP-3-*O*-(*R*-3-hydroxymyristoyl)-glucosamine (UDP-3-*O*-acyl-GlcN) (36). The first three enzymes of lipid A pathway (LpxA, –C, and –D) are cytoplasmic proteins, and their structures have been reported (37-39). Interestingly, LpxA and –D display significant structural homology and catalyze very similar chemistry.

The fourth and fifth step in lipid A biosynthesis are carried out by LpxH and LpxB, which are peripheral proteins, and their structures have yet to be determined (40, 41). LpxH catalyzes the cleavage of the pyrophosphate of UDP-2,3-diacyl-GlcN to generate UDP-2,3-diacyl-GlcN-1-phosphate (lipid X) and uridine monophosphate (UMP). Subsequently, LpxB condenses a molecule of UDP-2,3-diacyl-GlcN with lipid X through a β,1′→6 linkage to form tetra-acylated disaccharide-1-phosphate and UDP.

The last four enzymes of the pathway (LpxK, KdtA, LpxL, and LpxM) are integral inner membrane proteins with one predicted transmembrane helix at their amino (N)-terminal end. The LpxB product is phosphorylated at the 4′-position hydroxy group by LpxK kinase, yielding lipid IV_A (42). KdtA glycosyltransferase decorates lipid IV_A with two Kdo sugars (3-deoxy-D-*manno*-oct-2-ulosonic acid) at the 6′-position to form Kdo_2-lipid IV_A species (43). LpxL acyltransferase adds a lauroyl group to the 2′-

acyl group of Kdo_2-lipid IV_A (44), and lastly, LpxM adds a myristoyl group to the 3′-acyl group to generate Kdo_2-lipid A (45). Because the substrates of these enzyme are water-soluble, it is presumed that the their active sites face the cytoplasm (5).

Once assembled, Kdo_2-lipid A can be decorated with the core sugars on the cytoplasmic face of the inner membrane by the Waa family of glycosyltransferases (5, 46). The ATP-binding cassette transporter MsbA flips the glycosylated Kdo_2-lipid A into the outer monolayer of the inner membrane (47). In the periplasmic space WaaL ligase transfers O-antigen sugars, which are linked to an undecaprenyl-diphosphate, to the nascent LPS precursor (48). The details of LPS translocation from the inner to the outer membrane remain to be fully understood. However, it has been proposed that a complex of seven LPS transport (Lpt) proteins (LptA–G) extracts the LPS from the periplasmic surface of the inner membrane and shuttle it to the outer membrane (Fig. 1.6) (49).

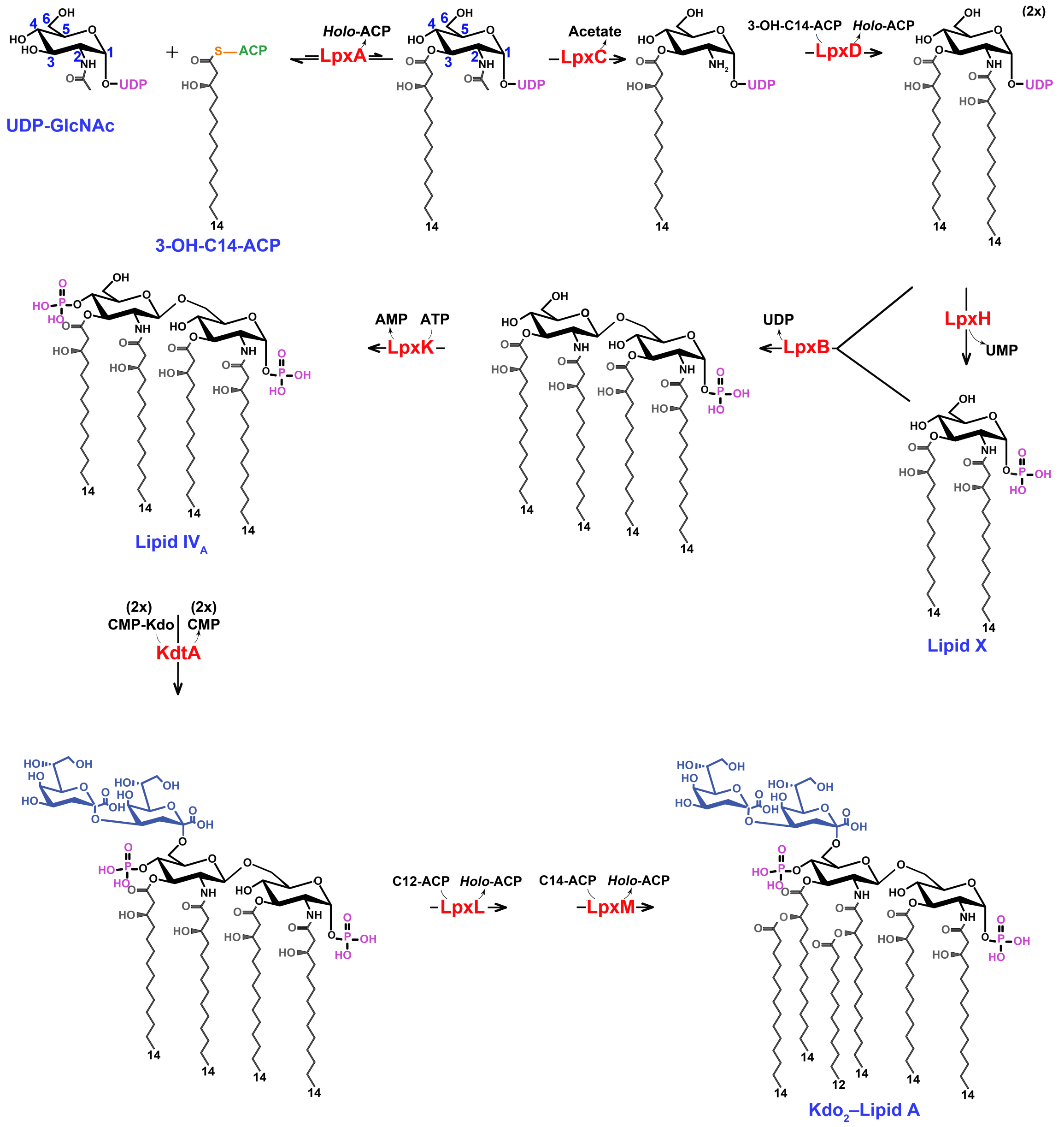

Figure 1.5: Biosynthetic pathway of lipid A production in *E. coli*. Nine highly conserved enzymes (red text) perform an array of reactions including acylation, deacetylation, hydrolysis, condensation, phosphorylation, and glycosylation to convert UDP-GlcNAc to Kdo$_2$–lipidA. The blue and black numbers indicate the carbon number of the glucosamine ring, and the acyl-chain length, respectively.

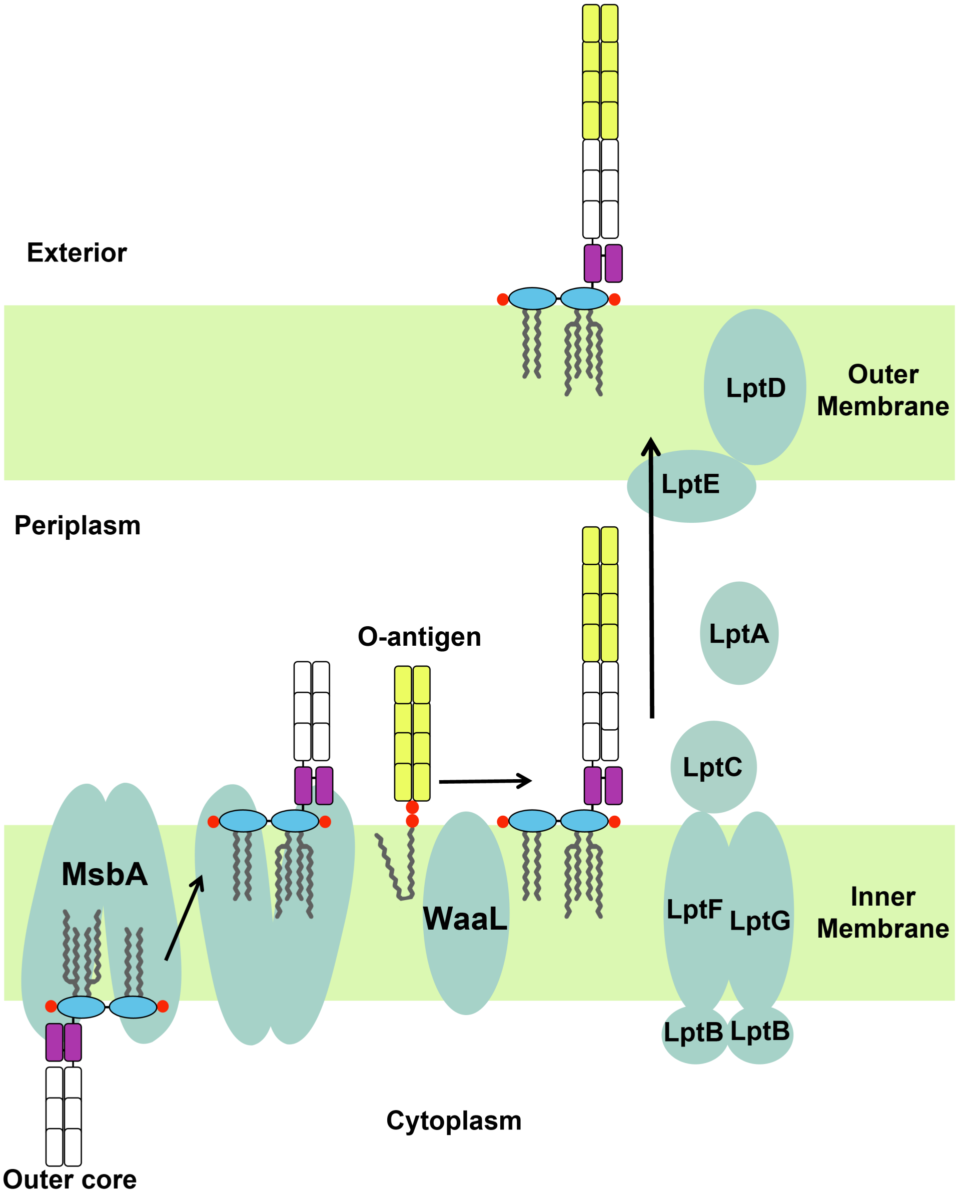

Figure 1.6: LPS transport in *E. coli*. Once Kdo$_2$-lipid A is charged with the core oligosaccharides (white boxes), MsbA transporter flips the nascent LPS across the inner membrane. The O-antigen sugars (yellow boxes), which are assembled on undecaprenyl pyrophosphate, are ligated to the core sugars by WaaL. LPS is extracted from the periplasmic side of the inner membrane by LptB, LptC, LptF, and LptG, and shuttled to the outer membrane by LptA. The essential outer membrane proteins, LptD and LptE, are believed to flip LPS to the outer leaflet of the outer membrane.

1.3 Acyl-carrier-protein

Acyl-carrier-protein is central to acyl-chain delivery in the cell, and represents one of the most highly conserved proteins across all organisms (50). Inactive ACP is referred to as *apo*-ACP, which is activated post-translationally by attachment of a 4'-phosphopantetheine (4′-PPT) group donated by coenzyme A (CoA). This reaction is catalyzed by holo-ACPS synthase (ACPS, also known as phosphopantetheinyl transferase), and the activated form of the carrier-protein is termed *holo*-ACP (Fig. 1.7) (51). The 4'-phosphopantetheine prosthetic group is covalently attached through a phosphodiester linkage to a conserved serine residue (Ser36 in *E. coli*) that is usually flanked by an aspartate and a leucine residue. Subsequently, the sulfhydryl group of the phosphopantetheine arm of *holo*-ACP is used to form a thioester bond with fatty acids to generate *acyl*-ACP (50).

The vast majority of ACPs charged with acyl-chains are generated by the fatty acid synthesis machinery (52). The biosynthesis of fatty acids is highly conserved, and initiates with the ATP-dependent carboxylation of acetyl-CoA to malonyl-CoA by acetyl-CoA carboxylase (AAC). The generated malonyl group is then thioester-linked to the prosthetic 4′-phosphopantetheine group of *holo*-ACP by malonyl/acetyl-CoA–ACP transacylase (MAT), which also transacylates the acetyl group from acetyl-CoA to *holo*-ACP. The malonyl-ACP enters the elongation process by going through a chain of chemical reactions involving i) decarboxylative condensation with the acetyl-ACP by a β-ketoacyl synthase (KS), ii) NADPH-dependent reduction of the oxoacyl intermediate through β-ketoacyl reductase (KR), iii) dehydration of the β-hydroxy-acyl intermediate by a dehydratase (DH), and iv) further NADPH-dependent reduction by a β-enoyl reductase (ER) to form a saturated nascent fatty-acyl chain attached to ACP. The cycle continues through the condensation of the *acyl*-ACP with another malonyl-ACP, and repeats to grow the acyl-chain by 2-carbon units at a time (Fig. 1.8).

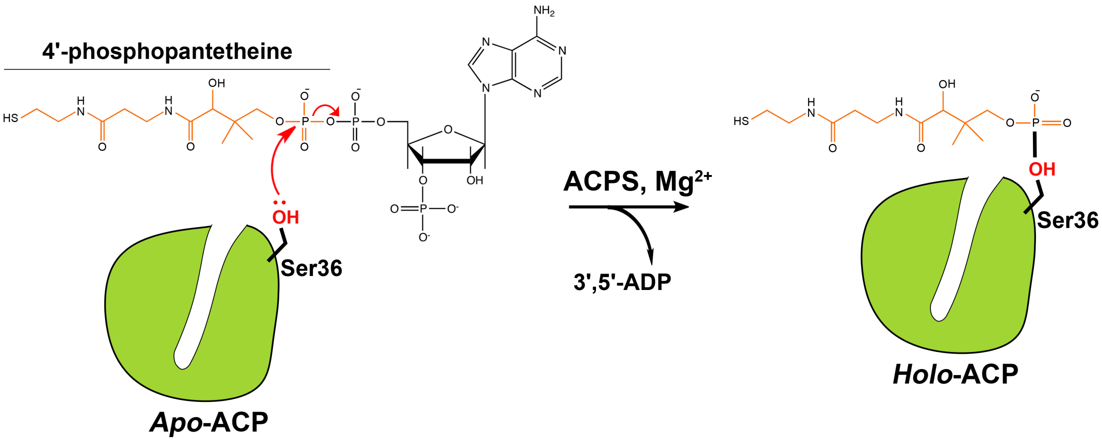

Figure 1.7: Activation of ACP by ACPS phosphopantetheinyl transferase. *Apo*-ACP is post-translationally modified by holo-ACP synthase (ACPS), which transfers a 4′-phosphopantetheine group from CoA to Ser36 in a magnesium-dependent reaction. The activated form of ACP is termed *holo*-ACP. The 4′-phosphopantetheine group of *holo*-ACP can bind different fatty acids through a high-energy thioester bond.

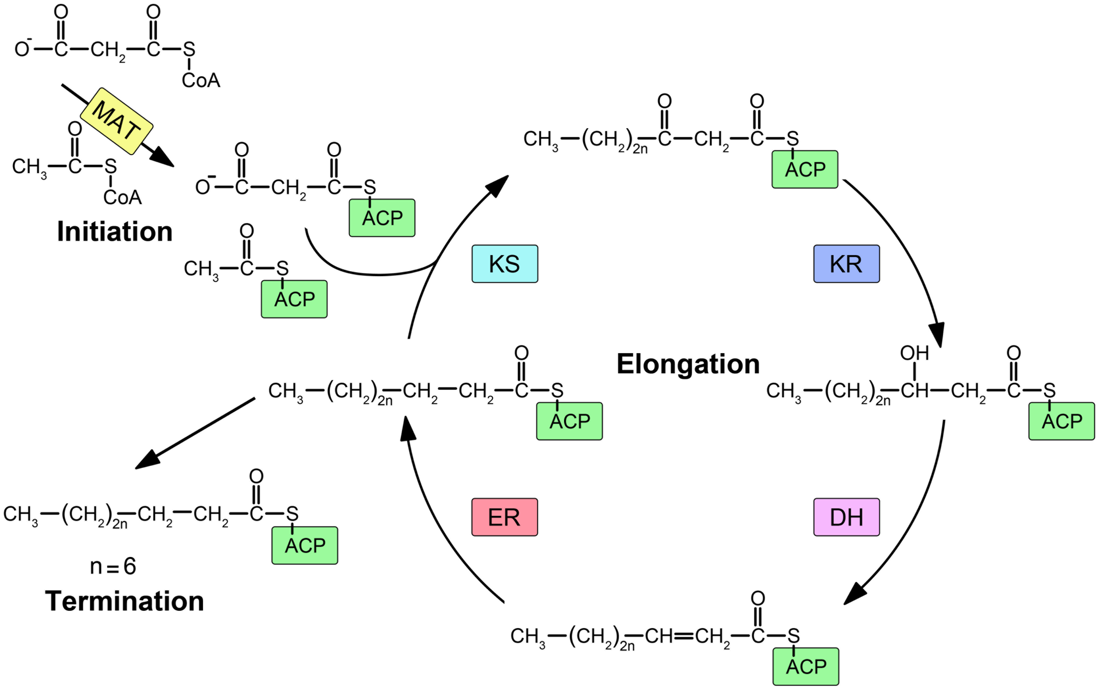

Figure 1.8: Generalized pathway of fatty acid synthesis. After the initiation step in which an acetyl and a malonyl group are transferred to ACP by malonyl/acetyl-CoA–ACP transacylase (MAT), a series of cyclical chemical reactions involving condensation (KS), dehydration (DH), and reduction (KR, ER) are performed on the nascent acyl-chain. The cycle repeats to generate acyl-chains of various lengths.

In mammals, fungi, and some bacteria, ACP is found integrated with large multifunctional enzyme complexes, for example with the type I fatty acid synthase (FAS) system (53-55). Conversely, ACP in most microorganisms, such as *E. coli*, and also in specialized eukaryotic organelles, such as mitochondria and plastids in plants, functions in the dissociated type II system (56). The discretely expressed enzymes and soluble ACP of the type II prokaryotic systems are structurally and functionally analogous to their counterparts in the eukaryotic type I system (Table 1.1) (57). These enzymes are believed to associate noncovalently, but little is known about their stoichiometry and organization *in vivo*. In this manner, type II ACP is highly diffusible in the cell facilitating association with a vast number of protein partners, for the efficient delivery of a broad assortment of acyl-substrates for diverse biosynthetic pathways. In addition to the classical roles of ACP such as fatty acid (58), phospholipid (59), polyketides (60), nonribosomal peptide (61), and lipid A biosynthesis (62), ACP is also essential in many other processes, such as quorum sensing (63), lipoic acid biosynthesis (64), acylation of toxic proteins (hemolysin) (65), and membrane-derived oligosaccharide synthesis (66). ACP interacts with over 25 partners in Gram-negative bacteria (Table 1.2), of which the majority are acyltransferases (56). In this way, bacterial ACP, along with ribosome associated proteins, RNA and DNA polymerases, represents one of the four major protein–protein interaction "hubs" in the cell (67).

Table 1.1: Domains of FAS I elongation cycle and their type II functional analogs.

Mammalian FAS domain*	Related bacterial FAS enzymes
MAT	FabD
KS	FabB, FabF, FabH
KR	FabG
DH	FabA, FabZ
ER	FabI, FabK, FabL

* MAT, malonyl/acetyl-CoA–ACP transacylase, KS, β-ketoacyl synthase, KR, β-ketoacyl reductase, DH, dehydratase, ER, β-enoyl reductase.

Table 1.2: ACP Partners in Gram-negative Bacteria.

Protein(s)	Activity or function
ACPS	Holo-ACP synthase
ACPH	Holo-ACP phosphodiesterase
FabA, FabB, FabD, FabE, FabF, FabG, FabH, FabI, FabK, FabL, FabZ	Fatty acid synthase component enzymes
PlsB, PlsC, PlsX	Phospholipid acylation
HlyC	Protein acylation (hemolysin)
LipB	Lipoic acid biosynthesis
LpxA, LpxD, LpxL, LpxM	Lipid A biosynthesis
LuxI, Ains (e.g., Vibrio fischeri)	Quorum sensing: AHL synthesis
LuxD	Bioluminescence: acyl-ACP esterase
Aas	Acyl-ACP ligation/phospholipid reacylation
AasS (vibrio harveyi)	Acyl-ACP ligation
MdoH	Membrane-derived oligosaccharide synthesis

1.4 Structure of acyl-carrier-protein

ACP is a small globular protein that consists of 70 to 100 amino acid residues, and is an essential cofactor of many primary and secondary metabolic pathways. Over the past 25 years, NMR and crystallographic studies of type II ACP from a wide variety of organisms have revealed that the overall fold of the carrier-protein is a 4–helix bundle (I-IV) with several loop regions (L1-L3) (Fig. 1.9) (68, 69). Unlike the well-studied type II family, only the rat, human, and yeast *Saccharomyces cerevisiae* type I ACPs are structurally characterized to date (Fig 1.10) (70-72). Despite the low amino acid sequence identity between rat and human ACPs, the structures of both display a 4–helix bundle fold that is reminiscent of type II ACPs. Interestingly, the X-ray structure of yeast ACP, which was solved as part of the mega-synthase, revealed an additional domain composed of 4 α-helices (72). The NMR structures of the isolated ACP domain of yeast FAS are consistent with the X-ray structure, nonetheless the exact role of this added domain remains unknown (73).

Type II ACP accommodates its covalently attached acyl-chain inside a central hydrophobic pocket formed by the four α-helices (Fig. 1.11) (69, 74). The phosphopantetheine places the thioester bond at the opening of the hydrophobic pocket that is formed by L1, N-terminus of helix II, helix III, and L3. By doing so, the reactive thioester bond is protected from hydrolysis, an event that would lead to release of immature fatty acids. The acyl-chain adopts a linear conformation and runs through the core of ACP, almost parallel with helix II and IV, and points toward L2 and the C-terminal end of helix IV.

Although the yeast, human, and rat studies of ACP integrated within FAS have revealed some structural information, the acyl-moiety of ACP was absent in these structures. The current structures of type I ACP display that the entrance to the central hydrophobic cavity is barricaded by the C-terminal region of L1, helix III, and L3, suggesting that ACP in type I machinery does not accommodate its acyl-chain inside this cleft (Fig. 1.12). The fact that ACP is integrated within its own biosynthetic compartment in the type I system may explain why the acyl-chain does not need to be sealed inside the hydrophobic pocket as is the case for the dissociated system of type II (70). Further structural and biochemical experiments are necessary to understand the architecture of type I *acyl*-ACP.

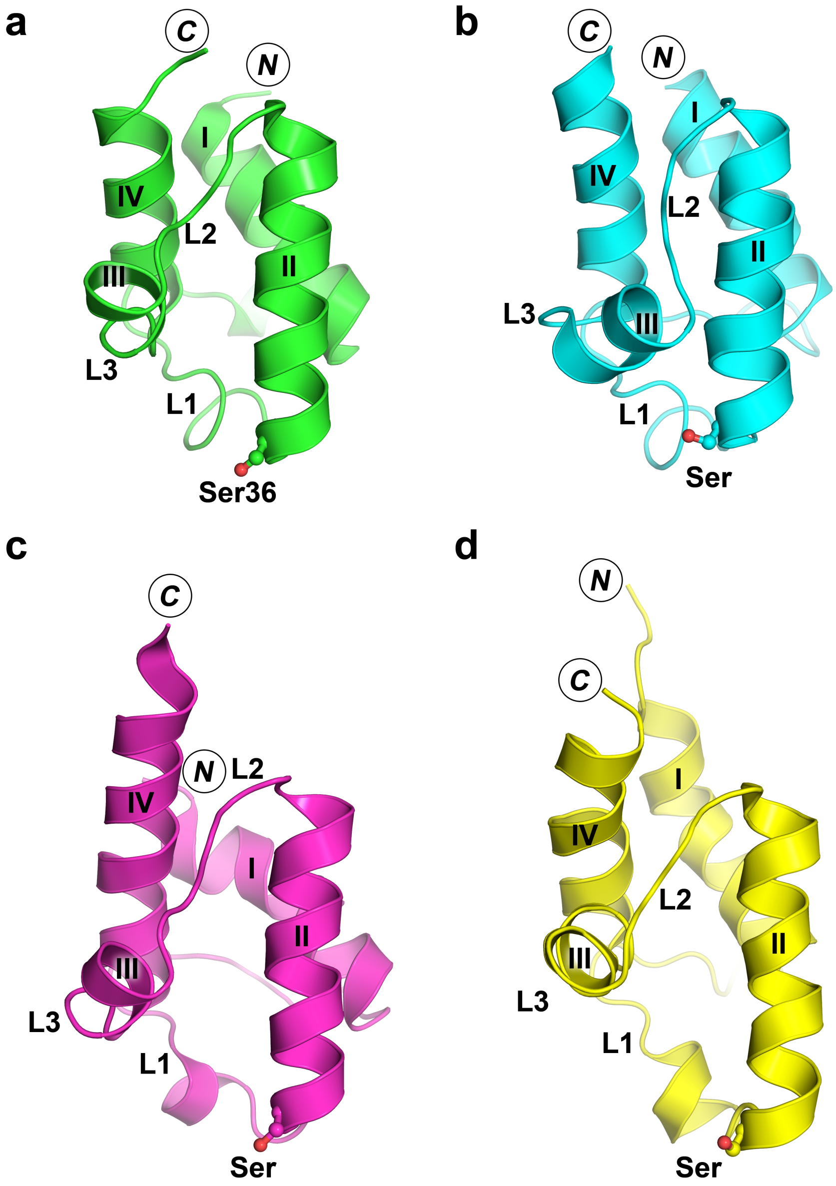

Figure 1.9: Molecular structure of type II ACP. The overall fold of type II ACP is a 4-helix bundle. Helix I is connected to helix II via a long loop (L1). L2 connects helix I to helix III, and L3 connects helix III to helix IV. **(a)** Crystal structure of *E. coli apo*-ACP (PDB code: 1T8K). The NMR structure of **(b)** *Bacillus subtilis apo*-ACP (PDB code: 1HY8), **(c)** *Geobacter metallireducens holo*-ACP (the 4′-phosphopantheteine group is not shown; PDB code: 2LML) and **(d)** *Rickettsia prowazekii apo*-ACP (PDB code: 2LOL). ACP is phosphopantetheinylated at a serine residue situated at the beginning of helix II. The N- and C-termini are labeled.

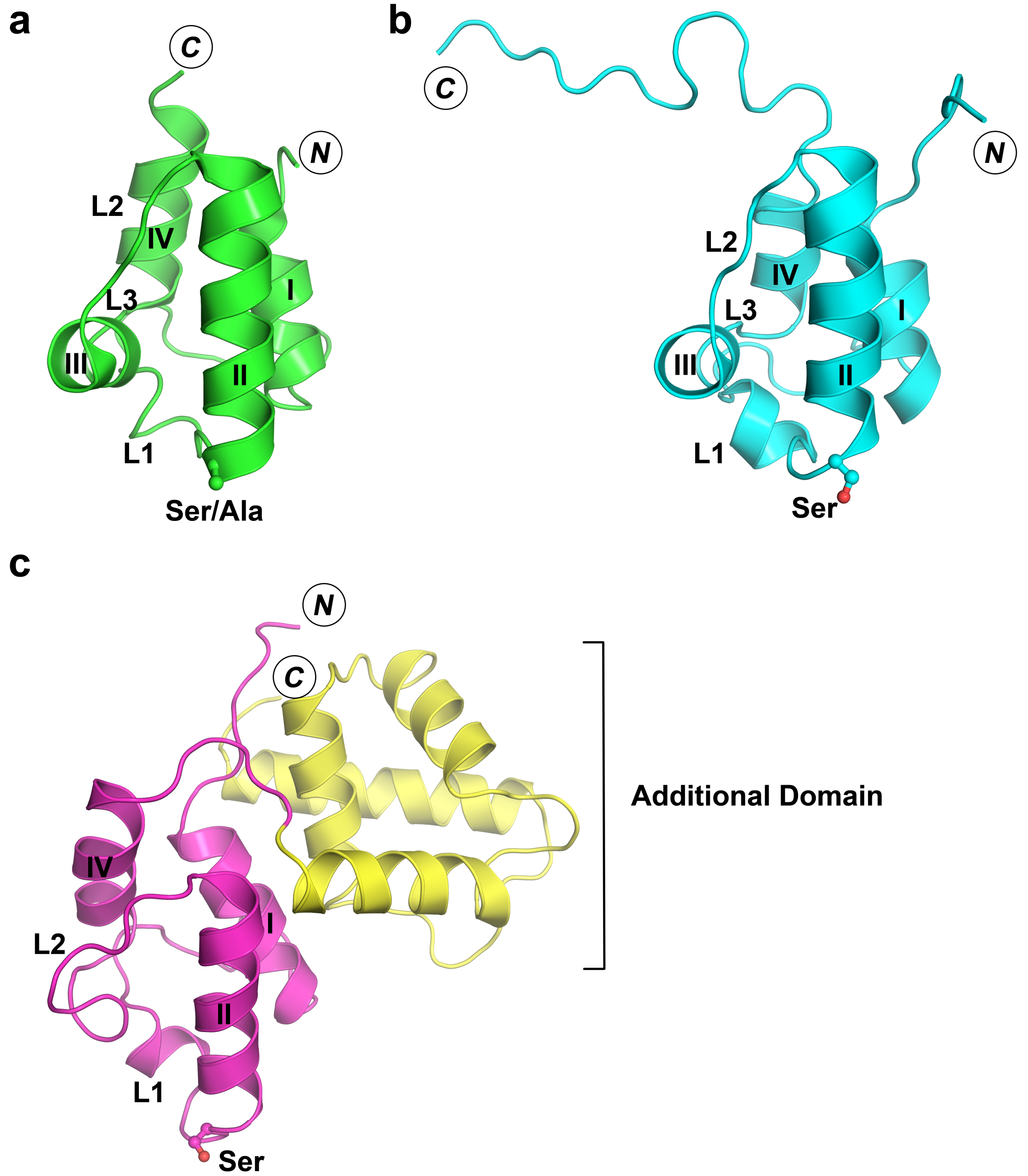

Figure 1.10: Molecular structure of type I ACPs. Type I ACP is structurally similar to Type II ACP. **(a)** Crystal structure of human fatty acid synthase ACP domain (PDB code: 2CG5). **(b)** NMR solution structure of rat ACP (PDB code: 2PNG). **(c)** Crystal structure of yeast ACP domain solved as part of fatty acid synthase complex (PDB code: 2UV8). Yeast ACP has an additional domain (yellow) with unknown function.

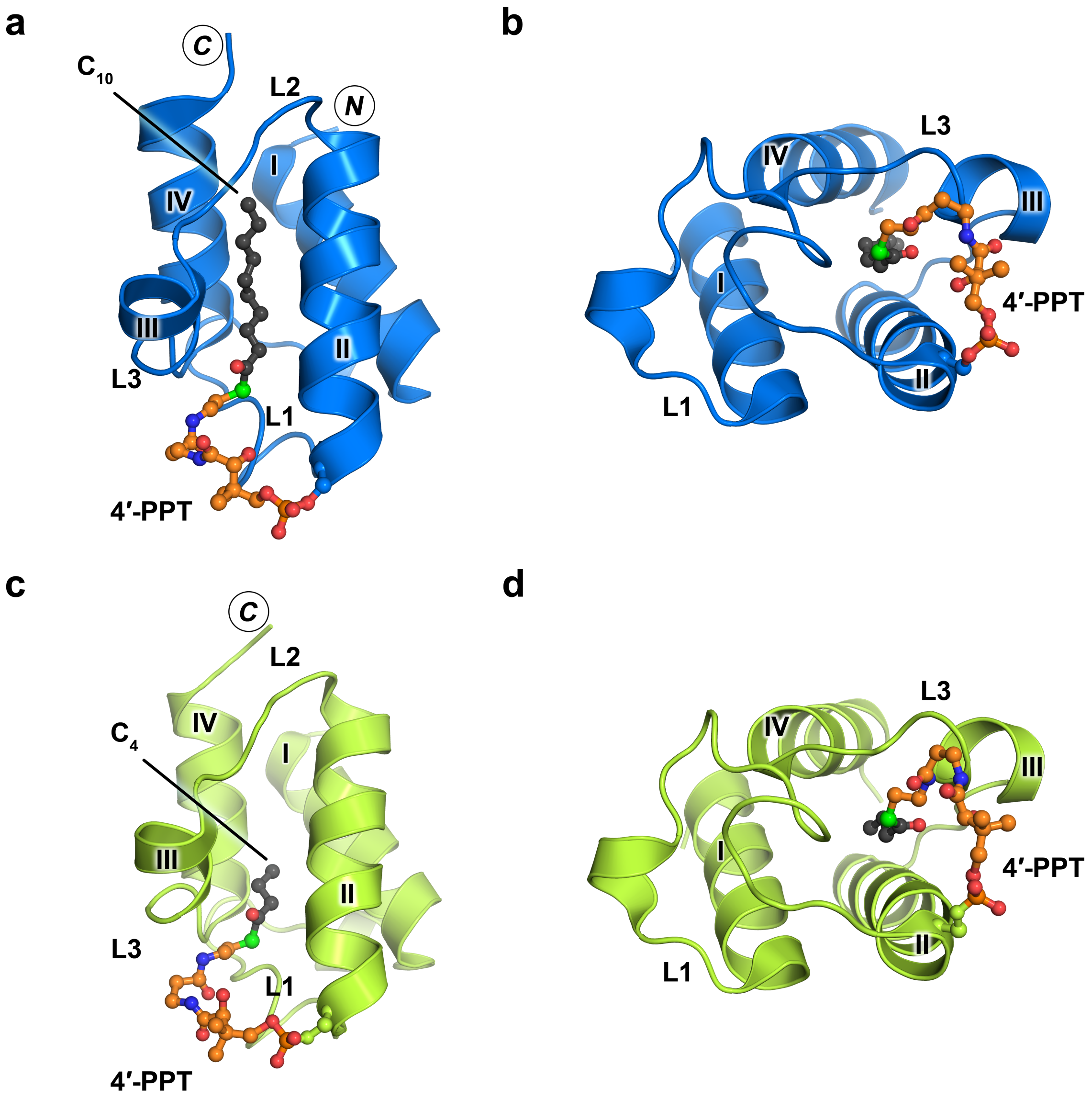

Figure 1.11: Structure of type II *acyl*-ACP. Type II ACPs accommodate their acyl-substrate cargo inside a hydrophobic pocket formed by the four helices. The thioester bond is situated at the opening of the hydrophobic cavity, which is formed by the C-terminal end of L1, N-terminal region of helix II, helix III, and L3. **(a,b)** Crystal structure of decanoyl-ACP (PDB code: 2FAE). **(a)** Side-view of decanoyl-ACP. The acyl-chain is oriented parallel to helix II and helix IV. The 4′-phosphopantheteine (4′-PPT) is colored orange and by atom type. The acyl-chain is colored black, and its length is indicated. **(b)** The opening of the hydrophobic pocket. The thioester bond (green sphere) is protected from hydrolysis. **(c,d)** Crystal structure of butyryl-ACP (PDB code: 1L0I). **(c)** The 4′-PPT tucks the short acyl-chain inside ACP. **(d)** The conformation of 4′-PPT is similar to that of decanoyl-ACP.

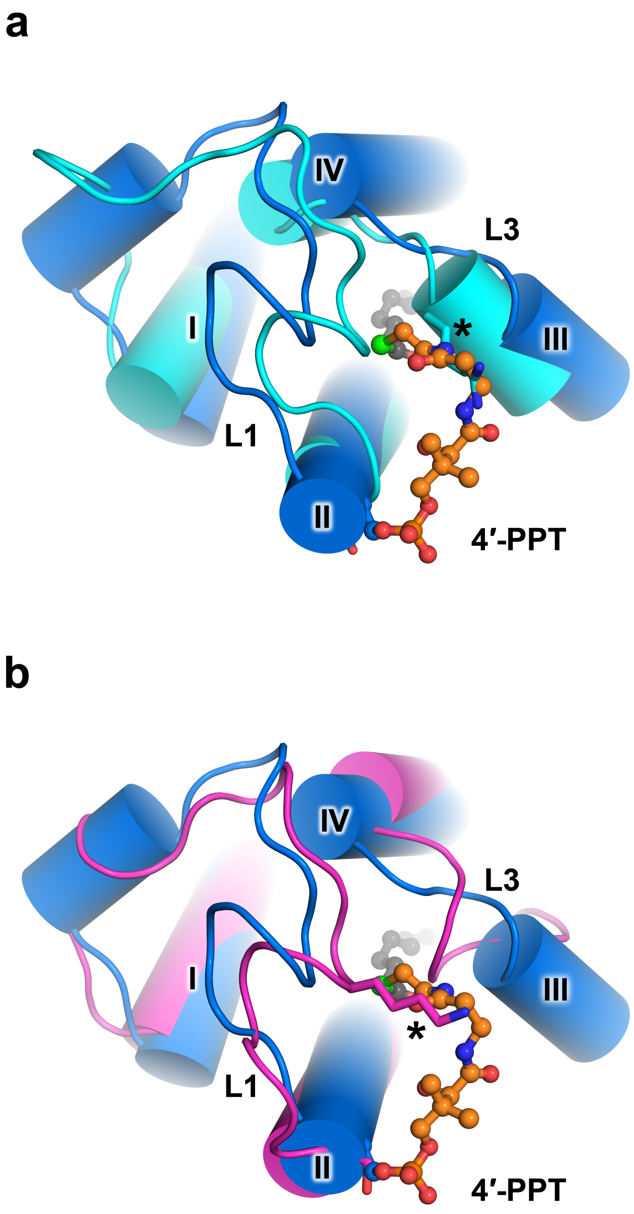

Figure 1.12: Comparison between type I and type II ACPs. In type I ACPs, the pocket opening is closed off by L1, helix III, and L3. **(a)** Overlay of rat ACP (cyan, PDB code: 2PNG) and type II decanoyl-ACP (blue, PDB code: 2FAE). An arginine residue (indicated by an asterisk) from helix III of yeast ACP overlaps with the 4′-PPT group of decanoyl-ACP. **(b)** Overlay of yeast ACP (magenta, PDB code: 2UV8) and type II decanoyl-ACP. A lysine residue (indicated by an asterisk) blocks the pocket opening and overlaps with the 4′-PPT group of decanoyl-ACP.

1.5 Structural flexibility of type II Acyl-carrier-protein

Bacterial ACP has a relatively high ratio of charged to hydrophobic residues, and exhibit resistance to precipitation by heating or organic solvents (56). Moreover, ACP is highly acidic ($\mathrm{pI}_{E.\ coli}$ ACP = 4.1), which gives rise to abnormal SDS-PAGE migration (75). These physical properties are a hallmark of intrinsically unstructured proteins, and the repulsive electrostatic forces resulting from the high concentration of acidic residues in the central region of ACP contribute to the structural flexibility of ACP (56). The region that spans from residue Glu30 to Glu60 in *E. coli* ACP includes 14 acidic and no basic residues. Two clusters of highly conserved acidic residues exist within this region, site A (Glu30, Asp35, and Asp38) and site B (Glu47, Asp51, Glu53, and Asp56), which display low affinity for divalent cations (dissociation constant/site = ~ 80 μM) (76, 77). Unlike *E. coli* ACP, *Vibrio harveyi holo*-ACP is largely unfolded at neutral pH. Interestingly, binding of Ca^{2+} or Mg^{2+} to the aforementioned acidic sites (site A and B), or the neutralization of helix II through mutagenesis induces a stabilized protein fold with a α-helix content of 40–50% (78, 79). Furthermore, interaction with partner enzymes such as phosphopantetheinyl transferase and the *O*-acyltransferase of lipid A biosynthesis (LpxA) can induce protein folding (79).

Although the physical properties of ACP are not adequate to substantiate the notion of ACP being natively unfolded, perhaps they could affect mechanisms through which ACP recognizes its partners. Moreover, ACP needs to undergo a significant conformational change to sequester and eject its cargo to the active site of partner enzymes. Hence, it appears that ACP flexibility is required for sampling the necessary conformations in order to stabilize and efficiently deliver thioester-linked acyl-chains.

1.6 Recognition of type II Acyl-carrier-protein

ACP has evolved the ability to transiently associate with a vast number of protein partners for efficient delivery of fatty acyl-substrates that are thioester-linked to its prosthetic 4'-phosphopantetheine group. This attribute is reflected by the relatively low micromolar dissociation constant (K_d) of ACP with a wide variety of protein partners, which enables it to rapidly exchange among its partnering enzymes, thus maximizing its efficiency in delivering acyl-substrates (80-82). All the while, ACP relies on the high degree of selectivity displayed by its protein partners.

Mutagenesis and binding assay studies have shown that helix II of ACP and its acidic residues are involved in recognition of various enzymes (79, 83, 84). There is no known ACP binding sequence motif, however it is well established that ACP recognizes basic patches on its partner enzymes (56, 81, 82). Various binding studies suggest that ACP partners, such as phosphopantetheinyl transferase and fatty acid biosynthetic enzymes like FabD, FabG, FabH, and FabI, possess arginine or sometimes lysine residues that have been shown to be critical in ACP binding (80-82, 85).

Significant effort has been devoted to understand the molecular basis of ACP association through X-ray crystallography, however, due to the highly transient nature of ACP-based interactions, structural studies of ACP complexes have been hindered. Very few crystal structures of the type II carrier-protein in complex with an enzyme have been solved in recent years. The trimeric structure of the phosphopantetheinyl transferase ACPS from *Bacillus subtilis* bound to three molecules of *holo*-ACP provided the first glimpse into the charge complementation mechanism of ACP recognition (86). The acidic residues localized on helix II and III of ACP form direct contacts with basic residues on ACPS (Fig. 1.13a). In the co-crystal structure of enoyl reductase FabI with dodecenoyl-ACP, the details of interaction between ACP and FabI could not be elucidated due to missing electron density of side chains and phosphopantetheine (85). Cytochrome P450 from *B. subtilis* was crystalized with *E. coli acyl*-ACP, which also revealed the same trend of electrostatic interactions with helix II and III (Fig. 1.13b) (87). Interestingly, for the first time it was discovered that the acyl-chain was ejected from the core of ACP and was placed within the active site of P450. More recently, 3-hydroxyacyl-ACP dehydratase (FabA) was crystalized with *acyl*-ACP through crosslinking the two protein partners together (88). This co-complex structure also showed that the acyl-chain flips out of ACP and key hydrophobic residues on helix II and III collapse to block the hydrophobic pocket. Although these structures have provided considerable insight into how ACP recognizes its partner enzymes, the mechanism by which these enzymes discriminate between ACP molecules that are loaded with various acyl-chains of differing length, degree of saturation, or hydroxylation is not well understood.

A series of NMR structures of *Streptomyces coelicolor* ACP bound to fatty acyl-chains that represent a complete cycle of fatty acid biosynthesis have been reported (89). In all of these structures, the hydrophobic portion of the acyl-chain is tucked inside the central hydrophobic pocket with the first hydrophilic group of the acyl-chain that precedes the non-polar portion stuck at the entrance of the pocket, preventing further insertion of the acyl-chain into the pocket (Fig. 1.14). The degree of exposure of the acyl-chain and the conformation of the 4'-phosphopantetheine group are associated with reorganizations of helix III. These structures suggest that the conformation of the 4'-phosphopantetheine group and helix III contribute to a specific surface feature, helping ACP-partners to recognize their preferred *acyl*-ACP intermediates. On the other hand, regardless of the arrangement of the acyl-chain, the conformation of helix II remains unaffected, suggesting that it may act as a universal “recognition helix” though it does not contribute to the mechanism by which enzymes select the proper *acyl*-ACP intermediate.

Further structural and functional experiments are necessary to understand i) the molecular basis for recognition of ACP by its multiple partners, ii) the role of the 4′-phosphopantetheine arm in complex formation, iii) the mechanism of acyl substrate ejection, and iv) the way by which ACP disengages from its protein partners. Presented in the chapters that follow are structural and biochemical data that have contributed greatly to the understanding of ACP-based interactions by exploiting two of the four acyltransferases of the Raetz pathway – LpxA and LpxD.

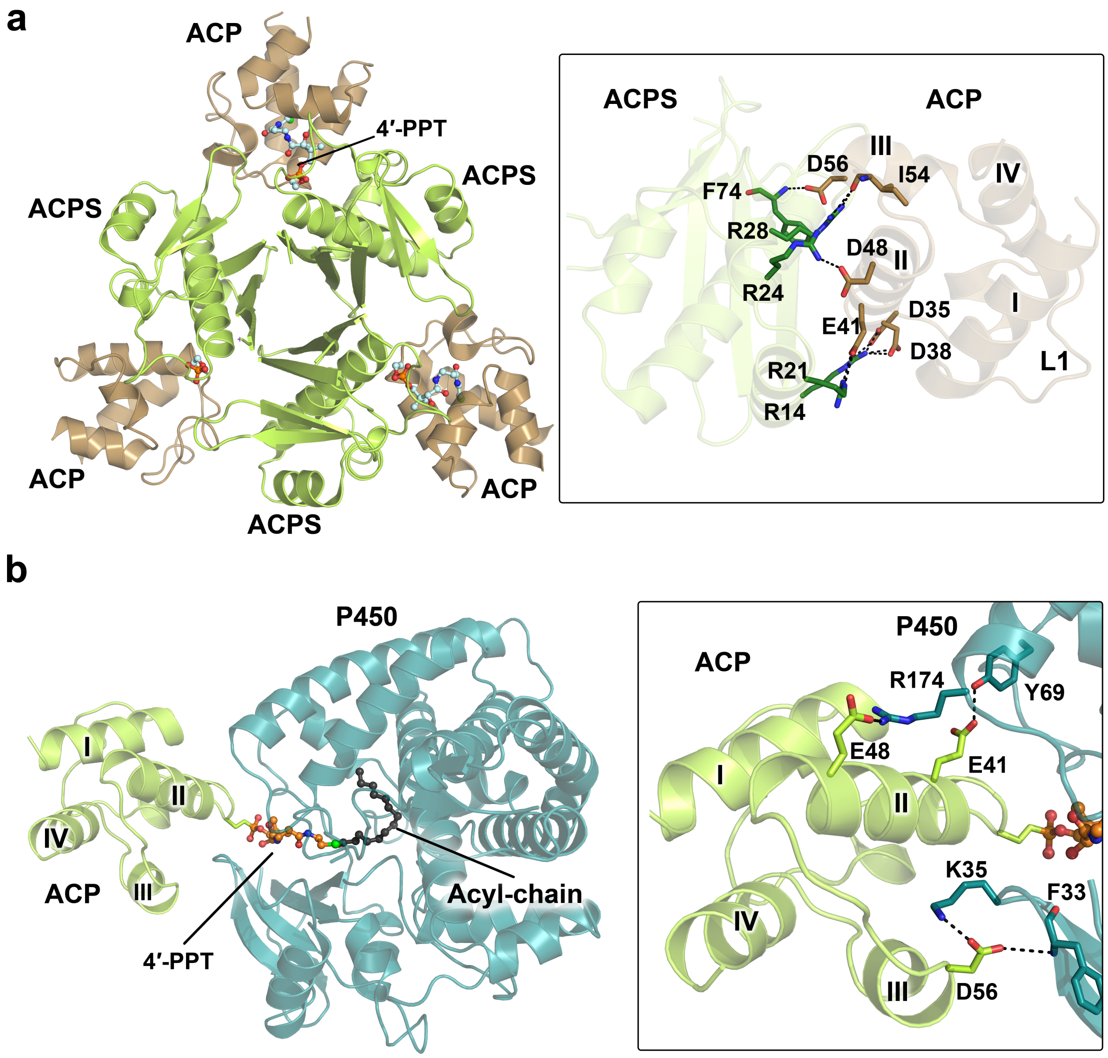

Figure 1.13: ACP in complex with ACPS and cytochrome P450. Helix II and III of ACP provide electrostatic interactions with the partner enzymes. **(a)** Three ACP molecules (brown) are bound to the ACPS trimer (green), which performs phosphopantetheinyl transfer. The 4′-PPT group (cyan) is located at the interface between the two protein partners, and adopts a conformation similar to that of free *acyl*-ACP. The inset shows only those residues that provide strong electrostatic interactions at the binding interface. **(b)** *Acyl*-ACP (green) bound to cytochrome P450 (blue). The 4′-PPT (orange) is rotated to place the acyl-chain (black) in the active site of P450, which performs oxidative cleavage of fatty acyl-chains. The inset shows electrostatic interactions of P450 with helix II and helix III of ACP.

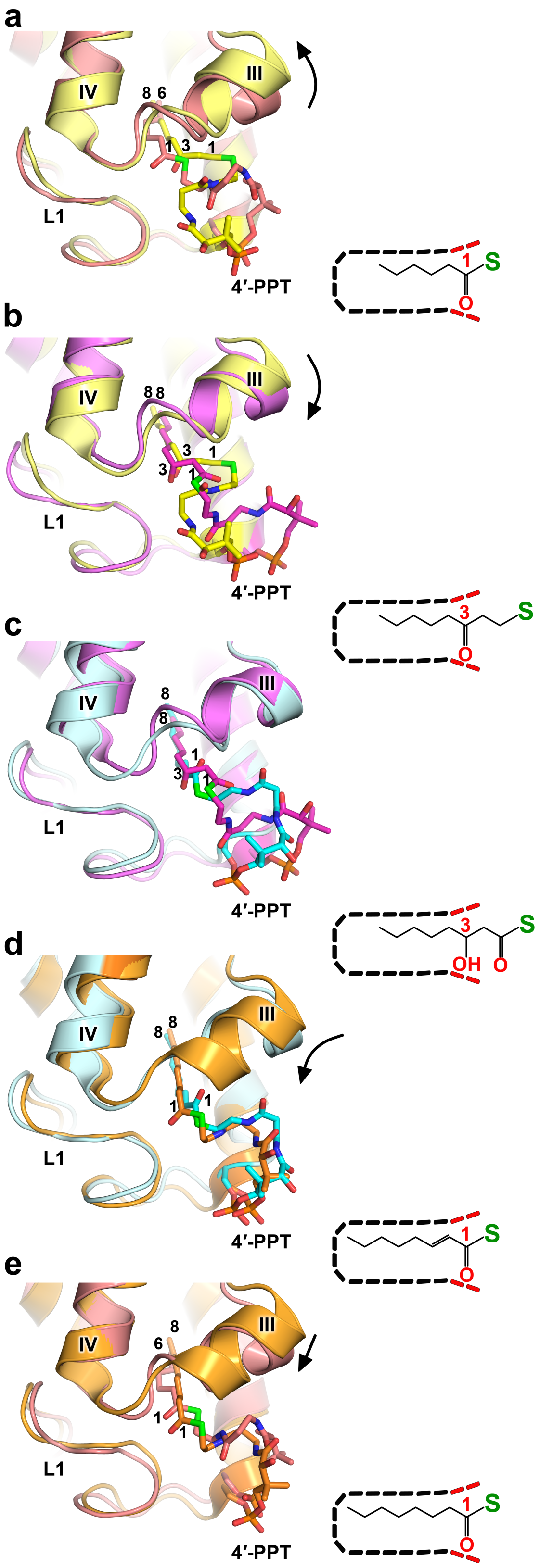
a
IV
III
8
6
1
3
1
L1
4′-PPT
1
S
O
b
IV
III
8
8
3
1
3
1
L1
4′-PPT
3
S
O
c
IV
III
8
8
1
3
1
L1
4′-PPT
3
S
OH
O
d
IV
III
8
8
1
1
L1
4′-PPT
1
S
O
e
IV
III
8
6
1
1
L1
4′-PPT
1
S
O

Figure 1.14: Comparison of ACPs charged with acyl-intermediates of a single cycle of fatty acid biosynthesis. Closest to average NMR structures are shown. The arrows indicate movement of helix III. Overlay of **(a)** hexanoyl- (salmon) and 3-oxooctanyl-ACP (yellow), **(b)** 3-oxooctanyl- (yellow) and *R*-3-hydroxyoctanoyl-ACP (pink), **(c)** and *R*-3-hydroxyoctanoyl (pink) and 2-octenoyl-ACP (cyan), **(d)** 2-octenoyl- (cyan) and octanoyl-ACP (orange), and **(e)** octanoyl- (orange) and hexanoyl-ACP. The right-hand panel is a schematic representation of the hydrophobic pocket (dashed lines) and the buried acyl-chain. The first polar oxygen preceding the hydrophobic portion of the acyl-chain is stuck at the pocket entrance. The carbon number of each acyl-chain is indicated. Hexanoyl-ACP (PDB code: 2KOO), 3-oxooctanyl-ACP (PDB code: 2KOP), *R*-3-hydroxyoctanoyl-ACP (PDB code: 2kOQ), 2-octenoyl-ACP (PDB code: 2KOR), and octanoyl-ACP (PDB code: 2KOS).

1.7 UDP-GlcNAc acyltransferase (LpxA)

LpxA is an ACP-dependent acyltransferase that catalyzes the first step of lipid A biosynthesis (Fig. 1.5). The crystal structure *E. coli* LpxA (EcLpxA) was first solved in 1995 in the absence of bound ligands, classifying a new family of enzymes that adopt an unusual left-handed β-helix (LβH) fold (Fig. 1.15a) (37). Each β-helical turn resembles an equilateral triangle, and is characterized by three repeating hexapeptide units with the consensus sequence of [LIV]-[GAED]-X_2-[STAVE]-X (Fig. 1.15b) (37, 90). More structures with this structural motif have emerged, including bacterial acetyl- and acyltransferases such as *N*-acetylglucosamine-l-phosphate uridyltransferase (91), galactoside acetyltransferase (92), tetrahydrodipicolinate *N*-succinyltransferase (93), xenobiotic acetlytransferase (94), serine acetyltransferase (95), and Vat(D) streptogramin acetyltransferase (96). Examples of the LβH architecture can also be found in archaebacterial and eukaryotic proteins (97, 98). The oligomeric structure of enzymes containing the LβH fold is trimeric, with each monomer being related to the neighboring subunit by a 120° rotation about the three-fold axis of symmetry that runs in parallel with the LβH domains. The length of LβH domains can vary considerably among this protein family, however the LβH found in LpxA is rather extended measuring, approximately 50 Å in length. In addition, LpxA contains a globular C-terminal domain, which is composed of four α-helices localized to one end (37).

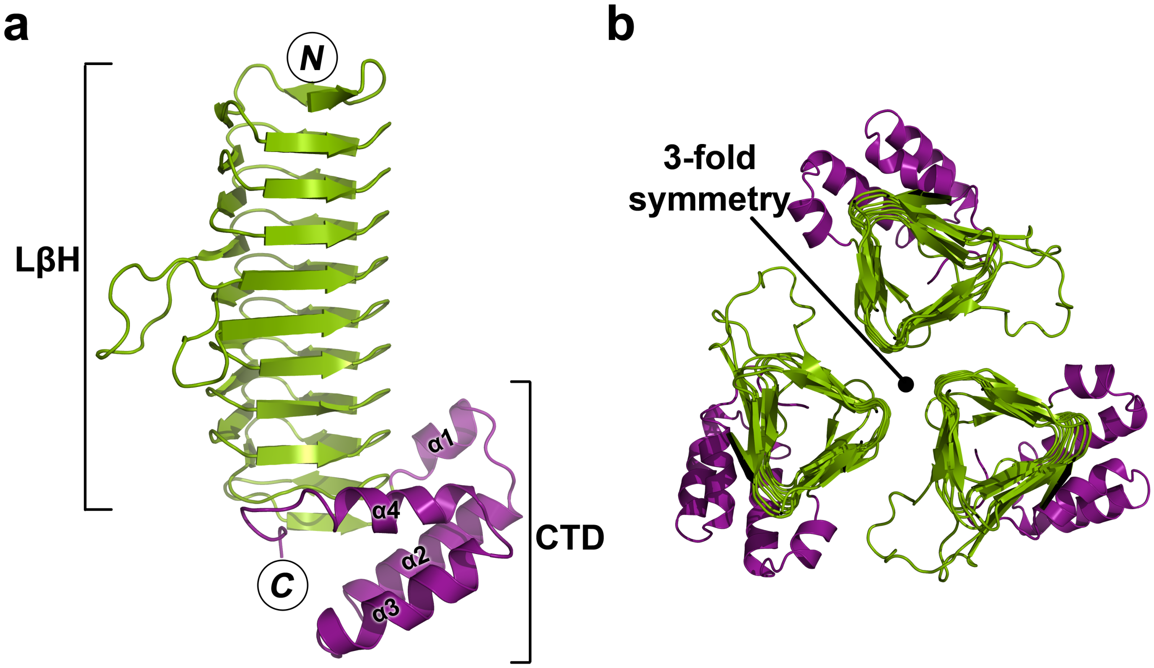

Figure 1.15: Crystal structure of *E. coli* LpxA. (a) Side view of LpxA (PDB code: 1LXA). Each monomer of LpxA is composed of a LβH domain (green) and an α-helical C-terminal domain (CTD, purple). The N- and C-termini are indicated. **(b)** Top-down view of LpxA trimer. The trimeric axis of symmetry runs in parallel with the LβH domain. Each β-helical coil resembles an equilateral triangle.

Sequence alignment of LpxAs from diverse bacteria revealed that several basic residues such as Lys76, His122, His125, His144, His160, and Arg204 are highly conserved (99). The LpxA structure showed these residues are localized around a cleft between two neighboring LβH domains. Because of the trimeric symmetry, three clefts are present in the LpxA structure. Alanine substitution of His125, which is strictly conserved, completely abrogated LpxA activity, suggesting that it may act as a catalytic base by activating the 3-hydroxy group of UDP-GlcNAc (99). Furthermore, it was proposed that the remaining basic residues are involved in substrate recognition as mutating them to alanine reduced, but did not completely eliminate, LpxA activity (99). The structure of *E. coli* LpxA with UDP-GlcNAc was later solved, which corroborated the role of these residues in UDP-GlcNAc binding, and revealed the involvement of the C-terminal helices in coordinating the uracil moiety of the substrate (Fig. 1.16) (100). A number of residues localized to helix $\alpha1$ of the C-terminal domain form a pocket that interacts with the uracil nucleotide. For example, Asn198 forms hydrogen bonds to the nitrogen and oxygen atoms of the uracil ring. Although LpxA has been shown to be highly specific for uridine, it can process thymidine diphosphate-GlcNAc (TDP-GlcNAc), albeit at 20% of the rate of UDP-GlcNAc (62). This can be explained by the fact that TDP and UDP are of similar size. Although cytidine diphosphate (CTD) is also comparable in size, its hydrogen bonding profile is rather different than UDP, thus providing a rationale as to why LpxA cannot turn over CDP-GlcNAc. The remaining two possible nucleotide-GlcNAc substrates, adenosine diphosphate- and guanosine

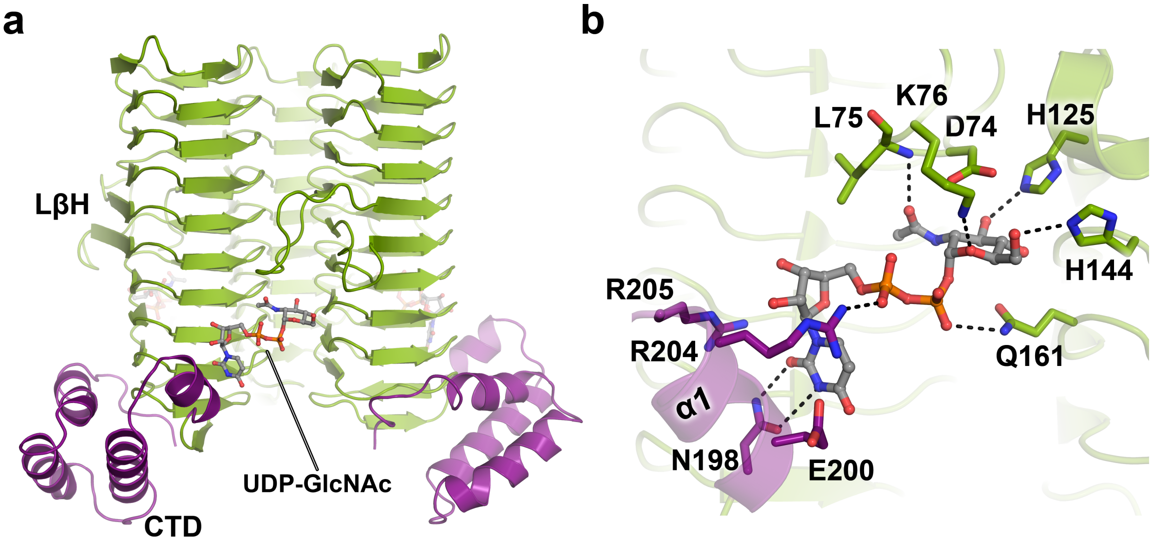

Figure 1.16: LpxA structure bound to UDP-GlcNAc. (a) The active site of LpxA is situated between two adjacent LpxA monomers (PDB code: 2JF3). **(b)** The GlcNAc moiety interacts with the LβH domain, and the uracil group interacts with the CTD. The dotted lines indicate hydrogen bonds. His125 hydrogen bonds with the 3-OH group of the GlcNAc, and its alanine substitution completely eliminates LpxA activity, suggesting that it acts as a catalytic base in the reaction mechanism.

diphosphate-GlcNAc, are bulky and are not able to be accommodated by the uridine binding pocket.

In the case of *E. coli*, LpxA is highly specific for *R*-3-hydroxymyristoyl-ACP (*R*-3OH-C14-ACP), whereas *Leptospira interrogans* and *Pseudomonas aeruginosa* LpxAs are selective for *R*-3-hydroxylauroyl-ACP (R-3OH-C12-ACP) and *R*-3-hydroxydecanoyl-ACP (R-3OH-C10-ACP), respectively (34, 62, 99, 101, 102). Previous studies have demonstrated the molecular basis for selectivity toward varying acyl-chain lengths. For example, substitution of Gly173 with an alanine in *E. coli* LpxA shifts the acyl-chain specificity to C10 (103). Additionally, the selectivity of LpxA from *P. aeruginosa* was shifted to C14-specificity when Met169 was mutated to glycine (103). Therefore, it appears that LpxA utilizes a precise molecular hydrocarbon ruler that selects for the proper length of acyl substrate, and is fine-tuned among various orthologs of LpxA.

The structure of *E. coli* LpxA with its bound lipid product, UDP-3-*O*-(*R*-3-hydroxymyristoyl)-GlcNAc (104), and *L. interrogans* LpxA with UDP-3-*N*-(*R*-3-hydroxylauroyl)-GlcNAc3N (105) have been solved (Fig. 1.17a,b). These structures confirmed the catalytic mechanism deduced from mutagenesis studies (99), and provided structural evidence for the presence of an accurate hydrocarbon ruler within LpxA. In both structures, the acyl-chain is packed inside a hydrophobic pocket shaped by two adjacent LβH domains. In *E. coli* LpxA, Gly173 and His191 form the pocket floor

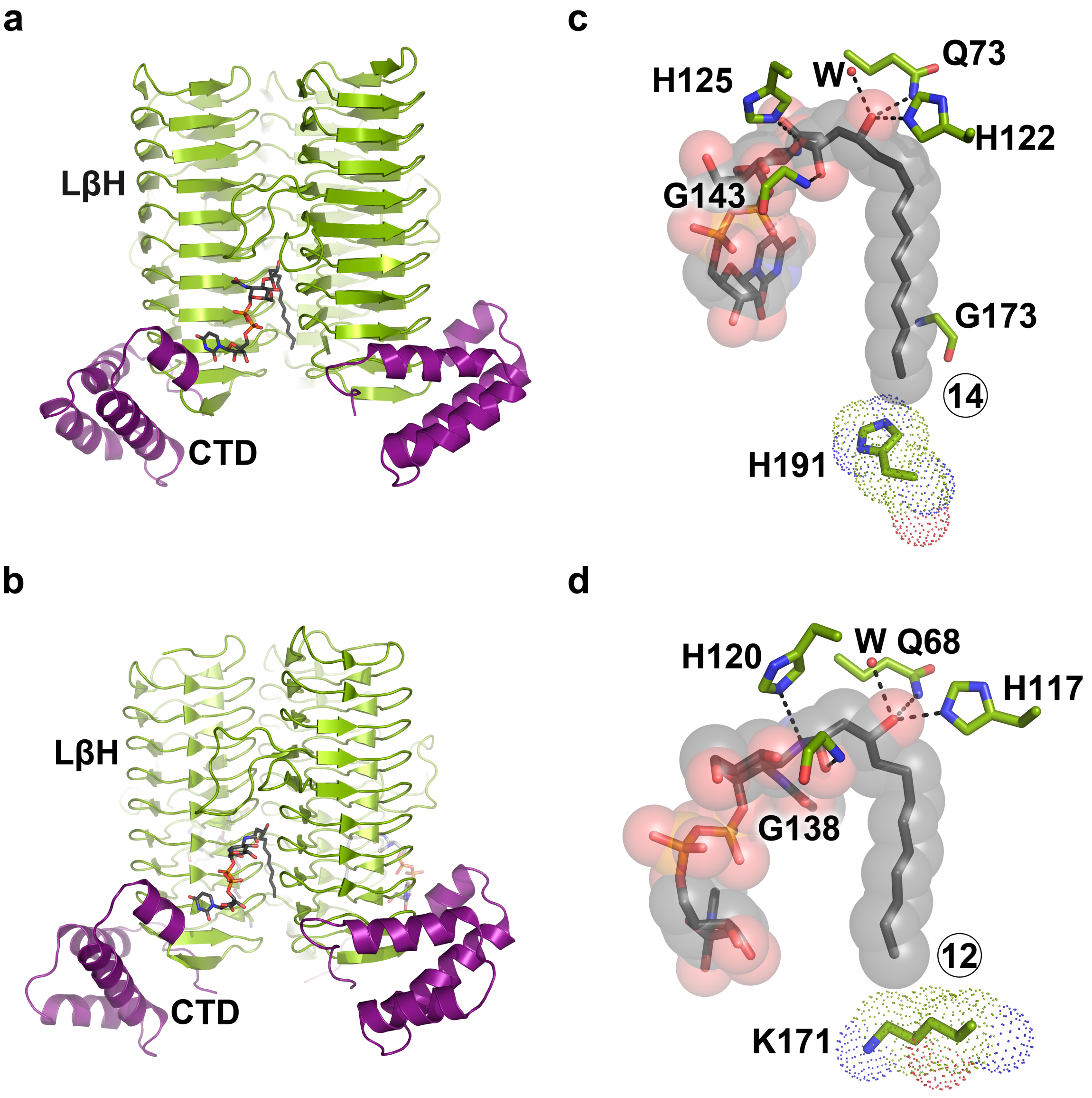

Figure 1.17: LpxA structure bound to its lipid product. (a) *E. coli* LpxA bound to UDP-3-*O*-acyl-GlcNAc (PDB code: 2QIA). **(b)** *L. interrogans* LpxA bound to UDP-3-*N*-acyl-GlcNAc3N (PDB code: 3I3X). The acyl-chain is packed inside a cleft formed by two neighboring LβH domains. **(c,d)** The catalytic histidine (**c**, His125, **d**, His120) is hydrogen bonded to the nucleophile. A strictly conserved glycine residue (c, Gly143, d, Gly138) acts as an oxyanion hole, stabilizing the negatively charged carbonyl oxygen in the transition state. The β-hydroxy group hydrogen bonds with a glutamine, histidine, and a water molecule (W). The acyl-chain length is indicated. His191 is the hydrocarbon ruler in *E. coli* LpxA (**c**), and Lys171 is the hydrocarbon ruler in *L. interrogans* LpxA (**d**).

and dictate the length of the acyl-chain delivered by ACP (Fig. 1.17c). Interestingly, the equivalent hydrophobic pocket in *L. interrogans* LpxA is truncated by Lys171, which explains its specificity for C12 acyl-chain (Fig 1.17d).

All known LpxA variants require β-hydroxy containing acyl-chains for catalysis, with the exception of *Chlamydia trachomatis* LpxA, which shows activity with myristoyl-ACP (106). In fact myristoyl-ACP inhibits *E. coli* LpxA reaction with an IC_{50} value of 2 μM, suggesting an important role for the β-hydroxy group (34). The *E. coli* LpxA structure bound to its lipid product revealed that the β-hydroxy group forms direct hydrogen bonds with His122 and Gln73, and interacts with His99 through a bridging water molecule (104). The same network of hydrogen bonds was also observed between the β-hydroxy group of UDP-3-*N*-(*R*-3-hydroxylauroyl)-GlcNAc3N and the active site cleft of *L. interrogans* LpxA (Fig 1.17c,d) (105). Based on sequence alignment, His122 and Gln73 are conserved, whereas His99 is replaced with a threonine residue in *C. trachomatis* LpxA (106). Further biochemical studies are necessary to show whether this replacement is responsible for loss of specificity of *C. trachomatis* LpxA for β-hydroxyacyl substrates.

Notably, *E. coli* LpxA does not recognize the coenzyme A substrate derivative, suggesting a crucial role of ACP in substrate recognition (36). An NMR-based docking experiment, which utilized the previous mutagenesis studies, suggests that ACP docks in the vicinity of the active site cleft of LpxA (107). Based on chemical shift perturbations, Asp35, Asp38, and Glu41 of ACP form salt bridges with Lys76, and Arg204 of LpxA. However, the structure of *L. interrogans* LpxA solved with acyl-4'-phosphopantetheine suggests that ACP binds to a different region on LpxA, as the 4'-phosphate group of this substrate mimetic is situated 20 Å away from Ser36 of the docked ACP (Fig. 1.18).

Previous attempts have been made to trap the LpxA–ACP complex, however, like other ACP-based complexes this has been proven to be a difficult task. This is primarily because ACP utilizes a "low affinity, high-selectivity' mechanism for acyl substrate delivery. The dissociation constant of LpxA:*holo*-ACP has been reported (K_d = 1.8 μM), which is consistent with the reported K_M of *E. coli* LpxA for its *R*-3-hydroxyacyl-ACP substrate (K_M = 1.2 μM) and the IC_{50} value for non-hydroxyated *acyl*-ACP (IC_{50} =2 μM). Trapping ACP in complex with LpxA will be the focus of Chapter 3, which describes for the first time ACP recognition by LpxA.

LpxA is a potential target for the design of novel antibiotics (108). A pentadecapeptide inhibitor of LpxA, known as peptide-920, has been identified by phage display (109). It is shown that overexpression of peptide-920 in bacteria as a glutathione-S-transferase-fusion protein inhibits growth, which can be rescued by overexpression of LpxA (109). Kinetic studies suggest that peptide-920 inhibits LpxA with a K_i value of 50 nM, and competes with *acyl*-ACP (108). Although the crystal structure of *E. coli* LpxA with peptide-920 has been solved (108), it is not clear whether peptide-920 competes with the acyl-phosphopantetheine moiety of ACP, or if it disrupts direct protein–protein interactions between the two protein partners.

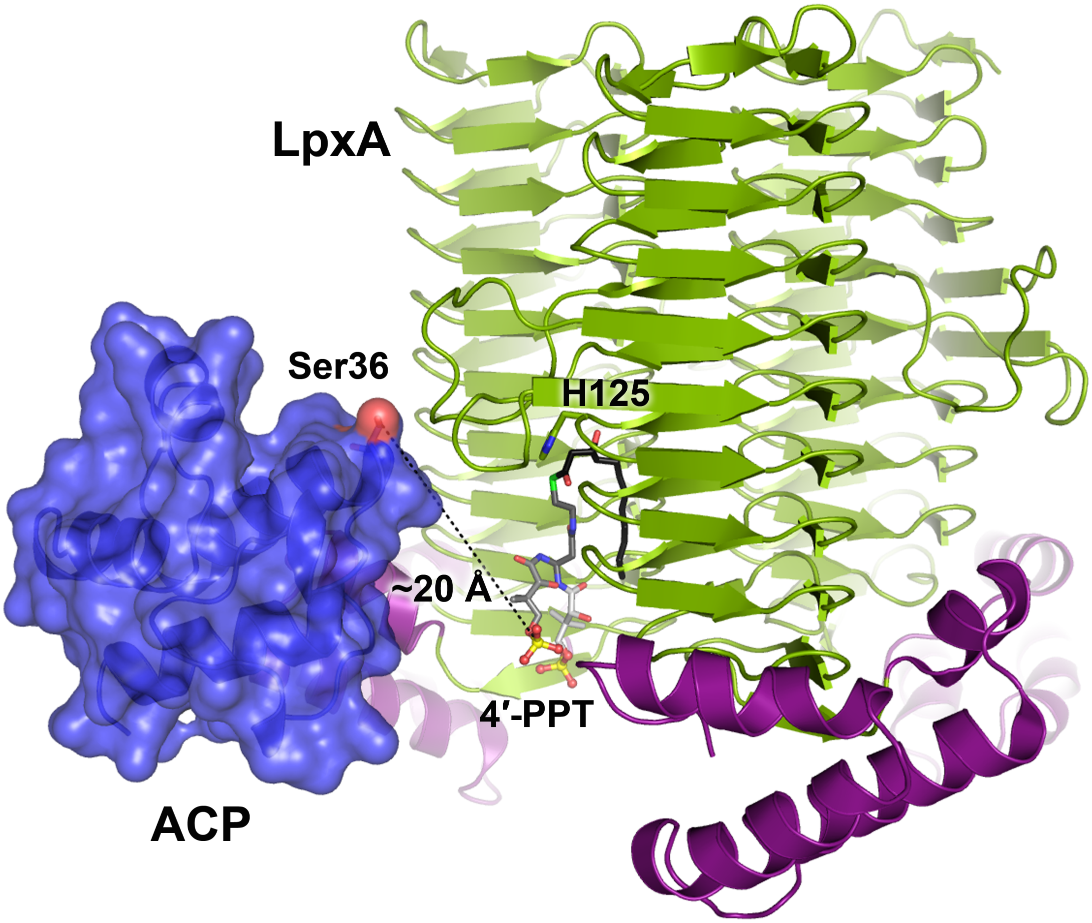

Figure 1.18: Comparing ACP–LpxA docking model with *L. interrogans* LpxA–acyl-4'-phosphopantetheine crystal structure. In the *L. interrogans* LpxA structure, the acyl-chain (black) is packed inside the hydrophobic pocket formed between two LβH domains, and the thioester bond is situated near the catalytic base (*E. coli* LpxA is shown here). Two conformations were observed for the 4'-PPT arm, both of which place the 4'-phosphate group approximately 20 Å away from Ser36 of ACP (blue).

1.8 UDP-3-O-acyl-GlcN acyltransferase (LpxD)

LpxD catalyzes the third step in lipid A biosynthesis by adding an *R*-3-hydroxyacyl-chain to the 2-amine group of UDP-3-*O*-acyl-GlcN (36). LpxD follows an ordered sequential reaction mechanism in which *acyl*-ACP associates with the enzyme prior to UDP-3-*O*-acyl-GlcN (110). An essential histidine residue (His239 in *E. coli* LpxD) acts as a catalytic base to extract a proton from the amine group for nucleophilic attack on the thioester carbonyl of *acyl*-ACP (110). LpxD possesses a strictly conserved glycine residue, which is proposed to stabilize the negatively charged carbonyl oxygen in the transition state (110). After catalysis, UDP-2,3-diacyl-GlcN dissociates from LpxD, followed by *holo*-ACP (110).

The crystal structure of LpxD from *C. trachomatis* (CtLpxD) was first reported in 2007 by Buetow *et*. *al*., verifying the LβH architecture that was previously inferred from the amino acid sequence (Fig. 1.19a) (111). LpxD and LpxA are structurally homologous, however the domain combination of LpxD is distinctive. In addition to the LβH domain, each monomer of LpxD contains an N-terminal domain (NTD) that is composed of a combination of α-helices and β-strands. Unlike LpxA, the C-terminal domain (CTD) of LpxD has only two α-helices that are connected by a short turn. The C-terminal helices from adjacent monomers interact to form a three-helix bundle, however, they do not contribute to the oligometric stability, as their removal does not disrupt the trimeric structure of LpxD (111).

The *E. coli* LpxD (EcLpxD) structure was later reported by Bartling *et. al.,* which was crystallized in the absence of any substrate (Fig. 1.19b) (39). The overall fold of EcLpxD and CtLpxD are similar, however there are some differences in the orientations of the NTD and CTD relative to the LβH domain. The NTD of CtLpxD is tilted approximately +20° relative to the three-fold axis of symmetry, whereas the equivalent domain of EcLpxD is tilted –10° (39). This difference is attributed to the length of the linker region between the NTD and LβH, which is one amino acid shorter for EcLpxD. The most distinctive difference between the two orthologues is in the spatial arrangement of the C-terminal helices (Fig. 1.19c,d). In the case of EcLpxD, the linker region between the LβH and CTD interdigitates with its neighbor. However, in CtLpxD a glycine (Gly310) substitution (Ser303 in EcLpxD) changes this 'crossover' arrangement, yet still enables the CTD to form a three-helix bundle (39).

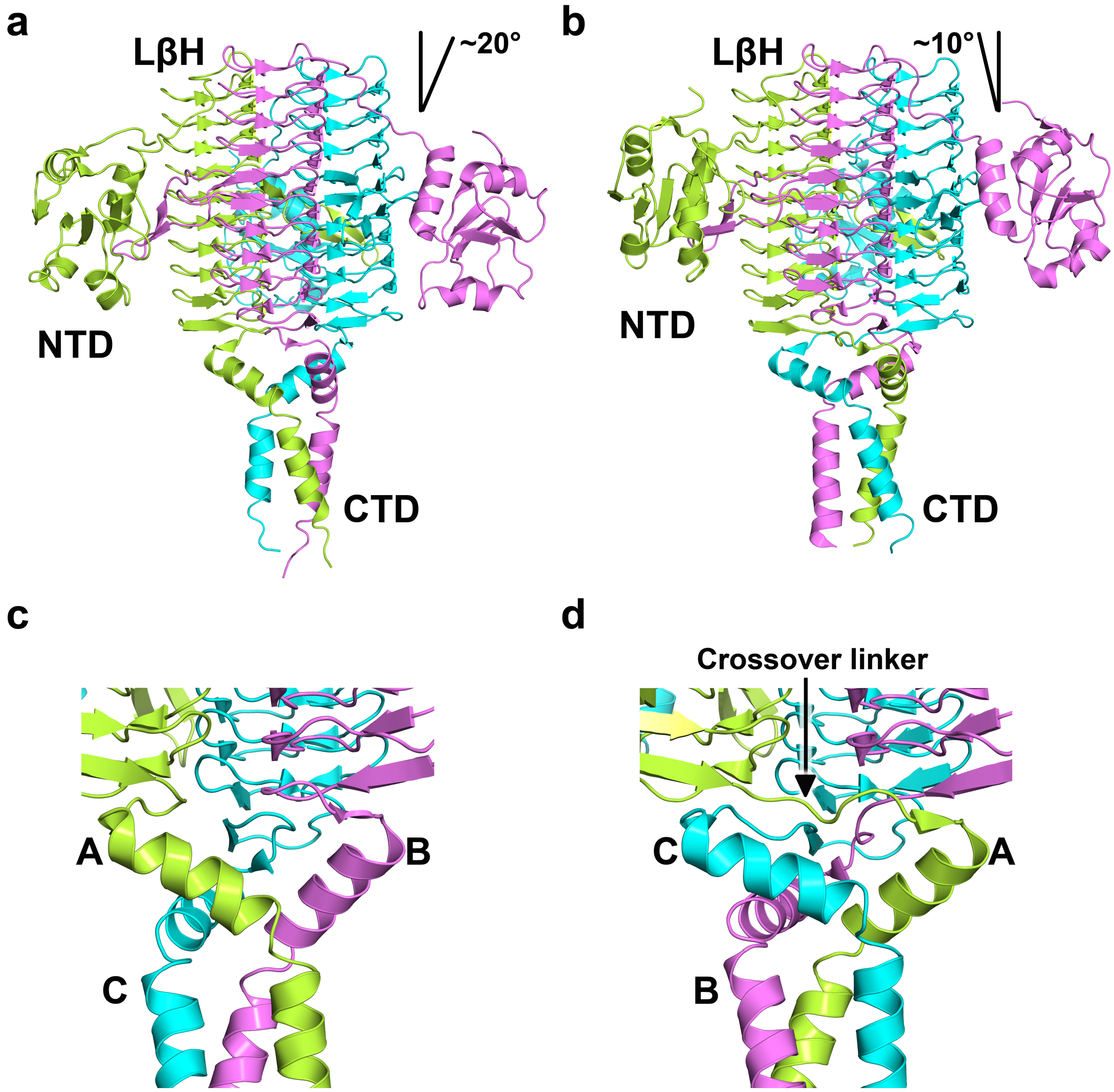

Figure 1.19: Molecular structure of *C. trachomatis* and *E. coli* LpxD. (a) *C. trachomatis* and **(b)** *E. coli* LpxD are trimers with each monomer composed of three domains: NTD, LβH, and CTD. The C-terminal helices form a three-helix bundle. **(c)** C-terminal domain of CtLpxD. The beginning of the first helix is located just below the same monomer. **(d)** C-terminal domain of EcLpxD. The beginning of the first helix is located below the neighboring monomer. Monomers A, B, and C, are colored green, pink, and cyan, respectively. The crossover linker is indicated.

The CtLpxD structure was determined in complex with UDP-GlcNAc and palmitic acid (Fig. 1.20a) (111). UDP-GlcNAc was bound inside a cleft formed by two neighboring LpxD subunits. The uracil interacts with the NTD of one LpxD subunit, and the glucosamine ring is coordinated by the LβH from of the adjacent subunit; the ribose and the diphosphate group cross between the two domains. Phe43 and Tyr49 from the NTD provide Π—Π interactions with the uracil ring. Glu32, Glu34, Gln248, Asp46, and His284 form hydrogen bonds with the ribose and the pyrophosphate group of UDP-GlcNAc (Fig 1.20b). The kinetic studies reported by Bartling *et. al.* confirmed the role of Phe43 and His284 in UDP-3-*O*-acyl-GlcN binding. However, the contribution of the remaining residues in lipid substrate binding could not be verified, as alanine substitution of the equivalent residues in EcLpxD did not raise the K_M value for the lipid substrate significantly.

The palmitate fatty acid was bound to a hydrophobic cavity formed between two neighboring LβH domains (111). Buetow *et*. *al*. claimed that this pocket represents the binding site for the acyl-moiety of the lipid substrate. However, Bartling *et*. *al*. suggested that this pocket is likely the feature that binds the acyl-chain delivered by ACP, which for CtLpxD is 20-carbons in length (39). Notably, in *E. coli* LpxD Met290 truncates the equivalent pocket at one end, and when substituted with an alanine the specificity of EcLpxD shifts from *R*-3-OH-C14-ACP to *R*-3-OH-C16-ACP (39). Furthermore, removal of two-carbons units from *R*-3-OH-C14-ACP, reduces wild-type LpxD specific activity

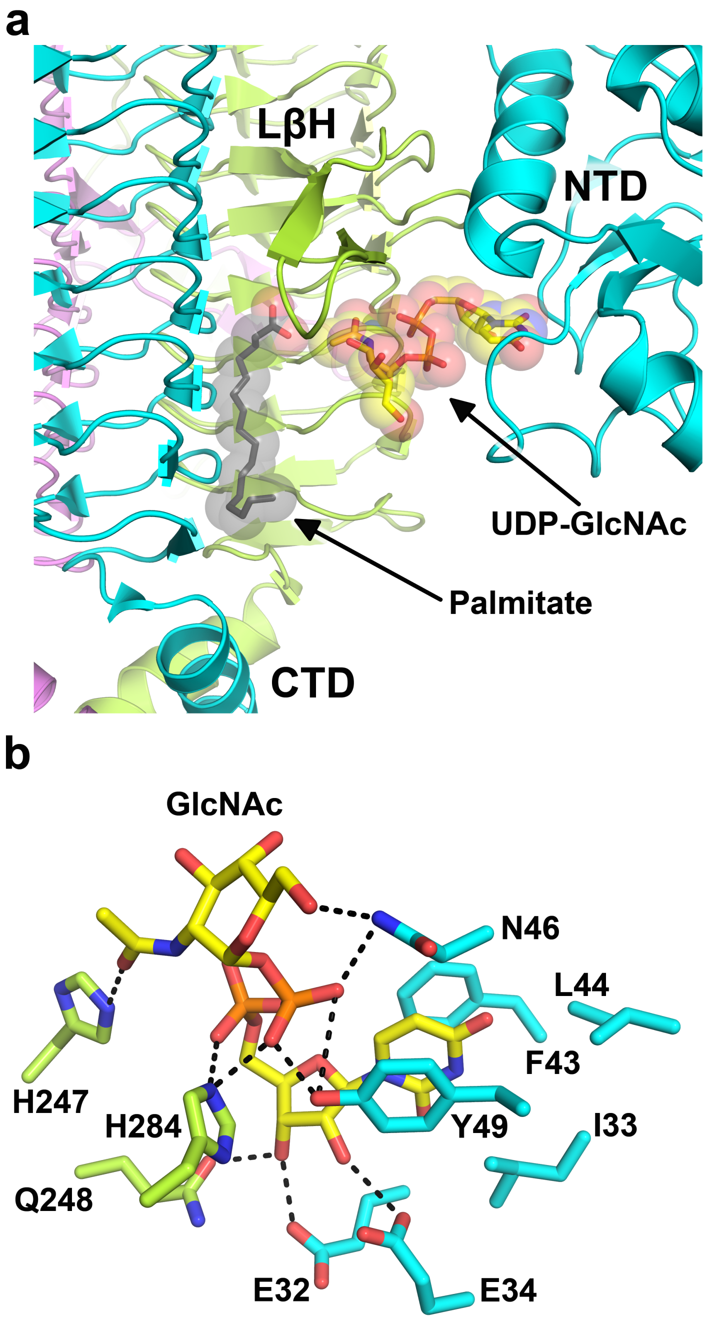

Figure 1.20: CtLpxD bound to UDP-GlcNAc and palmitate. (a) UDP-GlcNAc bridges the NTD and LβH domain. The uracil ring is bound to the NTD and the GlcNAc interacts with the LβH domain. Palmitate is bound between two adjacent LβH domains. **(b)** UDP-GlcNAc interaction with LpxD residues. The dotted lines indicate hydrogen bonds. His247 is proposed to act as a catalytic base. His284 interacts with the pyrophosphate groups. Phe43 and Tyr49 interact with the uracil ring through Π-staking.

by about 10-fold, suggesting the presence of a molecular hydrocarbon ruler (110).

In addition to acyl-chain selectivity, binding of ACP and LpxD is necessary for the successful delivery of acyl-substrates (110). Substitution of *acyl*-ACP with a substrate mimetic, *R*-3-hydroxylauroyl-methylphosphopantetheine, results in a loss of specific activity of more than 1000-fold, suggesting that protein–protein interactions between ACP and LpxD play a key role in the reaction mechanism (110). Divalent cation inhibition of LpxD activity, which can be reversed by addition of excess *acyl*-ACP, further signifies the importance of the protein–protein interaction in LpxD function (110). Although there is no biochemical evidence as to where ACP might dock on LpxD, Buetow *et. al.* utilized structural knowledge to propose that the NTD is involved in recognition of ACP, as it presents an electropositive patch near the UDP-GlcNAc binding locale. Further structural and biochemical studies are required in order to understand how LpxD interacts and recognizes its protein and lipid substrate, and how it acquires its remarkable selectivity for acyl-chain length.

Although the paradigm for ACP interaction is thought to be exceedingly transient, LpxD binds ACP with very high affinity (K_d = 59 nM) (110). Therefore, LpxD represents an excellent model system to study ACP-based interactions and is presented first in Chapter 2. A better understanding of ACP–LpxD may have drug discovery implications as well. Inhibitors of this enzyme might be advantageous over the known

LpxC inhibitors as they may cause buildup of the toxic detergent-like intermediate, UDP-3-*O*-acyl-GlcN, thereby contributing to cell death by a secondary mechanism (110).

Chapter 2. Chasing Acyl-Carrier-Protein Through a Catalytic Cycle of Lipid A Production

Portions of the following chapter have been published in *Nature*, volume 505, pages 422-426, 2014 January 16, and is reprinted with permission.

2.1 Introduction

Acyl-carrier-protein (ACP) represents one of the most highly conserved proteins across all domains of life and is nature's way of transporting hydrocarbon-chains *in vivo*. Type II ACPs found in most microorganisms and plants are small (70-100 residues), dissociated proteins with the ability to diffuse freely throughout the cytosol (58). Notably, type II ACPs have evolved the ability to associate with a substantial number of larger enzymes for efficient delivery of a broad assortment of acyl-substrates linked to their prosthetic 4′-phosphopantetheine (4′-PPT) group (56). ACPs of bacteria serve as a crucial interaction hub within primary cellular metabolism (67) by communicating transiently between partner enzymes of the numerous biosynthetic pathways. The highly transient nature of such interactions and the inherent conformational mobility of ACP (56) have stymied previous attempts to structurally visualize ACP tied to an overall catalytic cycle, which is essential to understanding a fundamental aspect of cellular metabolism leading to compounds that are not only useful to the cell, but are also of therapeutic value.

In addition to their well-defined roles in fatty acid and phospholipid biogenesis, ACPs are essential in the biosynthesis of lipid A (Raetz Pathway). The unique cell envelope of Gram-negative microorganisms requires lipid A (endotoxin), which serves as the anchoring unit of lipopolysaccharides (LPS) to the outer membrane leaflet (5). Lipid A is required for the growth and survival of most Gram-negative pathogens (112, 113) and activates the mammalian host's immune system (114, 115), thus emerging as an important therapeutic target for novel, broad-spectrum anti-infectives (116). In *Escherichia coli*, lipid A synthesis is an assembly line of nine discrete enzymes comprised of cytosolic, peripheral- and integral-membrane proteins (Fig. 2.1a). Central to this pathway is the thioester-activated, *acyl*-ACP which shuttles *R*-3-hydroxymyristoyl (β-OH-C_{14}), lauroyl (C_{12}), or myristoyl (C_{14}) intermediates among four ACP-dependent acyltransferases: LpxA, LpxD, LpxL, and LpxM. Of these, the crystal structures of both LpxA and -D have been reported and revealed an unusual left-handed, β-helical fold that forms the core of the homo-trimerization interface (37, 39).

LpxD is strictly dependent on ACP-mediated delivery, and highly specific for the transfer of β-OH-containing acyl-chains that measure 14-carbons in length to uridine diphosphate 3-O-(β-OH-C_{14})-α-D-glucosamine (UDP-acyl-GlcN) (110). The acyl-chain delivered by ACP has been proposed to bind a pronounced hydrophobic channel (*N*-channel) formed between LpxD monomers, which serves as a molecular 'hydrocarbon-ruler'. The conserved catalytic histidine, His239 in *E. coli* LpxD (Fig. 2.2a), activates the amino-group of GlcN, which attacks the thioester scissile bond of *acyl*-ACP generating an amide (*N*-linkage) at the 2-position of the sugar (Fig. 2.1b), as opposed to an ester (*O*-linkage) catalyzed by the preceding LpxA acyltransferase. Presumably a second channel exists (*O*-channel) on the surface of LpxD that accommodates the ester-linked acyl-chain of the lipid substrate. Strictly dependent on ACP-mediated delivery, LpxD is incapable of catalyzing acyl-transfer when the carrier-protein component is replaced with either coenzyme A (CoA) or pantetheine (110). Interestingly, LpxD binds ACP with high affinity (K_d = 59 nM) and uses an ordered sequential kinetic mechanism in which *acyl*-ACP binds first and, importantly, *holo*-ACP dissociates last (110). Given the canonical mode of ACP-mediated transfer is often highly transient, thereby permitting the rapid exchange between protein partners (72), such pronounced association between these protein partners is most unusual. This suggests that the 'strong, transient' ACP-LpxD interaction requires a yet to be identified 'molecular trigger' for dissociation (117) and offers a unique opportunity to gain the detailed molecular basis for ACP-based acyl-delivery and protein–protein communication more generally.

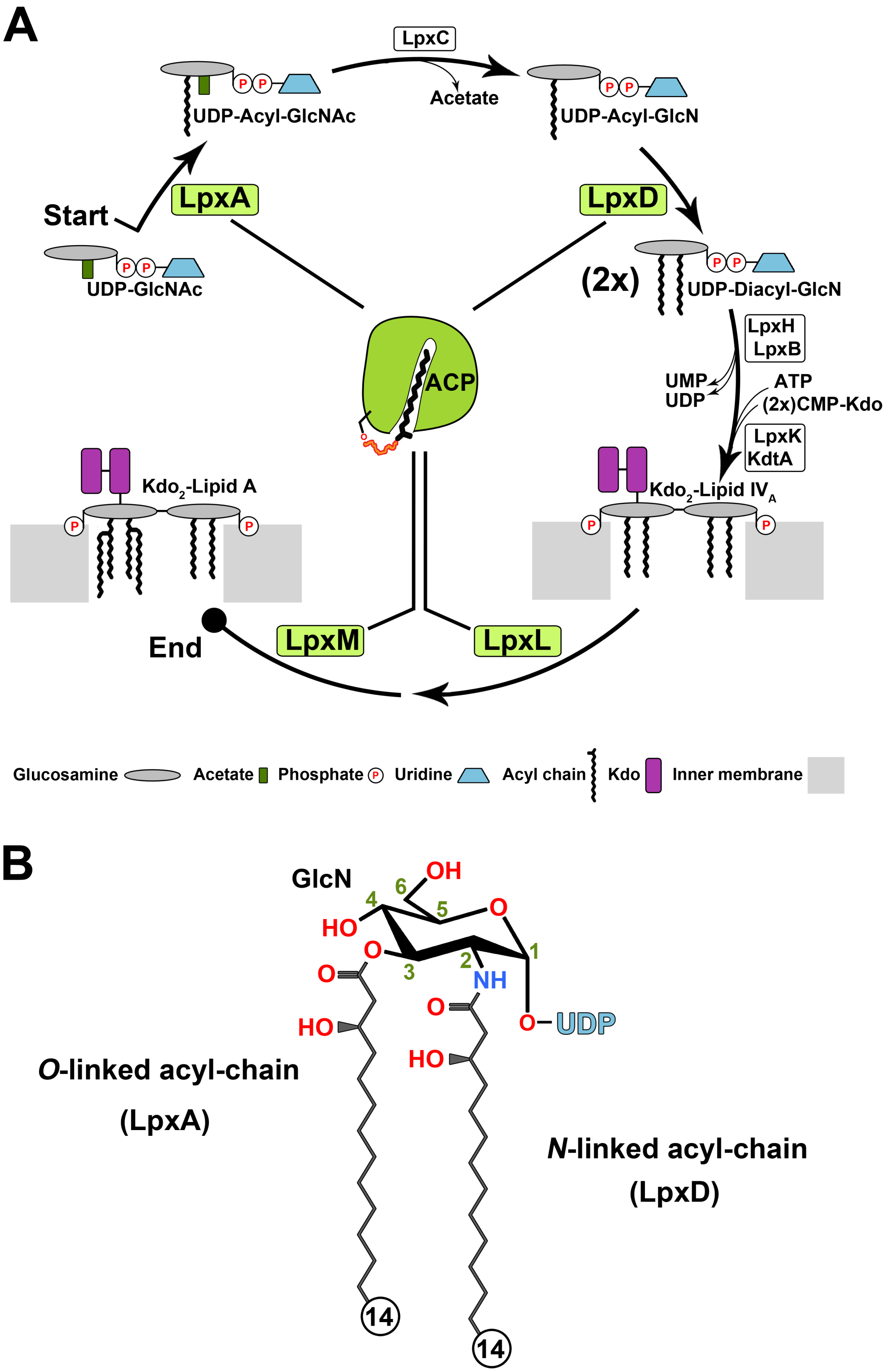
A
LpxC
Acetate
UDP-Acyl-GlcNAc
UDP-Acyl-GlcN
Start
LpxA
LpxD
UDP-GlcNAc
(2x)
UDP-Diacyl-GlcN
LpxH
LpxB
UMP
UDP
ATP
(2x)CMP-Kdo
ACP
LpxK
KdtA
Kdo$_2$-Lipid A
Kdo$_2$-Lipid IV$_A$
P
End
LpxM
LpxL
Glucosamine
Acetate
Phosphate
Uridine
Acyl chain
Kdo
Inner membrane
B
GlcN
OH
HO
O
NH
O–UDP
HO
1
2
3
4
5
6
14
O-linked acyl-chain
(LpxA)
N-linked acyl-chain
(LpxD)

Figure 2.1: Biosynthesis of Kdo$_2$-lipid A in *E. coli*. **(a)** Nine constitutive enzymes (Lpx) and *acyl*-ACP (green) coordinate to assemble Kdo$_2$-lipid A (Kdo, 3-deoxy-D-*manno*-oct-2-ulosonic acid). Two equivalents of UDP-diacyl-GlcN, as indicated by (2x), are required to generate Kdo$_2$-Lipid IV$_A$, which represents the tetra-acylated disaccharide decorated with two Kdo sugars. Highlighted are the four ACP-dependent acyltransferases (green boxes). **(b)** Chemical structure of the LpxD reaction product, UDP-diacyl-GlcN. Acyl-transfer occurs at the 2-position of the GlcN ring, generating an amide-linked *β-OH-C*$_{14}$ substituent, as opposed to the ester-linked *β-OH-C*$_{14}$ acyl-chain at the 3-position catalyzed by the preceding LpxA acyltransferase. LpxD is highly specific for the transfer of *β-OH*-containing acyl-chains that measure 14-carbons in length.

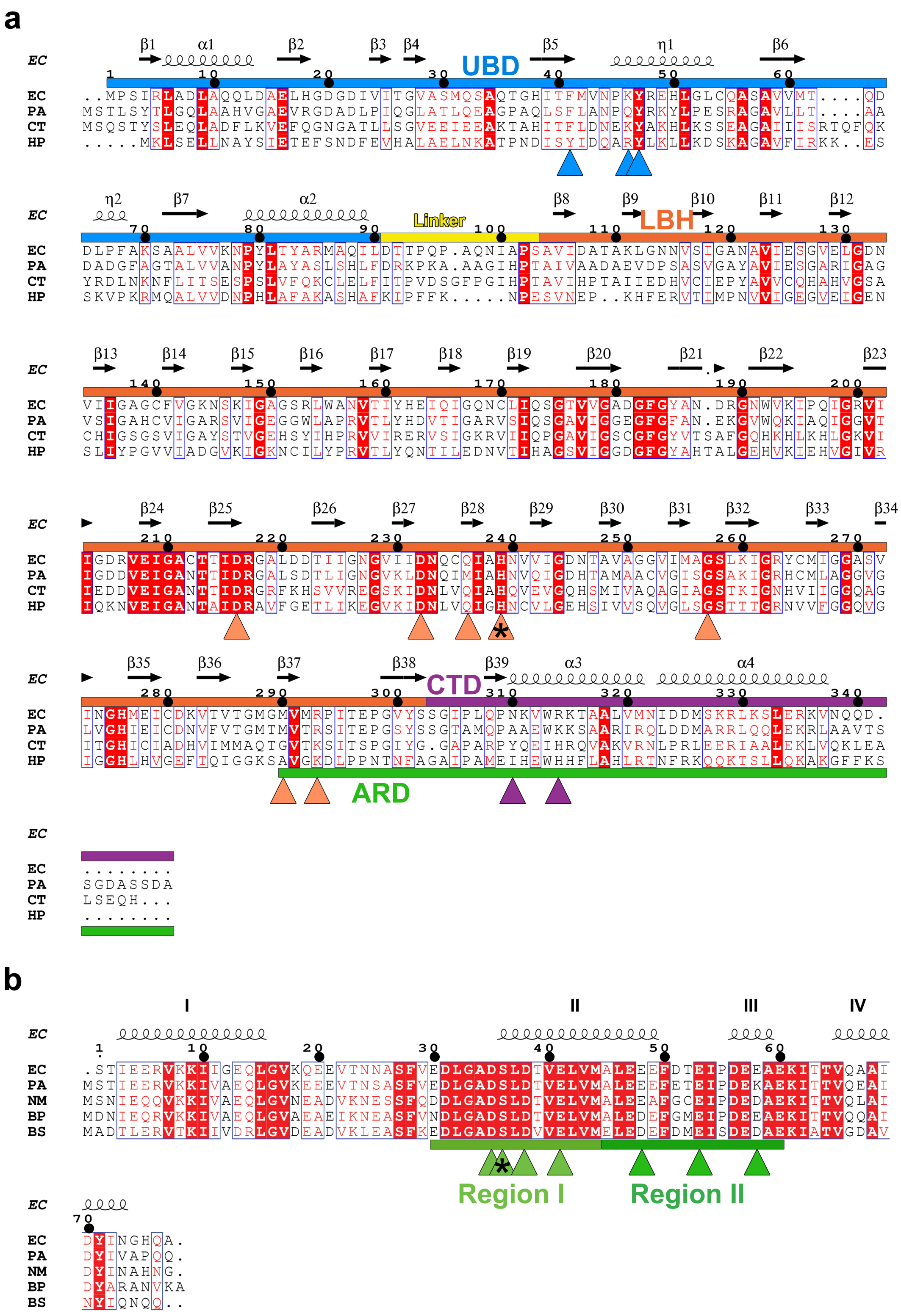a
β1 α1 β2 β3 β4 β5 η1 β6
UBD
EC ..MPSIRLADLAQQLDAELHGDGDIVITGVASMQSAQTGHITFMVNPKYREHLGLCQASAVVMT....QD
PA MSTLSYTLGQLAAHVGAEVRGDADLPIQGLATLQEAGPAQLSFLANPQYRKYLPESRAGAVLLT....AA
CT MSQSTYSLEQLADFLKVEFQGNGATLLSGVEEIEEAKTAHITFLDNEKYAKHLKSSEAGAIISRTQFQK
HP .....MKLSELLNAYSIETEFSNDFEVHALAELNKATPNDISYIDQARYLKLLKDSKAGAVFIRKK..ES
η2 β7 α2 β8 β9 β10 β11 β12
Linker
LBH
EC DLPFAKSALVVKNPYLTYARMAQILDTTPQP.AQNIAPSAVIDATAKLGNNVSIGANAVIESGVELGDN
PA DADGFAGTALVVANPYLAYASLSHLFDRKPKA.AAGIHPTAIVAADAEVDPSASVGAYAVIESGARIGAG
CT YRDLNKNFLITSESPSLVFQKCLELFITPVDSGFPGIHPTAVIHPTAIIEDHVCIEPYAVVCQHAHVGSA
HP SKVPKRMQALVVDNPHLAFAKASHAFKIPFFK.....NPESVNEP..KHFERVTIMPNVVIGEGVEIGEN
β13 β14 β15 β16 β17 β18 β19 β20 β21 β22 β23
EC VIIGAGCFVGKNSKIGAGSRLWANVTIYHEIQIGQNCLIQSGTVVGADGFGYAN.DRGNWVKIPQIGRVI
PA VSIGAHCVIGARSVIGEGGWLAPRVTLYHDVTIGARVSIQSGAVIGGEGFGFAN.EKGVWQKIAQIGGVT
CT CHIGSGSVIGAYSTVGEHSYIHPRVVIRERVSIGKRVIIQPGAVIGSCGFGYVTSAFGQHKHLKHLGKVI
HP SLIYPGVVIADGVKIGKNCILYPRVTLYQNTILEDNVTIHAGSVIGGDGFGYAHTALGEHVKIEHVGIVR
β24 β25 β26 β27 β28 β29 β30 β31 β32 β33 β34
EC IGDRVEIGACTTIDRGALDDTIIGNGVIIDNQCQIAHNVVIGDNTAVAGGVIMAGSLKIGRYCMIGGASV
PA IGDDVEIGANTTIDRGALSDTLIGNGVKLDNQIMIAHNVQIGDHTAMAACVGISGSAKIGRHCMLAGGVG
CT IEDDVEIGANTTIDRGRFKHSVVREGSKIDNLVQIAHQVEVGQHSMIVAQAGIAGSTKIGNHVIIGGQAG
HP IQKNVEIGANTAIDRAVFGETLIKEGVKIDNLVQIGHNCVLGEHSIVVSQVGLSGSTTTGRNVVFGGQVG
*
β35 β36 β37 β38 β39 α3 α4
CTD
EC INGHMEICDKVTVTGMGMVMRPITEPGVYSSGIPLQPNKVWRKTAALVMNIDDMSKRLKSLERKVNQQD.
PA LVGHIEICDNVFVTGMTMVTRSITEPGSYSSGTAMQPAAEWKKSAARIRQLDDMARRLQQLEKRLAAVTS
CT ITGHICIADHVIMMAQTGVTKSITSPGIYG.GAPARPYQEIHRQVAKVRNLPRLEERIAALEKLVQKLEA
HP IGGHLHVGEFTQIGGKSAVGKDLPPNTNFAGAIPAMEIHEWHHFLAHLRTNFRKQQKTSLLQKAKGFFKS
ARD
EC ....
PA SGDASSDA
CT LSEQH...
HP ....
b
I II III IV
EC .STIEERVKKIIGEQLGVKQEEVTNNASFVEDLGADSLDTVELVMALEEEFDTEIPDEEAEKITTVQAAI
PA MSTIEERVKKIVAEQLGVKEEEVTNSASFVEDLGADSLDTVELVMALEEEFETEIPDEKAEKITTVQEAI
NM MSNIEQQVKKIVAEQLGVNEADVKNESSFQDDLGADSLDTVELVMALEEAFGCEIPDEDAEKITTVQLAI
BP MDNIEQRVKKIVAEQLGVAEAEIKNEASFVNDLGADSLDTVELVMALEDEFGMEIPDEEAEKIATVQQAI
BS MADTLERVTKIIVDRLGVDEADVKLEASFKEDLGADSLDVVELVMELEDEFDMEISDEDAEKIATVGDAV
*
Region I
Region II
EC DYINGHQA.
PA DYIVAPQQ.
NM DYINAHNG.
BP DYARANVKA
BS NYIQNQQ..

Figure 2.2: Sequence alignment of LpxD and ACP homologs. Secondary structure assignment and residue numbers are presented above and are for *E. coli* LpxD or ACP. Red boxes indicate strictly conserved residues and red single letter amino acids show those that are partially conserved. **(a)** The amino acid sequence alignment of *E. coli* (EC) LpxD with *Pseudomonas aeruginosa* (PA), *Chlamydia trachomatis* (CT), and *Helicobacter pylori* (HP). The blue, yellow, orange, and purple bars above the aligned sequences indicate the uridine binding domain (UBD), linker region, left-handed β-helix domain (LβH), and the C-terminal domain (CTD), respectively. The ACP recognition domain (ARD) is indicated by a green bar and is presented below the alignment. Residues that contribute to catalysis and substrate specificity are indicated by triangles that are color matched according to domain association; the catalytic His293 is indicated with an asterisk. The Met290 residue which serves as the molecular 'hydrocarbon ruler' for *E. coli* LpxD is also indicated. Although this is indeed the case for *E. coli* LpxD, orthologs often have other chain-length specificity and, thus require fine-tuning of the 'hydrocarbon ruler,' for example with *C. trachomatis* LpxD which incorporates a twenty-carbon acyl-chain[12]. **(b)** Amino acid sequence alignment of ACPs from *E. coli* (EC), *Pseudomonas aeruginosa* (PA), *Neisseria meningitidis* (NM), *Burkholderia pseudomallei* (BP), and *Bacillus subtilis* (BS). The primary sequence of ACP begins with methionine, which for historical reasons (i.e. due to aminopeptidase action) is numbered zero and the serine that is next in sequence is denoted number one. Regions I and II are indicated by light and dark green bars, respectively. Key residues that make strong electrostatic interactions within regions I and II are indicated by triangles that are color matched according to their acidic region association. An asterisk indicates the canonical phosphopantetheinylated serine (Ser36) residue.

2.2 Results

2.2.1 Overview of the ACP-LpxD complexes

We determined three co-crystal structures of ACP bound to LpxD, each of which captured a different form of the carrier-protein: *intact-acyl*-ACP, *hydrolysed-acyl*-ACP, and *holo*-ACP (Fig. 2.3). In doing so, our structures visualize stalled substrate-intermediate and liberated products during the acyl-delivery process. These structures crystallized in the *P*1 spacegroup and were resolved to 2.1 Å, 2.9 Å, and 2.15 Å resolution, respectively (Table 2.1). In each case, the triclinic unit cell contained two LpxD trimers with different bound states of ACP (Fig. 2.4). It is well established that the biologically functional unit of LpxD is a single trimer; the fact that there is a dimer of trimers in asymmetric unit is most likely an artifact of crystallization. In the *intact-acyl*-ACP complex we observed three molecules of the carrier-protein bound per trimer of LpxD. However, in both the *hydrolysed*- and *holo*-ACP complexes we observed weak density for ACP in two or three of the six total LpxD active sites in which only portions of ACP could be modeled, possibly representing dynamically disordered ACPs. It is worth mentioning that ACP was mixed with LpxD at equal molar concentrations prior to crystallization, which may contribute to partial docking of carrier-protein; however, increasing the ACP concentration during crystallization had no effect on the ratio of bound ACP. The overall B-values for all ACPs modeled in each structure are 2-3 fold

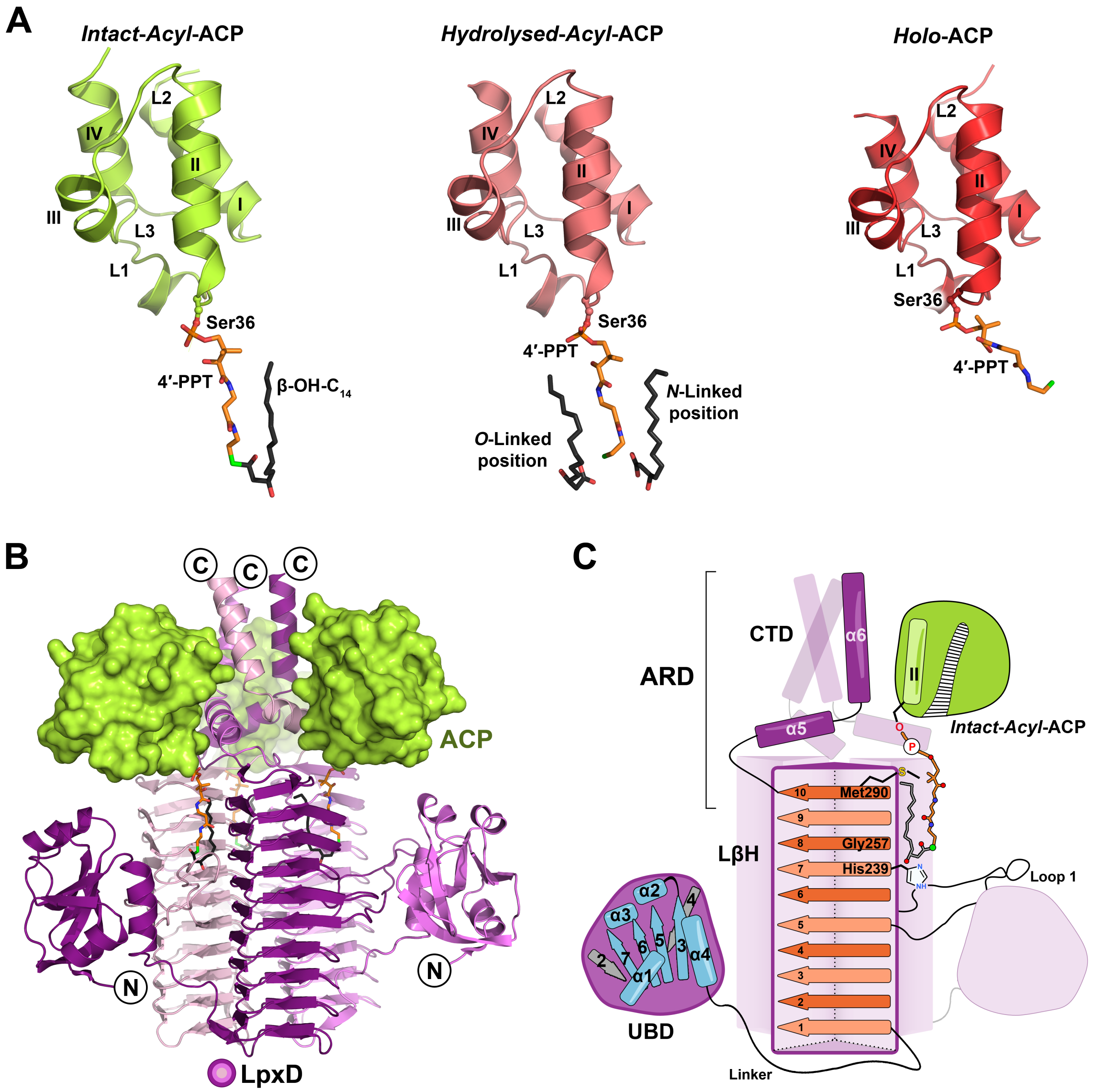
A
Intact-Acyl-ACP
IV
L2
II
III
I
L3
L1
Ser36
4′-PPT
β-OH-C_{14}
Hydrolysed-Acyl-ACP
IV
L2
II
III
I
L3
L1
Ser36
4′-PPT
N-Linked position
O-Linked position
Holo-ACP
L2
IV
II
III
I
L3
L1
Ser36
4′-PPT
B
C
C
C
ACP
N
N
LpxD
C
ARD
CTD
α6
II
α5
Intact-Acyl-ACP
O
P
S
LβH
10
Met290
9
8
Gly257
7
His239
6
5
4
3
2
1
Loop 1
α2
α3
4
2
7
6
5
3
α4
α1
UBD
Linker

Figure 2.3: Stalled ACPs bound to LpxD. **(a)** The three forms of ACP: *intact-acyl*-ACP (green), *hydrolysed-acyl*-ACP (salmon), and *holo*-ACP (red). ACP adopts a 4-helix bundle (I-IV) with several loop regions (L1-L3). The 4′-PPT arm and acyl-chains are shown as stick models and colored orange or dark gray, respectively, and by atom. **(b)** Overall architecture of the ACP-LpxD complex. For simplicity, only the representative *intact-acyl*-ACP structure is shown. Three ACPs (green) bind the carboxy-terminal end of the LpxD trimer (colored by chain purple/magenta/light pink). **(c)** Cartoon rendering showing the overall fold and interaction of *acyl*-ACP with LpxD. Highlighted dark purple is a single monomer of LpxD with the subdomains indicated: uridine binding domain (UBD), left-handed β-helix domain (LβH), and C-terminal domain (CTD). ACP, interfacing with the ACP recognition domain (ARD), and its *acyl*-4′-PPT group is shown. The locations of the catalytic base (His239), the oxyanion hole (Gly257), and the molecular 'hydrocarbon ruler' (Met290) are indicated within the ten β-helical coils (orange strands) of a single LβH.

Table 2.1: Data collection and refinement statistics.

	Intact-Acyl-ACP (His239Ala-LpxD)	*Hydrolysed-Acyl*-ACP (wild-type-LpxD)	*Holo*-ACP (wild-type-LpxD)
Data collection*			
Space group	*P*1	*P*1	*P*1
Cell dimensions			
a, *b*, *c* (Å)	84.30, 89.44, 112.25	84.18, 89.31, 111.93	89.47, 93.23, 114.30
α, β, γ (°)	104.06, 92.40, 118.47	104.09, 92.58, 118.64	75.93, 73.81, 58.95
No. of Reflections	561496	235456	858856
No. of Unique Reflections	154031	59734	160164
Resolution (Å)	50-2.10 (2.14-2.10)	50-2.90 (2.95-2.90)	50-2.15 (2.19-2.15)
R_{sym} or R_{merge}	0.10 (0.40)	0.09 (0.19)	0.09 (0.64)
$I / \sigma I$	14.6 (2.3)	13.8 (5.6)	21.9 (1.9)
Completeness (%)	97.7 (94.9)	98.3% (91.1)	96.1 (85.6)
Redundancy	3.6 (3.1)	3.9 (3.7)	5.4 (4.0)
Refinement			
Resolution (Å)	43.38–2.10	28.43–2.89	35.89–2.13
No. reflections	145543	57571	159778
R_{work}/ R_{free} (%)	16.8 / 21.6	20.4 / 25.3	17.8 / 21.6
No. atoms / *B*-factors			
LpxD	14835/39.1	14688/39.3	14914/32.1
ACP	3433/79.9	2631/78.6	2438/79.5
β-OH-C$_{14}$-4′-PPT	222/43.0	—	—
β-OH-C$_{14}$OOH	—	136/36.5	—
4′-PPT	—	126/37.3	126/54.6
Water	919/42.5	145/30.4	885/34.8
R.m.s deviations			
Bond lengths (Å)	0.01	0.01	0.01
Bond angles (º)	1.05	0.97	1.03
Ramachandran statistics			
Favored (%)	97.6	97.1	98.1
Disallowed (%)	0.0	0.0	0.0

Data were collected from a single crystal for each complex.

*Highest resolution shell is shown in parenthesis.

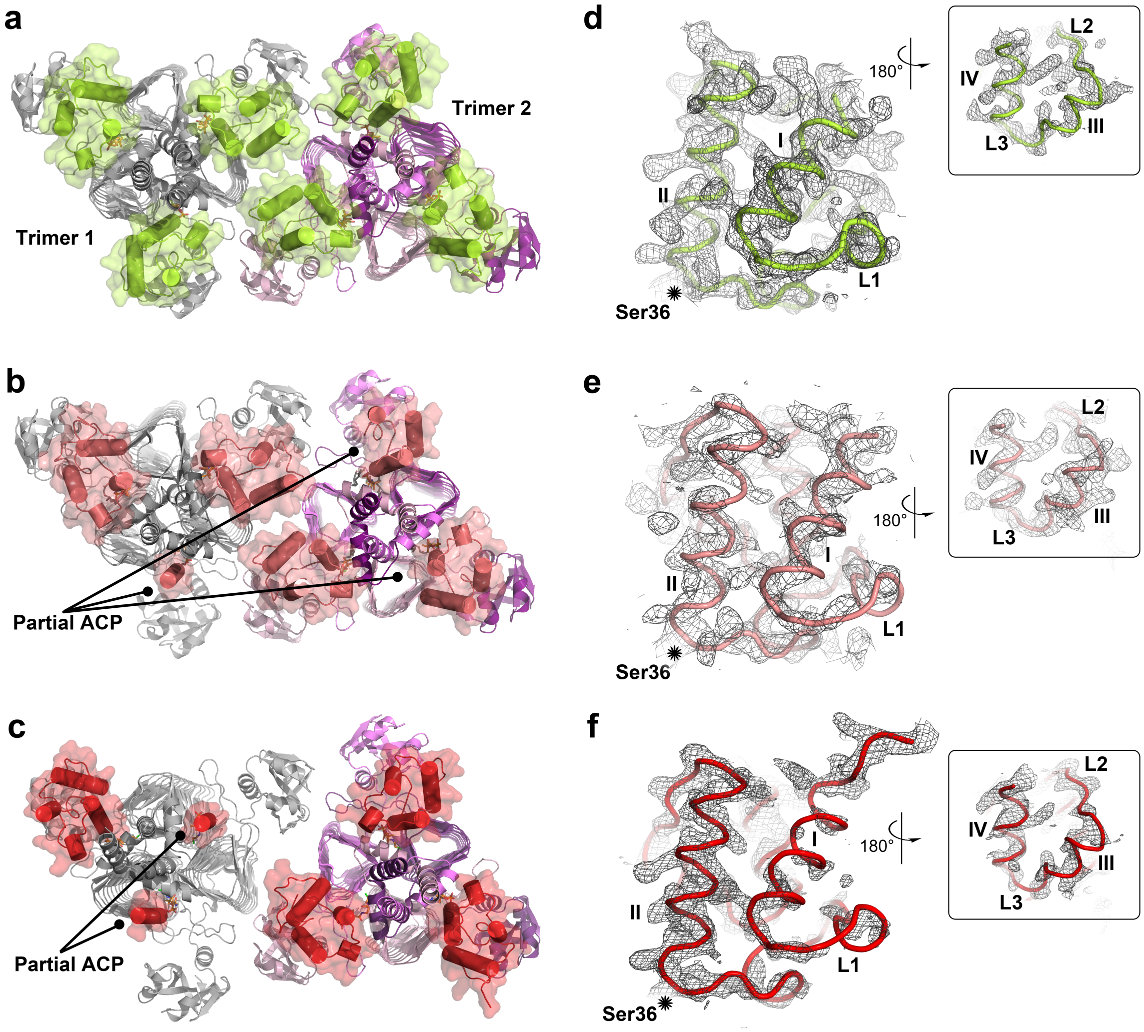

Figure 2.4: The asymmetric unit contents of the **(a)** *intact-acyl*-ACP **(b)** *hydrolysed-acyl*-ACP and **(c)** *holo*-ACP structures in complex with LpxD. Two trimers of LpxD (gray or colored as in figure 1) were observed in the triclinic unit cell. Six molecules of ACP were completely modeled in the *intact-acyl*-ACP structure (green with transparent molecular surface). In the *hydrolysed*- and *holo*-ACP structures (salmon or red with transparent molecular surfaces, respectively) three or two molecules of ACP were partially modeled. Representative molecules of **(d)** *intact-acyl*-ACP (chain H) **(e)** *hydrolysed-acyl*-ACP (chain J) and **(f)** *holo*-ACP (chain J) with $2F_o - F_c$ composite omit electron density covering each α-carbon trace, contoured at 0.9 σ. (inset) Rotated view showing the backside of ACP.

higher than LpxD (Fig. 2.5 and Table 2.1). Accordingly, the observed electron density for fully modeled *intact-*, *hydrolysed-*, and *holo-*ACP was weaker in some regions especially on the solvent exposed faces (Fig. 2.4) – further implicating conformational heterogeneity throughout the lattice. Nonetheless, the placement of side-chains was apparent at the protein–protein interface.

In order to trap the *intact-acyl-*ACP complex, the catalytic His239 of LpxD was mutated to alanine and inspection of the electron density indicates that the thioester scissile bond remained unbroken (Fig. 2.6). By contrast, both the *hydrolysed-* and *holo-*ACP structures were crystallized in the presence of wild-type LpxD enzyme. Electron density for the prosthetic group and acyl-chain of *hydrolysed-acyl-*ACP revealed that the thioester bond was cleaved. This likely occurred through the activation of a water molecule. Serendipitously we discovered a second molecule of β-*OH*-C_{14} fatty acid bound to the surface of LpxD, which likely originated from excess hydrolysis of *acyl-*ACP within the crystallization drop. We have shown by using a gel-based assay that both dithiothreitol (DTT) and LpxD enhance the hydrolysis of *acyl-*ACP (Fig. 2.7). Notably, this molecule of β-*OH*-C_{14} fatty acid likely represents the ester-linked acyl-chain of the lipid substrate. Although the *holo-*ACP lacked any acyl-chain substituent, electron density for its pantetheinyl-group was clear and revealed a different arrangement as compared to the other two complexes.

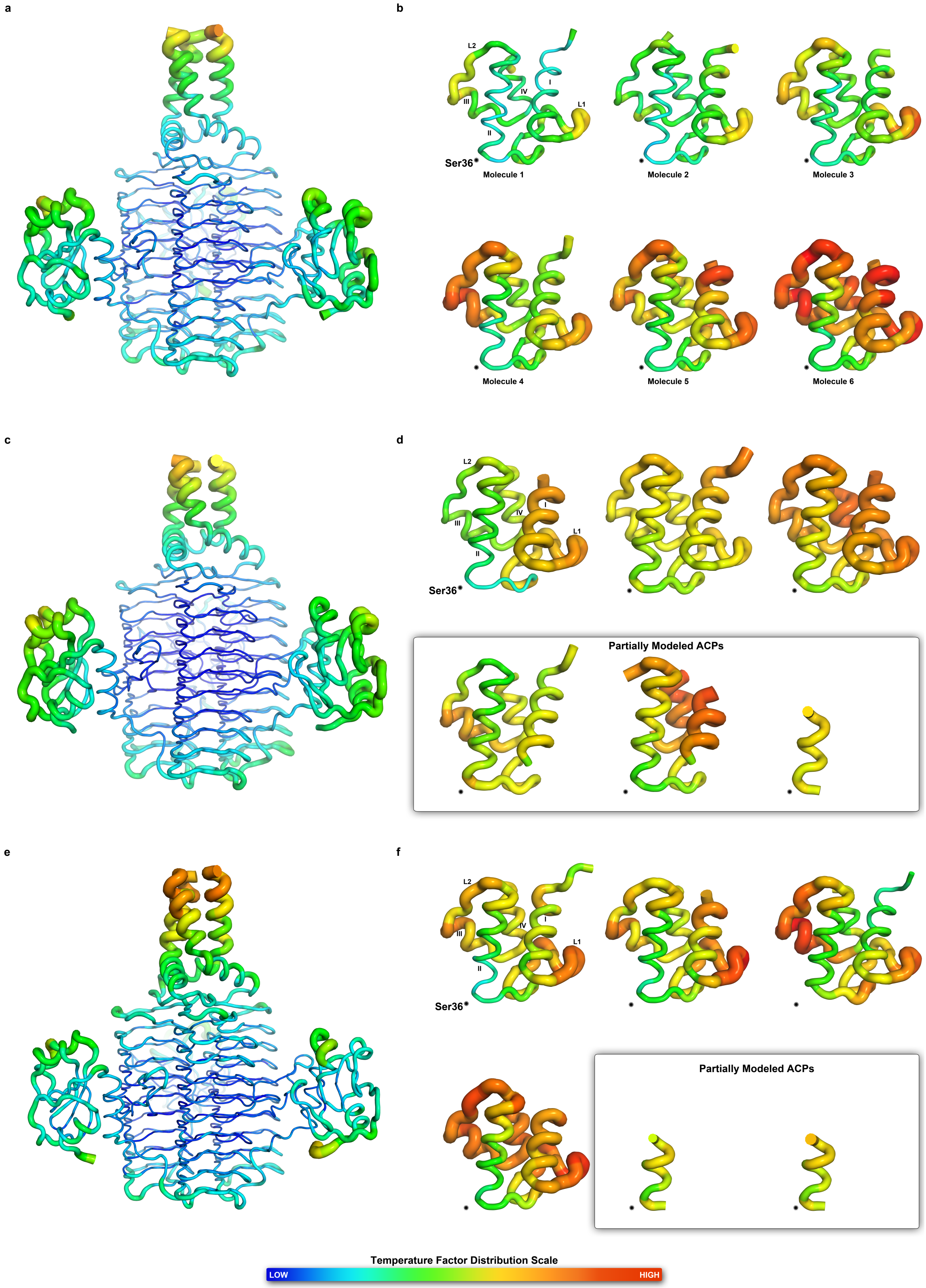
a
b
L2
III
IV
I
L1
II
Ser36
Molecule 1
Molecule 2
Molecule 3
Molecule 4
Molecule 5
Molecule 6
c
d
L2
III
IV
I
L1
II
Ser36
Partially Modeled ACPs
e
f
L2
III
IV
I
L1
II
Ser36
Partially Modeled ACPs
Temperature Factor Distribution Scale
LOW
HIGH

Figure 2.5: Temperature factor distribution of LpxD and ACP between the **(a)** *intact-acyl*-ACP, **(b)** *hydrolysed-acyl*-ACP, and **(c)** *holo*-ACP co-crystal structures. A single trimer of LpxD and all bound ACPs observed in the triclinic unit cell are represented as ribbon-putty diagrams and colored according to main-chain B-value. A scale bar is indicated for the thermal distribution. The subdomains of LpxD are indicated. The location of the pantetheinylated Ser36 residue is indicated with an asterisk symbol and the first ACP molecule of each co-crystal structure is labeled with secondary structural elements. Partially modeled *hydrolysed*- and *holo*-ACPs are accented with a box.

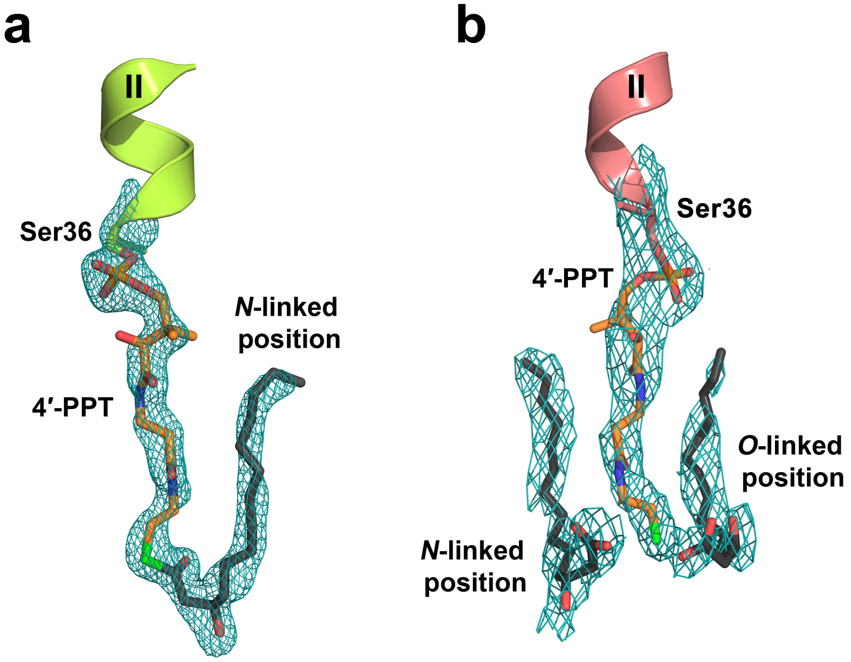

Figure 2.6: 4′-PPT and *β-OH-C14* moieties of **(a)** *intact-acyl*-ACP, **(b)** *hydrolysed-acyl*-ACP, and **(c)** *holo*-ACP that bound in the active site cleft of LpxD. Shown covering Ser36 and the *intact-acyl*-4′-PPT and *holo*-4′-PPT groups is $F_o - F_c$ simulated annealing omit electron density contoured at 3.5 σ. Covering the *hydrolysed-acyl*-4′-PPT group and the *β-OH-C14* fatty acids is $2F_o - F_c$ composite omit electron density contoured at 1.0 σ.

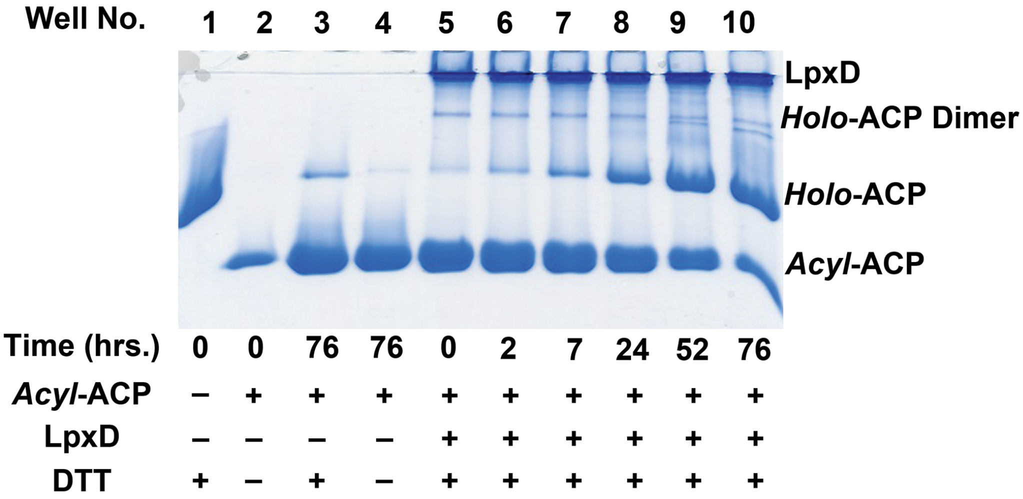

Figure 2.7: Evidence for the hydrolysis of *acyl*-ACP. Conformationally sensitive 2.5 M urea polyacrylamide (19%) gel-shift assay investigating the cleavage of the thioester bond of *acyl*-ACP in the presence (+) or absence (–) of 0.3 mM DTT and LpxD as a function of time. The assay mixture and temperature were kept consistent with the solution used for crystallization (0.1 M MES pH 6.5, 0.2 M ammonium sulfate, 20% PEG 8000, and incubation at 15 ˚C). The well numbers are indicated above the gel. Lanes 1 and 2 indicate *holo*- and *acyl*-ACP, respectively, and serve as controls. *Holo*-ACP even in the presence of DTT shows a weak, higher molecular weight band that corresponds to a disulfide bound form of holo-ACP via the pantetheinyl arm. Lanes 3 and 4 indicate the effect of DTT alone on *acyl*-ACP after 76 hours. Lanes 5 through 10 show *acyl*-ACP in the presence of both DTT and LpxD at the indicated time points. The data indicate an enhancement of *acyl*-ACP hydrolysis by DTT and LpxD.

Similar to other NMR and X-ray structures, ACP adopts a 4-helix bundle (I-IV) with several loop regions (L1-L3) (69, 118-120) and the pantetheine arm is covalently attached to the canonical serine-Oγ oxygen (Ser36 in *E. coli*) located on the 'universal recognition helix' (helix-II) involved in the electrostatic association with partner enzymes (77) (Fig. 2.3a and Fig. 2.6). Previous structural studies have shown that this architecture forms a hydrophobic cavity extending through its core, which is designed to accommodate acyl-chains of varying length, saturation, or hydroxylation (52, 56, 74, 89). By contrast, our structures show the 4′-PPT and its thioester-linked or hydrolysed *β-OH-*C_{14} acyl-chains having vacated this cavity, pivoted about Ser36, and adopted a rather extended conformation – all of which require considerable movement (Fig. 2.8). In doing so, our structures represent the stalled substrate-intermediate and liberated products in the acyl-delivery process.

Despite the fact that LpxD is bound to the *intact-*, *hydrolysed*, and *holo*-forms of ACP, the overall relationship and stoichiometry at the interface between the carrier-protein and LpxD remains consistent. The characteristic *intact-acyl*-ACP structure is represented in FIGURE 2.3b, which reveals three molecules of the carrier-protein localized to the C-terminal end of LpxD. Each monomer of LpxD can be subdivided into three domains (39, 111). First, the N-terminal uridine-binding domain (UBD, residues 1-90), which is tethered to LpxD by a short linker region, binds the uridine-diphosphate moiety of UDP-acyl-GlcN (Fig. 2.3c). Second, and perhaps the most prominent domain is the left-handed β-helix domain (LβH, residues 100-300). It is composed of 10 left-handed, β-helical coils forming a tower-like prism that measures ~45Å in length. The LβH serves as the major trimerization interface (39, 110, 111), forms a possible acyl-chain binding surface (39, 110, 111), and harbors the catalytic His239 residue (110), as well as an extended loop insertion (loop 1) that interrupts the continuity of the β-helical coils and forms part of the catalytic cleft.

Finally, there is a C-terminal domain (CTD, residues 303-341), which is composed of an extended α-helix that is disrupted in its middle by a small kink. The CTD is localized to one end of LpxD, and in the trimer, interdigitates to form a 3-helix bundle. Our structures reveal the ACP recognition domain (ARD), which is formed by the CTD and includes the last beta-coil of the LβH domain and provides the molecular basis for ACP association. This contrasts with a previous study that suggested the UBD domain as the likely ACP docking site due to its proximity to the catalytic cleft and the presence of an electropositive patch (111), and correlates with a study that showed acyltransferase activity is abolished when the C-terminal helices of the ARD are removed (110), even though the truncated LpxD retains its trimeric structure (111). It is worth mentioning that although the analogous C-terminal region of the LpxA acyltransferase is found to adopt a completely different orientation from that of LpxD (37, 108), it may serve a similar function in binding ACP.

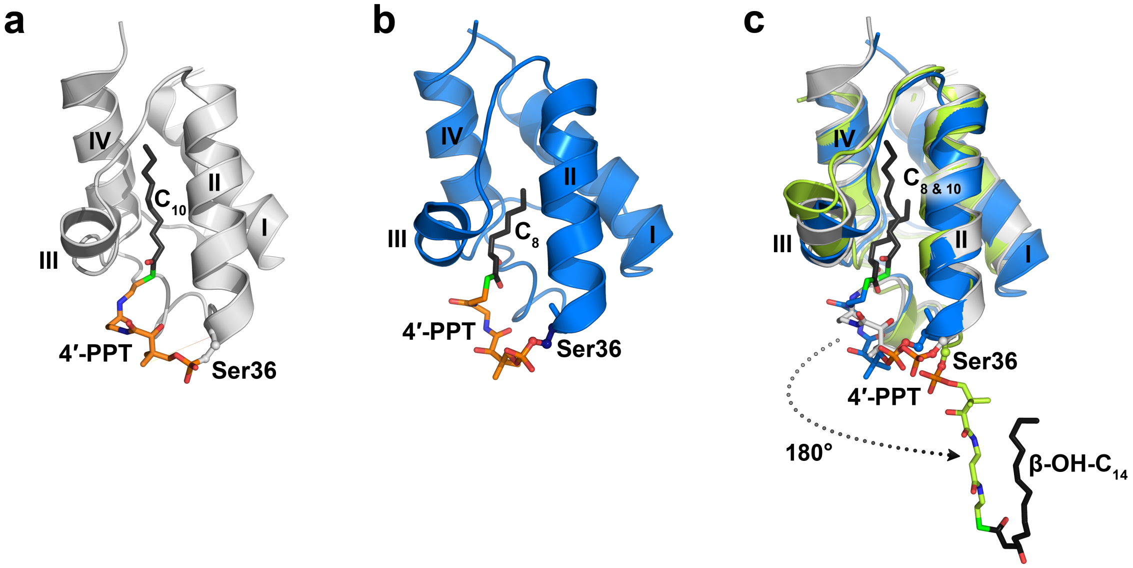

Figure 2.8: Structural comparison of *acyl*-ACPs. The X-ray and NMR structures of **(a)** *E. coli* decanoyl-ACP (PDB 2FAE, light gray) and **(b)** *S. coelicolor* *R*-3-hydroxyoctanoyl-ACP (PDB 2KOQ, blue), respectively, determined in the absence of partner enzyme. The acyl-chains (dark gray) are covalently attached via a thioester bond to the 4′-PPT arm (colored in orange and by atom) and are tucked inside the hydrophobic cavity. **(c)** Superposition of decanoyl- and *R*-3-hydroxyoctanoyl-ACP with the structure of *intact-acyl*-ACP colored green (LpxD is omitted for simplicity). The 4′-PPTs are colored according to ACP affiliation. The 4′-PPT arm of *intact-acyl*-ACP has pivoted about Ser36, rotating by 180° to present the acyl-chain to the active site of LpxD.

2.2.2 The ACP-LpxD interface

By virtue of the LpxD trimer symmetry and the complete engagement of ACP, three competent active sites are created (Fig. 2.9a). However, it remains unclear as to whether all three function independently, simultaneously, or perhaps furnish some type of cooperative allostery. The ACP-LpxD interface buries a surface area of ~530 Å^2 and is predominated by electrostatic interactions. In addition to van der Waals contacts and extensive interactions with the prosthetic group, the large binding footprint explains the 'strong, transient' nature of these two protein partners and correlates with their reported high affinity (110). An overlay of the electrostatic surface shows the complementarity between the ARD and ACP (Fig. 2.9b). A combination of residues located on helix-II, as well as portions of L1, L2, and helix-III of ACP provide the acidic surface that binds a pronounced basic patch on LpxD. This surface feature of ACP can be subdivided into two highly acidic regions, I and II, which include residues Glu30-Met44 and Ala45-Glu60, respectively. The complementary binding surface on LpxD forms a shallow groove between coiled-coils of the ARD into which helix-II packs. It is comprised of residues from all three ARD-helices and a few from β-coil-10, including Pro306 from monomer A, Lys311′, Trp313′, Lys315′, Ala317′, Ala318′, Leu319′, Met321′, Asn322′, Asp325′, Met326′, and Arg329′ from monomer B, and Met292″, Arg293″, Pro294″, Asp324″, Lys328″, Lys331″, and Arg335″ from monomer C (Fig. 2.9c). This interaction orients ACP with respect to the LpxD active site cleft by aligning helix-II parallel to the

ARD helical bundle and positioning the pantetheinylated Ser36 residue toward the catalytic chamber.

Within region I Asp35, Ser36, Leu37, Asp38, Val40, Glu41, and Met44 are important for binding the N-terminal end of the recognition helix to the base of the ARD domain (Fig. 2.9c) and the interactions were notably present in each of the *intact-*, *hydrolysed-*, and *holo-*ACP structures. Most of these residues are located on helix-II with the exception of Asp35, which resides on L1. Region II of ACP interacts with the upper portion of the ARD domain, the details of which differ substantially among the three stalled ACP complexes. Most of the residues within regions I and II are conserved among other type II carrier-proteins (Fig. 2.2b) and have been implicated as key modulators of ACP association with other protein partners, such as cytochrome $P450_{BioI}$, *holo-*ACP synthase, and fatty acid megasynthases (72, 86, 87).

The most universal electrostatic interaction displayed across the *intact-*, *hydrolysed-*, and *holo-*ACP structures is between Arg293 of LpxD and Asp35, Asp38, and Glu41 of ACP that flank Ser36. This electrostatic interaction structurally anchors Ser36 so that ACP is poised to extend its acylated 4′-PPT prosthetic group toward the His239 catalytic base. Moreover, this coordination point is crucial for ACP association as mutation of Arg293 to alanine results in a 23-fold increase in K_M for *acyl-*ACP as compared to wild-type LpxD, with little effect on k_{cat} (110). Although Arg293 clearly plays an important role, it is obvious that a single residue cannot explain the tight association. For example, LpxD acyltransferase activity is abolished when the C-terminal helices are removed (110), which does in fact remain a timer (111). This occurs even though Arg293 remains on β-coil-10. Therefore, Arg293 contributes to ACP binding but is not sufficient without the entire ARD domain. In fact, the *intact-acyl*-ACP complex identified several additional electrostatic interactions between residues located at the top of the ARD and region II of ACP.

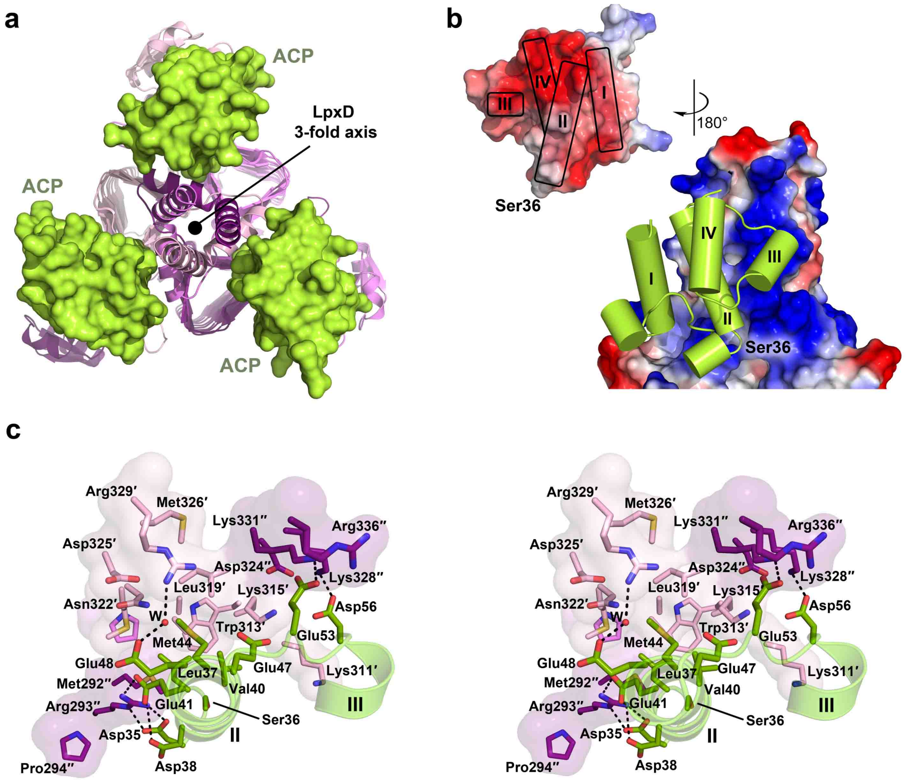

Figure 2.9: Intermolecular interactions between ACP and LpxD. (a, b) Overview of the protein-protein interactions. **(a)** Top-down view of the ACP-LpxD complex showing three molecules of ACP bind per LpxD trimer (*intact-acyl*-ACP depicted and colored as in figure 3.3). **(b)** Electrostatic surface representation of the ARD and ACP (inset), the potential contours were scaled to +79.2 (blue) and -79.2 (red) $k_B T e^{-1}$ (where k_B is the Boltzmann constant, T is temperature and e^{-1} is the charge of an electron;*intact-acyl*-ACP depicted). **(c)** Stereoview of the *intact-acyl*-ACP complex. Only those residues and their molecular surfaces that contribute at the protein-protein interface (chain J) are shown. Salt-bridge interactions are indicated by black dashes. The *acyl*-4′-PPT group attached to Ser36 is omitted for clarity.

2.2.3 Acyl-4′-PPT interactions and LpxD functional surfaces

In addition to the protein–protein interactions, the prosthetic group and acyl-chain of the *intact-acyl*-ACP complex extensively contact the surface of LpxD (Fig. 2.10a and Fig. 2.11a). The *β-OH-C*$_{14}$ acyl-chain packs into a pronounced hydrophobic channel (*N*-channel) formed by residues between adjoining LBH domains, including Ala′250, Gly251′, Gly269′, Gly287′, Met288′, Phe183″, Gln236″, Ala238″, Ile254″, Met255″, Ala256″, Gly257″, Val272″, Ile273″, Asn274″, Met290″, Val291″, and Met292″. The 4′-PPT arm and the acyl-chain adopt a horseshoe-like conformation relative to one another, which in effect buries the acyl-chain between the prosthetic group and residues lining the *N*-channel. The 4′-phosphate moiety of 4′-PPT is coordinated by Asn310 and Arg314 of LpxD. This is in contrast to both the crystal structures of cytochrome P450 and BioH methyl ester esterase that were solved in complex with *acyl*-ACPs. The former structure showed a network of water molecules that mediate interaction with the 4′-phosphate (87), whereas the latter structure displayed no interactions at all (121). Direct contact of the prosthetic group with LpxD may partially explain the strong binding affinity reported for these partners (110) and conceivably may contribute to some level of specificity. The remainder of the 4′-PPT arm adopts a rather extended conformation, stretching over 14 Å, and interacts with residues primarily along the rim of the *N*-channel. The functional groups along one side of the pantetheinyl-arm hydrogen bond with the amide nitrogen atoms of Gly269′ and Gly287′, whereas the opposing side makes

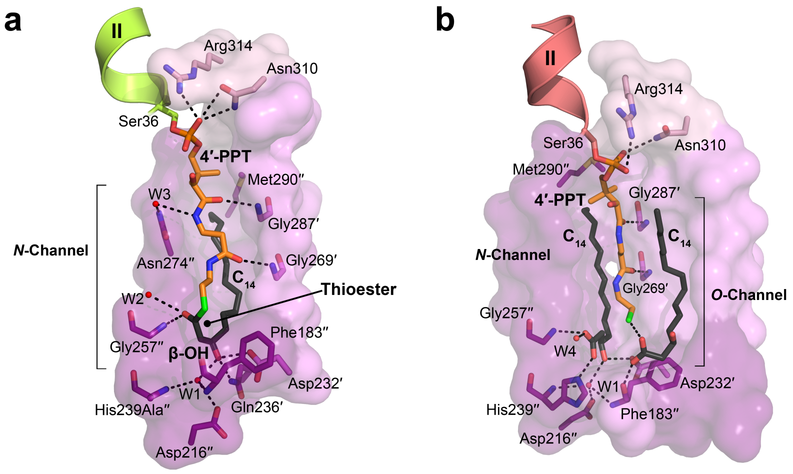

Figure 2.10: Detailed interactions between LpxD reaction chamber and bound acyl-4′-PPT. Molecular surfaces are of only those residues that contribute to interactions and are colored as in figure 2. Hydrogen bonds are shown as black dashes. **(a)** The *intact-acyl*-ACP complex. The attached *β-OH-C*$_{14}$ binds the hydrophobic *N*-channel and its terminal carbon-atoms pack near Met290″. The thioester scissile bond is positioned above His239Ala″ and hydrogen bonds with Gly257″ of the oxyanion hole. The β-hydroxyl group is coordinated through a hydrogen bond network with residues in the catalytic cleft. The 4′-PPT hydrogen bonds with residues lining both sides of the *N*-channel. **(b)** The *hydrolysed-acyl*-ACP complex. The newly formed carboxylate makes hydrogen bonds with His239″ and Gly257″. An equivalent *β-OH-C*$_{14}$ acyl-chain is shown bound to the hydrophobic *O*-channel adjacent to the 4′-PPT. **(c)** The *holo*-ACP complex. The 4′-PPT arm interacts at the far end of the channel, positioning the terminal thiol near Met290″.

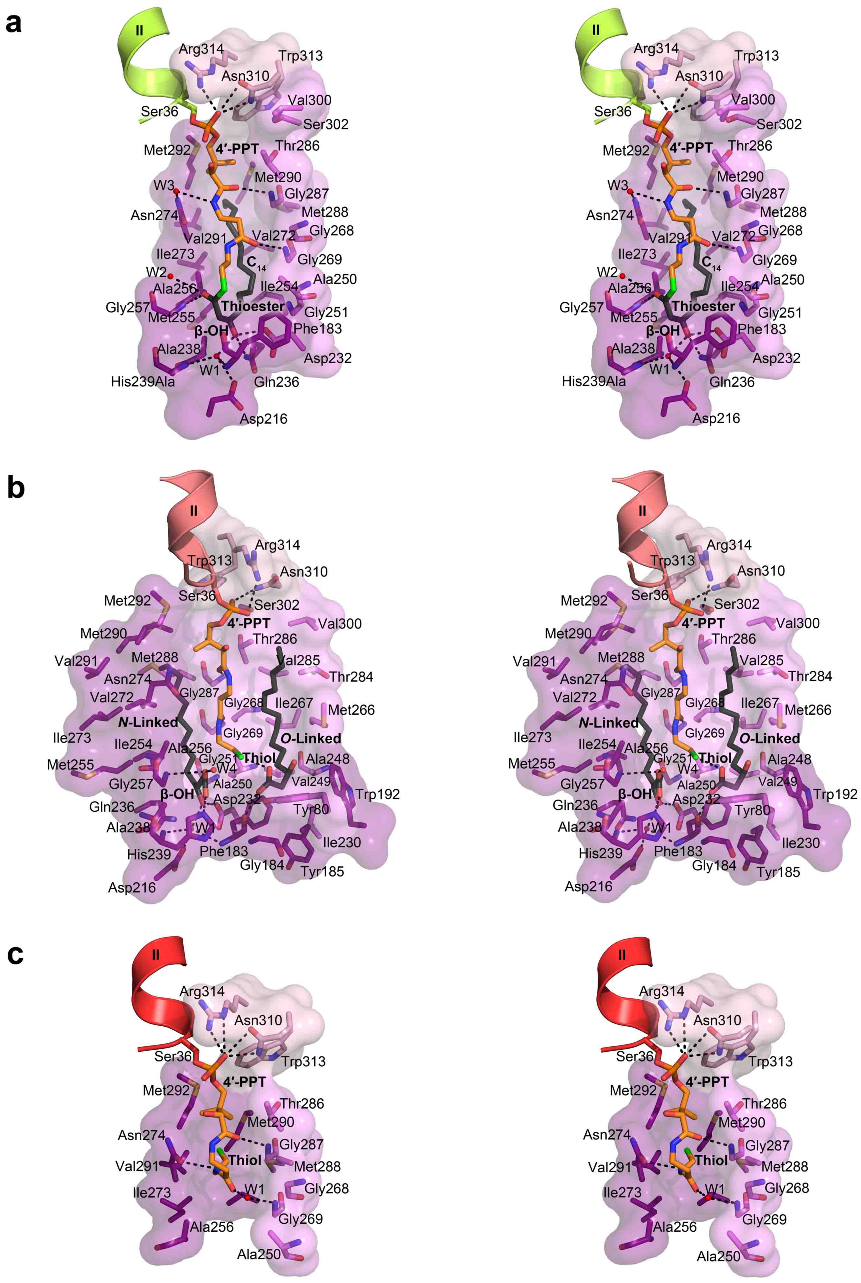
a
II
Arg314
Trp313
Asn310
Val300
Ser36
Ser302
Met292
4′-PPT
Thr286
Met290
W3
Gly287
Met288
Asn274
Gly268
Val291
Val272
Ile273
Gly269
C14
W2
Ala250
Ala256
Ile254
Gly257
Met255
Thioester
Gly251
β-OH
Phe183
Ala238
Asp232
W1
His239Ala
Gln236
Asp216
b
II
Arg314
Trp313
Asn310
Ser36
Met292
Ser302
4′-PPT
Val300
Met290
Thr286
Val291
Met288
Val285
Thr284
Asn274
Val272
Gly287
Gly268
Ile267
Met266
N-Linked
Gly269
Ile273
Ile254
Ala256
O-Linked
Met255
Gly251
Thiol
Ala248
W4
Gly257
Ala250
Val249
Gln236
β-OH
Asp232
Trp192
Ala238
Tyr80
W1
His239
Phe183
Ile230
Gly184
Asp216
Tyr185
c
II
Arg314
Asn310
Ser36
Trp313
4′-PPT
Met292
Thr286
Met290
Asn274
Gly287
Thiol
Val291
Met288
W1
Ile273
Gly268
Ala256
Gly269
Ala250

Figure 2.11: Stereoview of **(a)** *intact-acyl*-ACP, **(b)** *hydrolysed-acyl*-ACP, and **(c)** *holo*-ACP complex structures detailing the interaction of the acyl-4′-PPT moieties within the reaction chamber of LpxD. Only those residues that contribute to ligand contact are shown with transparent molecular surfaces. Hydrogen bonds are shown as black dashes and the color scheme is as in figure 2.10.

a hydrogen bond with the side-chain of Asn274″ mediated by a water molecule. A number of additional residues interact with the 4′-PPT group, the majority of which provide van der Waals contacts (Trp313, Gly268′, Thr286′, Val300′, Phe183′, Ala256″, Asn274″, Met290″, and Met292″). This conformation of 4′-phosphopantetheine places the thioester bond in proximity to the alanine-substituted His239 catalytic base and orients the carbonyl-oxygen of *β-OH-C*$_{14}$ toward the amide nitrogen atom of Gly257″, corroborating its role in forming the oxyanion hole (122).

Two features of LpxD acyl-chain specificity are explained by the *intact-acyl*-ACP structure. First, the terminal two carbon-atoms of *β-OH-C*$_{14}$ pack against Met290″ located at the far end of the *N*-channel. This correlates with the preference of *E. coli* LpxD for acyl-chains that measure 14-carbons long (110) and supports the role of Met290 as a 'hydrocarbon ruler,' which discriminates acyl-chains based on their carbon-length (39). Second, LpxD is specific for the β-hydroxyl group of the acyl-chain; its removal completely abrogates acyltransferase activity (36). Our structures reveal an intricate hydrogen bond network between the β-hydroxyl group and Asp232′, Gln236′, and a critical water-mediated bridge with Asp216″ and the main-chain nitrogen atoms of Phe183″ and His239Ala″. Selectivity for *β-OH-C*$_{14}$ is most likely an amalgamation of these key factors, which together provide proper register of the thioester scissile bond relative to His239 and the GlcN amino-nucleophile. Any adjustment in its carbon-atom measurement or hydroxylation would displace the thioester bond from the active site, resulting in improper geometry for catalysis to occur.

By contrast to the *intact-acyl*-ACP complex, the thioester bond is broken in the *hydrolysed-acyl*-ACP structure. The 4′-PPT and acyl-chain make similar interactions with only minor differences (Fig. 2.10b and Fig. 2.11b). The newly formed carboxylate head group is rotated and makes a hydrogen bond with the Nε2 nitrogen atom of His239″. Also, the terminal thiol of the liberated 4′-PPT arm has shifted slightly by ~1.3 Å. The discovery of a second molecule of *β-OH-C*$_{14}$ fatty acid bound to the LpxD surface revealed the *O*-channel, which likely binds the acyl-chain of the UDP-acyl-GlcN lipid substrate. Lining the hydrophobic cleft are residues Tyr80′, Ile230′, Ala248′, Val249′, Ala250′, Met266′, Ile267′, Gly268′, Thr284′, Val285′, Thr286′, and Val300′, all of which belong to a single LβH monomer. The *O*-channel is solvent exposed and because it is situated adjacent to the 4′-PPT prosthetic group, the ligands generate an 'acyl–PPT–acyl' sandwich. The carboxylate head group of the *β-OH-C*$_{14}$ bound in the *O*-channel forms hydrogen bonds with the main-chain oxygen atom of Phe183″ and the thiol of the 4′-PPT arm. A superposition between our structure and the *C. trachomatis* LpxD determined in complex with UDP-GlcNAc (111) illustrates the proximity of this head group to the anticipated binding locale of the 3-hydroxyl position of the GlcN ring (Fig. 2.12).

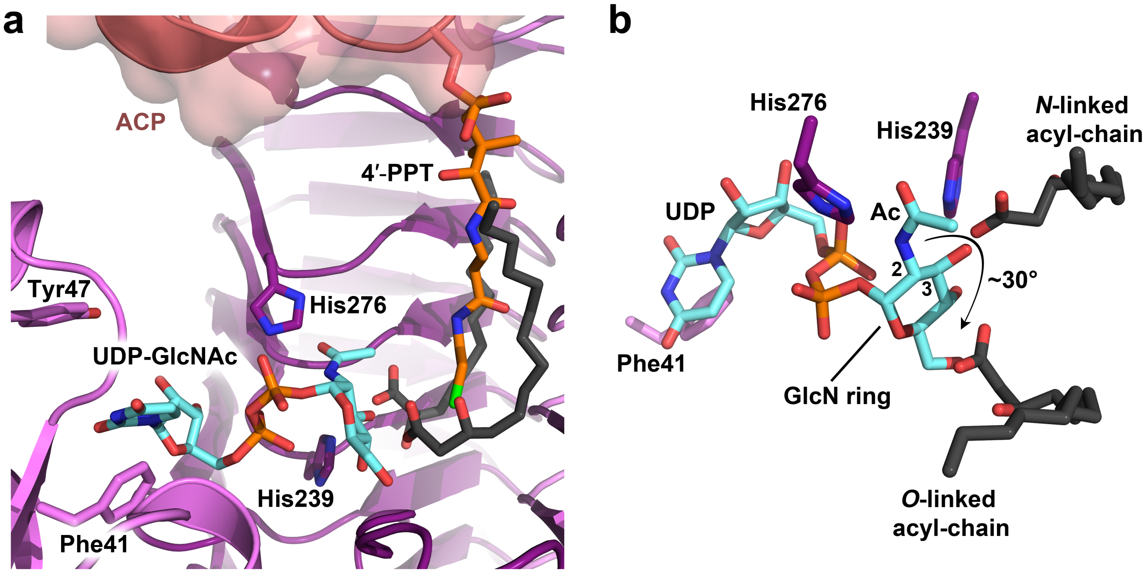

Figure 2.12: Comparison between the *E. coli hydrolysed-acyl*-ACP complex and LpxD from *C. trachomatis* bound to UDP-GlcNAc (PDB 2UIA). (**a**) Close-up view of the binding of UDP-GlcNAc (cyan, colored by atom) in the catalytic cleft of LpxD. The position of the UDP-GlcNAc relative to the nucleotide binding pocket, His239, the acyl-chains within the *N*- and *O*-channels, and the *hydrolysed*-4′-PPT arm is shown. For clarity, the cartoon representation of *Ct*LpxD is not shown. (**b**) Rotated view showing the orientation of the GlcNAc ring. A ~30° clockwise rotation (arrow) is needed for the attachment sites of both acyl-chains to properly align with their respective carboxylate head groups, i.e. the 2- and 3-positions of GlcNAc.

The *holo*-ACP structure revealed an alternate conformation of the prosthetic group (Fig. 2.10c and Fig. 2.11c). Although a short portion of the 4′-PPT including the 4′-phosphate moiety overlays with the *intact*- and *hydrolysed*- structures, the latter half of the pantetheinyl-arm has moved considerably to pack against the far end of the *N*-channel. Because of this dramatic change and the absence of any acyl-substrate, only a subset of residues within the *N*-channel provides surface contacts with the prosthetic group. Notably, the terminal thiols among all modeled prosthetic groups of each *holo*-ACP remain situated near Met290, and we believe that their conserved positioning has functional importance (see below).

2.2.4 ACP-partner communication

What is striking about both the *intact*- and *hydrolysed-acyl*-ACP structures is the conformational similarity between the 4′-PPT prosthetic groups, which completely enclose the reaction chambers (Fig. 2.13a). Although this architecture likely stabilizes substrate binding within the hydrophobic *N*-channel, it raises a key question. Given a sequential ordered reaction mechanism, how does the di-acylated-GlcN product leave LpxD prior to *holo*-ACP if the reaction chamber is completely blocked? A structural comparison between *intact*- and *holo*-ACP sheds light on this matter by exposing a substantial movement that the 4′-PPT arm has undergone (Fig. 2.13b). The 4′-PPT pivots about the seventh-atom position, and consequently, the terminal thiol has vacated the catalytic cleft and moves ~15 Å to be situated near Met290. Notably, the thiol now occupies the same position as was observed for the terminal carbon-atoms of *β-OH-*C_{14}. A sizable region of the reaction chamber closest to the catalytic cleft is now open to solvent, thereby giving the diacyl-GlcN product an opportunity to dissociate prior to the release of *holo*-ACP.

The remarkable difference in conformation displayed by the 4′-PPT arm between the *intact*- and *holo*-ACP structures, together with the ordered sequential mechanism of acyl-transfer, prompted us to propose that this 'swing' motion may in fact be involved in the release of lipid-product. To confirm the role of ACP in this process, we modified LpxD in an attempt to trap the *holo*-ACP product following catalysis. Since every terminal thiol of *holo*-ACP was positioned ~3.7 Å away from Met290 of LpxD, we envisaged the possibility of mutating this residue to a cysteine in an effort to induce a mixed-disulfide linkage. Biochemically, the Met290Cys mutation abrogated acyl-transfer to UDP-acyl-GlcN as compared to wild-type LpxD, although the data do indicate a small, but measurable turnover (Fig. 2.14). This is consistent with what we would expect with forming a covalent bond between the cysteinyl and 4′-PPT thiols.

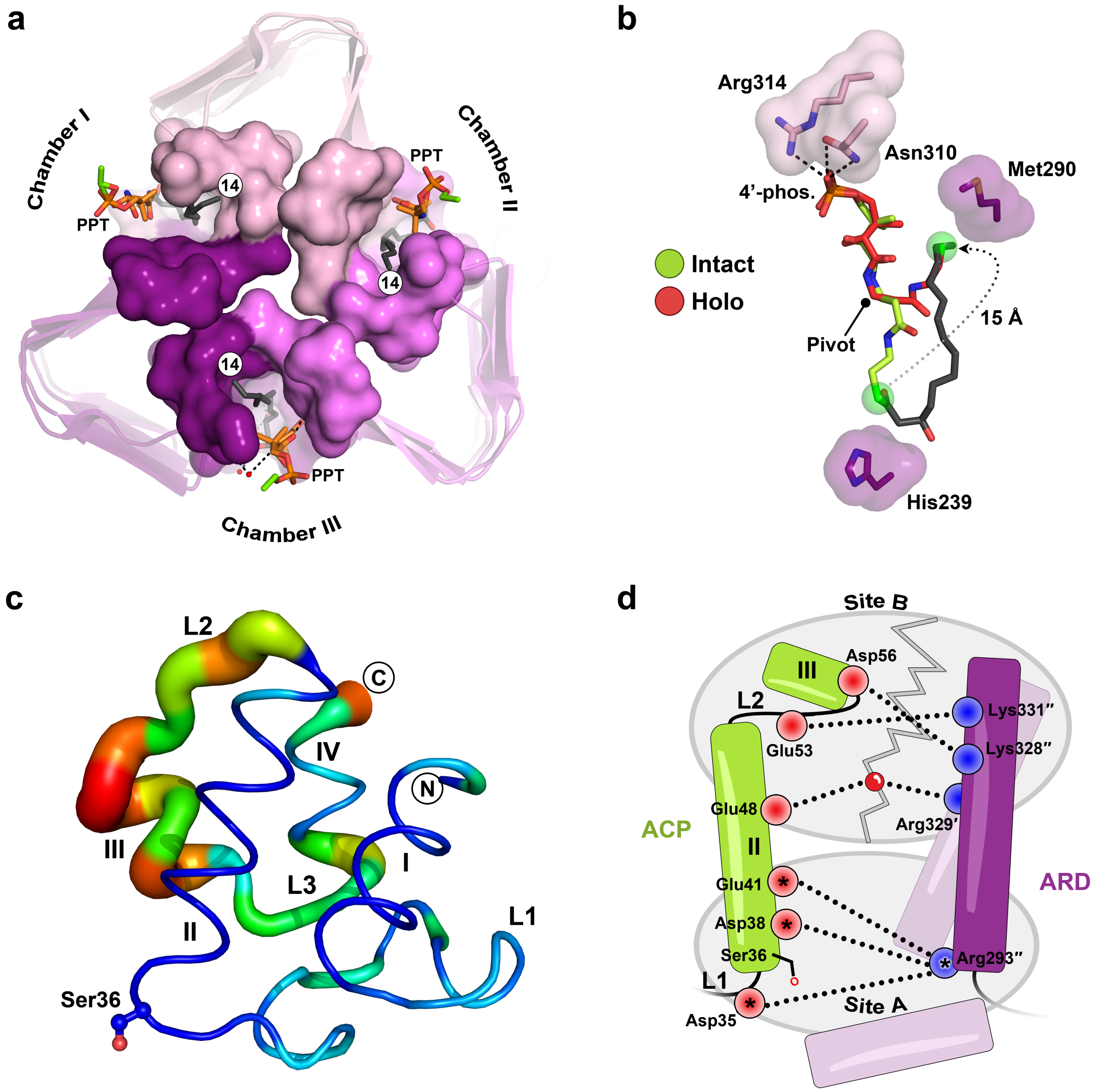
a
Chamber I
Chamber II
Chamber III
PPT
PPT
PPT
14
14
14
b
Arg314
Asn310
Met290
4’-phos.
Intact
Holo
Pivot
15 Å
His239
c
L2
C
IV
N
III
L3
I
II
L1
Ser36
d
Site B
III
Asp56
L2
Lys331″
Glu53
Lys328″
Glu48
Arg329′
ACP
II
Glu41
Asp38
Ser36
L1
Asp35
Site A
Arg293″
ARD

Figure 2.13: ACP conformations and reorganization of its prosthetic group. (**a**) Top-down view of LpxD (*intact-acyl*-ACP depicted) showing three reaction chambers enclosed by the 4′-PPT. Molecular surfaces are of only those residues that contribute to acyl-4′-PPT interactions. (**b**) Structural comparison between the *intact*- (green) and *holo*-4′-PPT (red) prosthetic groups. The 4′-PPT rearrangement is indicated (gray dotted arrow). (**c**) Difference distance matrix calculated between fully modeled *intact*- (chain K) and *holo*-ACP (chain G). Deviations between like atoms are shown as a putty-sausage representation. Both the thickness and heat-map coloring indicate regions of least (thin, blue) to highest (thick, red) displacement. (**d**) Schematic summarizing differences in electrostatic interactions between ACP complexes. Residues are indicated as red (acidic) or blue (basic) circles and subdivided according to region I or II affiliation. Interactions made by *intact-acyl*-ACP alone are depicted (dashed lines) and those common among all complexes are represented with an asterisk. The gray zigzag indicates those electrostatic interactions that are broken in the *hydrolysed*- and *holo*-ACP product complexes.

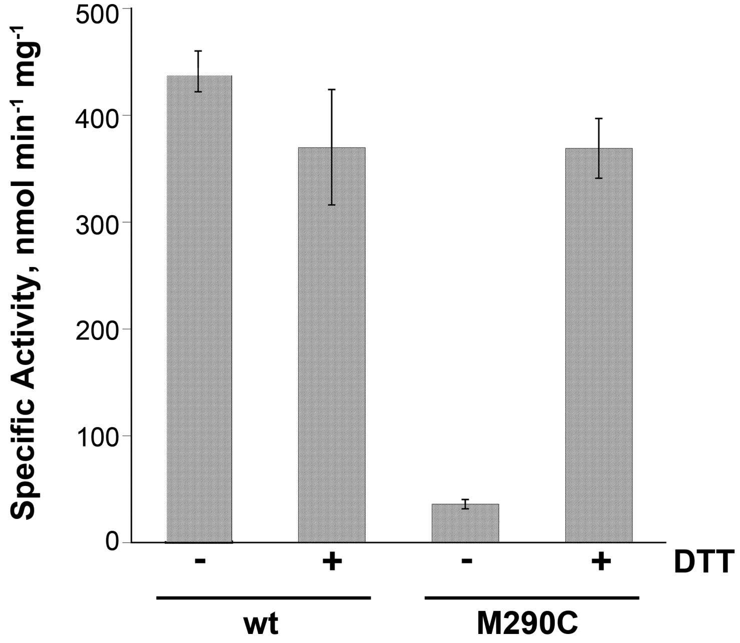

Figure 2.14: Biochemical evidence for the role of ACP in product release. Bar chart showing the effects of DTT on the *in vitro* specific activity of wild-type LpxD (wt) or the Met290Cys (M290C) LpxD mutant. The assay mixture contained 40 mM HEPES (pH 7.4), 0.02 mg/mL BSA, 6 μM *β-OH-C$_{14}$*-ACP, and 4 μM [α-^{32}P]-UDP-acyl-GlcN (0.005-0.04 μCi/μL). The reaction was initiated by the addition of either 1.4 nM wild-type *E. coli* LpxD or 4.2 nM Met290Cys LpxD enzyme. Compared to wild-type enzyme, the cysteine mutation abrogates activity, although the data do indicate a small, but measurable turnover. The addition of reductant to the assay mixture (rescues the Met290Cys mutant, within error, to near wild-type levels of activity assayed in the presence or absence of DTT.

Owing to earlier work that showed mutation of Met290 to alanine retained activity (39), albeit shifting chain-length specificity toward longer acyl-chains, we reasoned that if Met290Cys-LpxD is in fact bound to *holo*-ACP through a mixed-disulfide, then the addition of reducing agent would rescue acyl-transfer. Accordingly, titration of DTT into the reaction mixture recovers activity of Met290Cys-LpxD to levels indistinguishable from that of wild-type enzyme also assayed in the presence of reductant (Fig. 2.14). These data suggest the presence of a post-catalytic mixed-disulfide bond formed between the 4′-PPT and cysteine residue introduced at the far end of the hydrophobic *N*-channel. We postulate that following hydrolysis of the thioester scissile bond, the 4′-PPT thiolate moves from its location near His239 to a position close to the 'hydrocarbon-ruler' in the course of product release. Moreover, as typically shown with 'strong, transient' interactions (117) this substantial movement of the pantetheine arm likely serves as the 'molecular trigger' that promotes the collapse of the ACP-partner complex.

Because our structures show different states of ACP stalled at the LpxD active site, an alignment of LpxD domains between them allows visualization of the movements within ACP as it relates to the overall catalytic cycle (Fig. 2.13c), which to the best of our knowledge is unprecedented. Helix-I, helix-II, and portions of L1 remain relatively unchanged (RMSD of ~1 Å) and are preserved for the purpose of docking with LpxD and allows for the 'swing' motion of the 4′-PPT arm. The largest differences occur downstream of the recognition helix (Fig. 2.13c), including helices-III, -IV, L2 and L3 (RMSD of ~3 Å) and are an indication of what interactions must ultimately break for dissociation. A closer inspection reveals that the *intact*-complex makes electrostatic interactions with the entire ARD interface that involves region II, whereas both the *hydrolysed*- and *holo*-ACP structures completely lack any contact with this region (Fig. 2.13d). For example, Glu48 interacts with Arg329′ through an intervening water molecule and Glu53 and Asp56 form a salt-bridge with Lys331″ and Lys 328″ of LpxD, respectively. The more extensive interactions observed with the *intact*-complex provide molecular recognition that 'zippers' the two protein partners together during association. Moreover, these data indicate that following acyl-transfer, the substantial movement of pantetheinyl group 'triggers' both helix-III and L2 to undergo a conformational change that cause residue interactions within region II to break, ultimately destabilizing the protein–protein complex. In this context, one particular molecule of *holo*-ACP is displaced from the others and possibly represents a different binding state (Fig. 2.15). Consequently, Ser36 and the 4′-phosphate of its pantetheine group have moved by nearly 5 Å in the direction away from LpxD, breaking key interactions with Asn310 and Arg314. Because *holo*-ACP should be leaving LpxD at this point in the sequential ordered reaction, these structural differences reveal additional interactions that must break leading to ACP-partner dissociation.

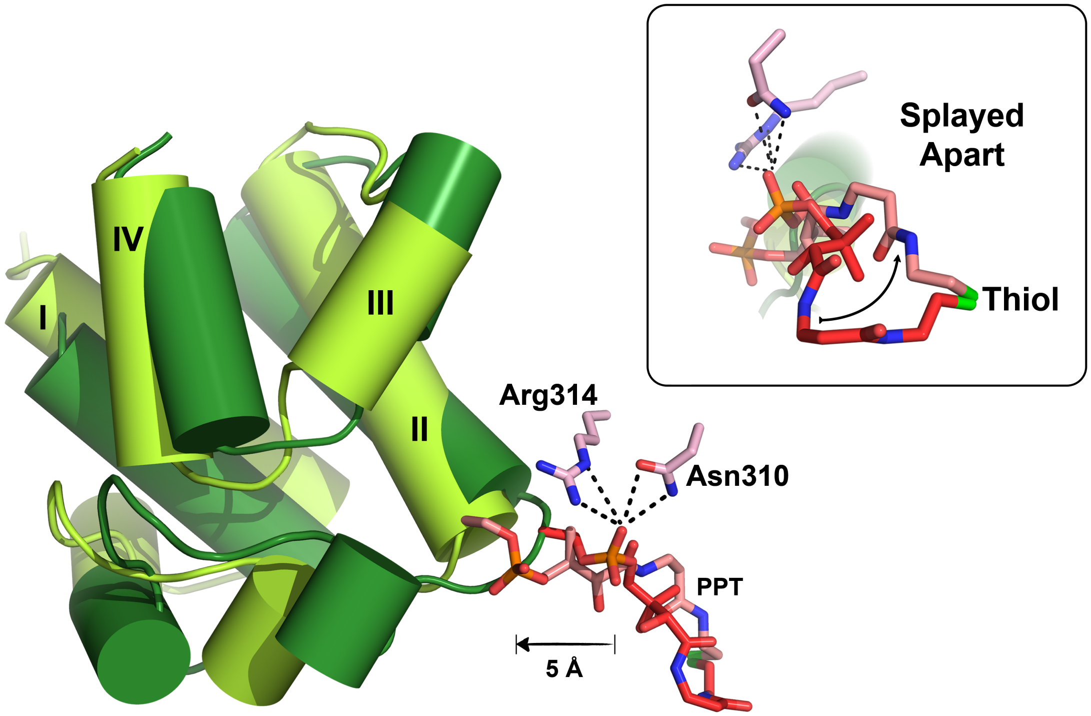

Figure 2.15: Structural differences between molecules of *holo*-ACP. The superimposed *holo*-ACPs are colored light (chain I) or dark green (chain K) and their 4′-PPT groups are colored salmon or red, respectively. All four helices have displaced from one another. The 4′-PPT group (chain I) shifts by ~5 Å and splays apart from chain K (inset, rotated 90°). The terminal thiols remain affixed at the far end of the *N*-channel near Met290, identical to the other molecules of *holo*-ACP.

2.3 Discussion

The crystal structures presented in this chapter represent the first to have captured several stalled complexes of ACP along its acyl-delivery reaction coordinate: *intact-acyl*-ACP, *hydrolysed-acyl*-ACP, and *holo*-ACP. On the basis of these structures, a model is presented for ACP-based synthesis of lipid A precursors catalyzed by LpxD (Fig. 2.16). (i) β-OH-C_{14} acyl-intermediates are shuttled by ACP to LpxD, although the mechanism for extracting the β-OH-C_{14} from within the core of ACP is not known. (ii) *Acyl*-ACP is the first to bind LpxD in the bi-substrate reaction and does so with rather high affinity (110). The extensive interactions at the interface explain the 'strong, transient' nature of these protein partners, which not only involve residues that extend the length of ACP, but also the entire 4′-PPT prosthetic group. The structures presented here have revealed that LpxD is capable of binding three molecules of the carrier-protein at a time, yet it is not clear whether this is required to reach its highest level of activity. The interfacial contacts made by helices-II and –III as well as nearby loop regions of ACP play a major role in docking the carrier-protein securely to the newly identified ARD domain. This properly orients ACP to deliver its acyl-4′-PPT, which adopts an unusual horseshoe-like conformation within the catalytic cleft. Packing of the terminal carbon-atoms and β-hydroxyl substituent provides the correct register of the thioester scissile bond relative to His239. The 4′-PPT serves an important role in this process, providing an enclosure for each reaction chamber. (iii) UDP-acyl-GlcN binds next in the ordered sequential reaction with the β*-OH-*C_{14} substituent carried from the lipid substrate packing into the *O*-channel located on one side of the 4′-PPT arm. (iv) Following acyl-transfer the liberated pantetheinyl-arm remains fully extended and sandwiched between both lipid acyl-chains. However, this organization completely occludes any obvious path for the di-acyl-GlcN product to leave prior to *holo*-ACP. We postulate that the substantial rearrangement observed by the *holo*-ACP pantetheinyl-arm is the 'molecular trigger' that initiates the release of lipid product and is followed by the collapse of the protein–protein complex. Relocating the terminal thiol in proximity of Met290 at the far end of the *N*-channel, unblocks the active site chamber enabling the (v) release of UDP-diacyl-GlcN; thus, providing the essential building blocks for synthesis of the Kdo_2-lipid A anchor of LPS. (vi) Finally, the movement of the 4′-PPT initiates conformational changes within helix-III and L2 that destabilize region II of ACP, ultimately breaking interactions within region I that lead to the dissociation of *holo*-ACP.

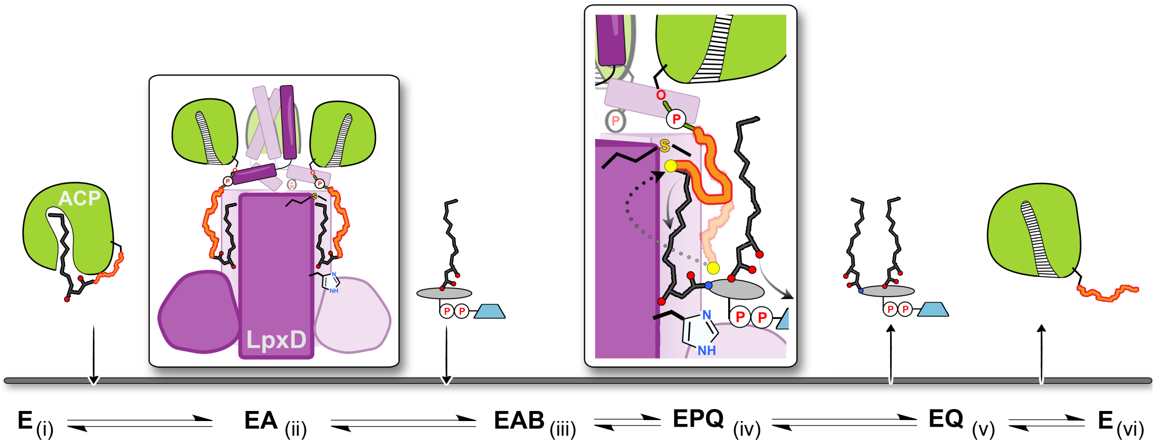

Figure 2.16: Molecular basis for the ordered-sequential reaction mechanism and involvement of ACP in lipid-product release. *Acyl*-ACP binds first (i) to free LpxD forming the (ii) binary complex. ACP associates with the ARD and the acyl-4′-PPT packs into the hydrophobic *N*-channel, thus (iii) enabling UDP-acyl-GlcN to bind next and initiate acyl-transfer. In the ternary product complex (iv) the 4′-PPT arm of *hydrolysed-acyl*-ACP (transparent orange squiggle) completely encloses the reaction chamber, blocking UDP-diacyl-GlcN from leaving. By moving toward Met290 (dotted arrow), the 4′-PPT (dark orange squiggle) drives the (v) eventual release of UDP-diacyl-GlcN by opening up the catalytic chamber. This motion also 'triggers' (vi) conformational changes downstream of helix-II leading to *holo*-ACP dissociation.

The structures captured in this study begin to establish key molecular movements within ACP that initiate molecular recognition and a mechanism with which associations can be ultimately broken. In this context, we can extract some general principles for these types of interactions. First, although there does not yet appear to be a consensus-sequence binding motif on the surface of partner proteins, both regions I and II of ACP seem to be frequently involved, with the majority of the small number of other ACP-based complexes determined revealing that helix-II, -III, L1 and L2 are consistently utilized (86, 87, 121, 123). Second, because these regions are broadly universal, exploiting specific residue contacts at the interface and fine-tuning the buried surface area at these regions likely dictate how ACP-based associations can be both specific and temporary. For instance, our structures reveal the first direct, electrostatic coordination with the 4′-phosphate of both *acyl*- and *holo*-ACP, which in addition to extensive protein–protein contacts provide the ‘strong, transient’ nature of the ACP-LpxD complex. Third, because we observe ACP tied to an entire catalytic cycle, a substantial conformational change downstream of the recognition helix-II may represent a more general communication mechanism for breaking ACP-partner complexes. Finally, the stalled ACPs captured herein have revealed an unprecedented role for carrier-proteins in product release and the contribution of the pantetheinyl group in both the formation and dissociation of the ACP-partner complex. Perhaps motion of the pantetheinyl group in other ACP-based complexes provokes dissociation in a similar manner, especially when considering other ‘strong, transient’ protein partners.

2.4 Methods

2.4.1 Expression and purification of His$_6$-LpxD

E. coli LpxD was over-expressed, and purified as previously reported (110). Briefly, His$_6$-LpxD was expressed in *E. coli* Rosetta/pLysS. The membrane-free fraction was loaded onto a 5 mL Ni-NTA (Qiagen, CA) column and eluted in one step with 200 mM imidazole. The His$_6$-tag was left intact and the resulting LpxD was concentrated to ~4-10 mL and loaded onto a High Load 26/60 Superdex 200 gel filtration column (GE, NJ) equilibrated with 10 mM Tris-HCl (pH 7.5), 500 mM NaCl, and 1 mM DTT. The protein peak had an elution profile consistent with that of the LpxD homotrimer. Fractions were pooled and concentrated to ~40 mg mL^{-1} and stored in aliquots at −80 °C. The wild-type LpxD enzyme utilized in the LpxD assay was purified and stored in the absence of DTT.

2.4.2 Construction, expression and purification of His$_6$-LpxD point mutants

Site-directed mutants designed to alter Met290 (Met290Cys), and His239 (His239Ala) were accomplished using the QuikChange PCR mutagenesis kit (Stratagene, CA). The LpxD variants were recombinantly expressed in C41(DE3) *E. coli* (124) cells and purified in the same manner as described for wild-type His$_6$-LpxD. The His239Ala

LpxD was stored in 10 mM Tris-HCl (pH 7.5), 500 mM NaCl, and 1 mM TCEP, and Met290Cys LpxD was purified and stored in the absence of a reductant.

2.4.3 LpxD lipid substrate preparation

LpxD radioactive substrate [α-^{32}P]-UDP-3-acylGlcN was synthesized according to established methods with minor modifications (36). Briefly, a typical 62.5 μL reaction mixture containing 25 μl of [α-^{32}P]-UTP (800 Ci mmol^{-1}, PerkinElmer, MA), 0.5 mM glucosamine-1-phosphate, 1 mM $MgCl_2$, 5 mM DTT, 100 mM Tris-HCl (pH 8.0), 12.5 units of inorganic pyrophosphatase, and 3.13 units of UDP-glucose pyrophosphatase was incubated at room temperature for 1 hour to generate [α-^{32}P]-UDP-GlcN. The *N*-acetylation of the product was initiated by adding 63 μL H_2O, 75 μL methanol, 5 μL saturated sodium bicarbonate, and 2.0 μL acetic anhydride to the mixture. 20 minutes later, H_2O was added to the mixture to adjust the volume to 1.75 ml. Subsequently, the reaction was loaded onto a 1 ml DEAE-Sepharose column equilibrated with 10 mM triethylammonium bicarbonate (TEAB, pH 8.5). After washing the column with 10 ml of H_2O, [α-^{32}P]-UDP-GlcNAc was eluted in 1 ml fractions by applying 8 ml of 100 mM TEAB (pH 8.5) to the column. The relevant eluted fractions were dried under a vacuum in a Speed-Vac centrifuge and redissolved in 250 μL H_2O.

In order to synthesize high specific radioactivity [α-^{32}P]-UDP-3-acyl-GlcN, 0.1 μM [α-^{32}P]-UDP-GlcNAc (100 μCi mL^{-1}) and 1.3 μM β-*OH-C$_{14}$*-ACP were reacted for 15 minutes at 30 ˚C in a mixture that contained 40 mM HEPES (pH 8.0), 1 mg mL^{-1} bovine serum albumin (BSA), 0.03 mg mL^{-1} purified *E. coli* His$_6$-LpxA, and 100 μg mL^{-1} purified *E. coli* LpxC. The low specific radioactivity substrate was synthesized in a similar manner by mixing 100 μM [α-^{32}P]-UDP-GlcNAc (2 μCi mL^{-1}) with 50 μM β-*OH-C$_{14}$*-ACP for 30 minutes.

Using a combination of DEAE-Sepharose and C$_{18}$ Sep-Pak columns the [α-^{32}P]-UDP-3-acyl-GlcN substrate was isolated. The DEAE-Sepharose column was pre-washed serially with 5 mL of 1 M Bis-Tris (pH 6.0), 3 mL of 50 mM Bis-Tris (pH 6.0) supplemented with 1 M NaCl, and 4 ml of 10 mM Bis-Tris (pH 6.0). One C$_{18}$ Sep-Pak column, pre-washed sequentially with 10 mL of acetonitrile and 20 mL of H_2O, was attached to the bottom of the DEAE-Sepharose column. The reaction mixture was diluted to 2 mL with H_2O and loaded onto the columns. After washing both of the columns with 0.2 M NaCl, the Sep-Pak column was detached and washed with 20 mL of H_2O. The [α-^{32}P]-UDP-3-acyl-GlcN substrate was eluted from the Sep-Pak column in 0.5 mL fractions with 5 mL of 50% acetonitrile. The fractions containing the lipid substrate were lyophilized, redissolved in 150 μL Bis-Tris (pH 6.0), and stored in aliquots at –20 ˚C.

Using a liquid scintillation counter the concentration of the low specific radioactivity substrate, [α-^{32}P]-UDP-3-acyl-GlcN, was measured by comparing its specific radioactivity to that of the starting material, [α-^{32}P]-UDP-GlcNAc.

2.4.4 *In vitro* assay of LpxD

The LpxD catalyzed conversion of [α-^{32}P]-UDP-3-acylGlcN to [α-^{32}P]-UDP-2,3-diacylGlcN was monitored by thin layer chromatography (TLC) as previously reported (36). The 20 μL assay mixture containing 40 mM HEPES (pH 7.4), 0.02 mg mL^{-1} BSA, 1.4 nM pure wild-type *E. coli* LpxD (or 4.2 nM Met290Cys LpxD), 6 μM *β-OH-C*$_{14}$-ACP, and 4 μM [α-^{32}P]-UDP-3-acyl-GlcN (0.005-0.04 μCi/μL) was equilibrated at 30 °C, and the reaction was initiated by the addition of the enzyme. DTT (100 mM) was added to assess its effect on the catalysis of the wild-type and the mutant LpxD. 1 μL of the reaction mixture was spotted onto a silica gel 60 plate (EMD Chemicals, Germany) at various time-points. After drying under a cold air stream, plates were developed with a chloroform/methanol/water/acetic acid solvent (25:15:4:2, v:v:v:v). The plates were dried and exposed overnight to a Molecular Dynamics PhosphorImager Screen. The conversion rate of the lipid substrate to product was measured using ImageQuant software.

2.4.5 Expression and purification of *holo*-ACP

The *acp* gene was amplified from *E. coli* W3110A genomic DNA using the ACP-forward and ACP-reverse primers (Table 2.2) engineered to introduce downstream of the ACP coding region a spacer sequence, a ribosome binding site, followed by a translation spacer element (denoted PCR product A). The ACPS-forward and ACPS-reverse primers (Table 2.2) were used to amplify *acps* gene from W3110A genomic DNA, which contained a spacer sequence, a ribosome binding site, and a translation spacer element upstream of the ACPS coding region (denoted PCR product B). The ACP-forward and ACPS-reverse primers were subsequently used to generate PCR product C, which contained *acp* and *acps* genes separated by the spacer sequence, ribosome binding site, and the translation spacer element. PCR product C was cloned into a pET16b* vector, which contained an engineered tobacco etch virus (TEV) protease cleavage site instead of Factor Xa, using the *NdeI* and *XhoI* restriction sites. *E. coli* DH5*α* competent cells (Invitrogen, CA) were subsequently transformed with plasmid and transformants were selected at 37 ˚C on a LB-agar plate supplemented with 100 μg mL^{-1} ampicillin. The sequence of the plasmid encoding the N-terminally histidine-tagged ACP and non-tagged ACPS (pET16b*-AM) was confirmed by DNA sequencing.

ACP and ACPS were co-expressed using the pET16b*-AM vector in C41(DE3) *E. coli* cells (124) and cultured at 37 ˚C in 1 L of LB broth supplemented with 100 μg mL^{-1} ampicillin. Upon reaching an OD_{600} of 0.6 the expression was induced for 6 hours with 1 mM isopropyl-β-D-thiogalactopyranoside (IPTG) at 30 ˚C. All the subsequent procedures were carried out at 4 ˚C. The cells were harvested, washed, resuspended and lysed in 20 mM HEPES, pH 8.0 containing 10% glycerol, 200 mM NaCl, and 2 mM DTT (Buffer A), supplemented with 20 mM imidazole. After removal of cell debris by centrifugation at 100,000 x g for 1 hour, the soluble fraction was loaded onto a Ni-NTA (Qiagen, CA) column equilibrated with Buffer A and 20 mM imidazole. The Ni-NTA column was washed with 10 column-volumes and His_{10}-ACP was eluted in one step by Buffer A supplemented with 250 mM imidazole over the equivalent of 5 column-volumes. Although ACPS was not histidine-tagged, it co-purified with His_{10}-ACP. The elution fraction was allowed to slowly rock with 1 mg of TEV protease and 2 mM EDTA overnight. Subsequently, the protein mixture was dialyzed against 20 mM MES, pH 6.0, and 2 mM DTT overnight. The TEV protease and residual His_{10}-ACP were removed by passing the mixture through a 2 mL Ni-NTA column. The resulting flow-through fraction containing ACP was loaded onto a 5 mL QFF ion exchange column (GE, NJ). ACP eluted separately from ACPS by applying a linear gradient of 20 mM MES, pH 6.0, 0-500 mM NaCl, and 2 mM DTT over 50 column-volumes. The fractions corresponding to ACP were pooled together and dialyzed against 100 mM Tris-HCl, pH 7.1, and 200 mM NaCl (Buffer B) overnight. *Holo*-ACP was separated from residual *apo*-ACP (inactive form) by mixing the ACP sample with 5 mL of Thiopropyl Sepharose 6b resin (Sigma-Aldrich, MO) overnight. *Apo*-ACP, which lacks any free thiol group, did not bind to the resin, whereas, *holo*-ACP covalently attached to the resin via the terminal thiol group of its phosphopantetheine moiety. After washing the Thiopropyl Sepharose 6b with 25 mL of Buffer B, *holo*-ACP was eluted in 25 mL of Buffer B supplemented with 25 mM DTT. The complete removal of *apo*-ACP was confirmed by electrospray ionization mass spectrometry. The elution fraction was concentrated to ~4-10 mL and loaded on a High Load 26/60 Superdex 200 gel filtration column equilibrated with 10 mM Tris-HCl, pH7.5, 200 mM NaCl, and 2 mM DTT. The relevant eluted fractions were concentrated to ~20 mg mL^{-1} and stored in aliquots at −80 ˚C.

Table 2.2: Summary of primer sequences used in molecular cloning.

Name	Sequences
ACP Forward	5′-GCGCGCGCCAT**ATGAGCACTATCGAAGAACGC**-3′
ACP Reverse	5′-TTTAAATTCTCCTTCCCGGGCCCGG**TCACGCCTGGTGGCCGTT**-3′
ACPS Forward	5′-CCGGGCCCGGGAAGGAGAATTTAAA**ATGGCAATCTTAGGTTTAGGC**-3′
ACPS Reverse	5′-GCGCGCGCCTCGAG**TCAACTTTCAATAATTACCGT**-3′

The underlined letters indicate the restriction sites for *NdeI* and *XhoI* endonucleases. The bold letters indicate the sequence of the template gene. The green and blue letters show the sequence of the translation spacer element and ribosome binding site, respectively. Orange letters represent the spacer sequence.

2.4.6 Production of *β-OH-C$_{14}$*-ACP

Holo-ACP was charged enzymatically with *R*-3-hydroxymyristic acid (Santa Cruz Biotechnology, Inc.) by soluble *acyl*-ACP synthetase from *Vibrio harveyi* (125). The soluble *acyl*-ACP synthetase (*aasS*) gene was synthesized by GenScript. The *aasS* gene was subcloned into pET-16b expression vector, overexpressed, and the His$_6$-AasS was purified using nickel affinity chromatography as reported by Jiang *et al*. (125). To generate *β-OH-C$_{14}$*-ACP, 0.1 mM of *holo*-ACP was mixed with 0.001 mM AasS and 0.3

mM of the fatty acid (*β-OH-*C_{14}) at room temperature for 3 hours in a buffer containing 100 mM Tris-HCl, pH 7.8, 10 mM ATP, and 10 mM $MgCl_2$. To separate *acyl*-ACP from AasS, the reaction mixture was loaded onto a High Load 26/60 Superdex 200 gel filtration column equilibrated with 10 mM Tris-HCl, pH7.5, and 200 mM NaCl. The complete conversion of *holo*-ACP to *β-OH-*C_{14}-ACP was confirmed by both electrospray ionization mass spectrometry and 2.5 M urea (19%) polyacrylamide (pH 9.5) gel electrophoresis (126).

2.4.7 Crystallization and structure determination

Prior to crystallization, either *acyl*-ACP or *holo*-ACP was mixed with the wild-type or the catalytically inactive His239Ala LpxD in order to preform the protein–protein complex. Initial crystallization hits were identified by screening each protein complex against the Protein Complex Suite (Qiagen, CA) using the sitting-drop vapor diffusion method. Crystals of *holo*-ACP-LpxD were grown at 15 ˚C by mixing the protein solution with the precipitant (0.1 M MES pH 6.0, 0.2 M lithium sulfate, 20% PEG 4000) in ratios of 1:1 and 1:1.5. Crystals achieved full size in approximately 45 days. The crystals were transferred to a cryo-solution using a 50:50 ratio of paratone to mineral oil and immediately cryo-cooled to −180 ˚C in liquid nitrogen. *Hydrolysed-acyl*-ACP-LpxD crystals were obtained by equilibrating the protein mixture against a well solution containing 0.1 M MES pH 6.5, 0.2 M ammonium sulfate, 20% PEG 8000 and incubating at 15 °C. The crystals were harvested on day 10 and cryo-cooled using a solution containing ammonium sulfate, 33% PEG 8000, 5 mM Tris-HCl pH 7.5, 190 mM NaCl, and 20% of the cryoprotectant ethylene glycol. In order to trap the *intact-acyl*-ACP-LpxD complex the His239Ala-LpxD mutant was purified in the presence of the reducing agent TCEP instead of DTT in an attempt to reduce hydrolysis of the thioester bond. His239Ala-LpxD and *acyl*-ACP were premixed using a 1:1 molar ratio prior to crystallization trials. The well solution and the cryoprotectant were the same as that described for the *hydrolysed-acyl*-ACP structure, however, a ratio of 1.5:1 of protein to well solution was required.

The diffraction data were collected on the SER-CAT 22-BM and 22-ID beamlines at the Advanced Photon Source (APS) at Argonne National Laboratory. Data were processed using the HKL2000 (127) software suite (Table 2.1). Although the data for both *intact*- and *holo*-ACP complexes were processed to 2.1 and 2.13 Å, respectively, the *hydrolysed-acyl*-ACP complex was trimmed to 2.9 Å due to the data completeness being unsatisfactory in higher resolution bins, i.e. well below 70%. This resulted in a higher signal to noise ratio in the 2.9 Å resolution bin as well as a much lower Rmerge value. Even though 360 degrees of data were collected, the most likely cause for this phenomenon is the combination of an unfortunate crystal mount orientation with respect to the incident X-ray beam, the quality/hardiness of the crystal, and the fact that the complex crystallized in the *P*1, triclinic space group. The structures were solved by the molecular replacement method using the program PHASER within the PHENIX software suite (128, 129) and the previously determined *E. coli* LpxD structure (PDB code: 3EH0) as the search model. Two trimers of LpxD were observed in the triclinic unit cell for the *intact-acyl*-ACP, *hydrolysed-acyl*-ACP, and *holo*-ACP co-crystal structures. In each case, however, ACP was intentionally omitted during the molecular replacement process, and instead was manually rebuilt into unbiased, contiguous $F_o - F_c$ difference electron density by first rigid-fitting the *E. coli apo*-ACP coordinates (PDB code: 1T8K) (130) into the resulting maps. The models were rebuilt using COOT (131) and iterative structure refinement with restrained and TLS options was carried out using PHENIX (128). For the lower resolution *hydrolysed-acyl*-ACP structure hydrogens were included for refinement with automated optimization of X-ray/stereochemistry and ADP weights selected. Additionally, we utilized the high resolution *E. coli apo*-ACP structure (PDB code: 1T8K) as a reference model. The molecular coordinates and restraints of the 4′-PPT, *β-OH-*C_{14}-4′-PPT, and free *β-OH-*C_{14} fatty acid ligands were generated by using either the Dundee PRODRG2 Server (132) or PHENIX Elbow (128). Composite omit map and simulated annealing omit map calculations were conducted using CNS (133). The protein-ligand interactions were identified by AREAIMOL calculations within the CCP4 suite (134). The quality of the final models was validated using MOLPROBITY (135). The data statistics are reported in Table 2.1. Molecular figures were generated using PyMOL (136).

A total of six ACP molecules were present in the *intact-acyl*-ACP structure (Fig. 2.4). Both the *hydrolysed*- and *holo*-ACP structures exhibited partially bound states of ACP within two or three LpxD active sites as interpreted by the lack of contiguous electron density for the majority of the ACP backbone. As a result, only a portion of ACP that includes Ser36 and its 4′-PPT prosthetic group were included in the final model: (i) *hydrolysed-acyl*-ACP, residues 35-44 of chain L, residues 6-15, 27-53, and 62-73 of chain I, residues 1-15 and 27-73 of chain G, (ii) *holo*-ACP, residues 35-44 of chain H and chain L. The remaining LpxD active sites in the *hydrolysed*- and *holo*-ACP structures contain fully modeled ACPs. In all three co-crystal structures, the electron density maps indicated that the N-terminal methionine of ACP was present and forms a key lattice contact with neighboring molecules of LpxD. Two additional residues (Ser-His) in the *holo*-ACP structure that remain from the TEV cleavage site could also be modeled.

The observed electron density for fully modeled *intact*-, *hydrolysed*-, and *holo*-ACPs were weaker in some regions especially on the backside of the molecule that faces solvent. This implicates conformational heterogeneity throughout the lattice. Nonetheless, in all three co-crystal structures electron density was apparent in every active site for all atoms of the 4′-PPT group. In both the *intact*- and *hydrolysed*-forms, pronounced electron density was also present for the *β-OH-*C_{14} acyl-chains located in the *N*-channel. In addition, electron density indicated that the *hydrolysed-acyl*-ACP complex included two additional molecules of *β-OH-*C_{14} fatty acid bound to the hydrophobic *O*-

channel, although the density was weaker toward the terminal carbon-atoms of the acyl-chains. To investigate the origin of this second fatty acid, we mixed *acyl*-ACP (12.86 mg mL^{-1}) in a 1:2.25 v:v ratio with wild-type LpxD (26.38 mg mL^{-1}) pre-incubated with 1 mM DTT in a solution that was consistent with the condition used for crystallization. The protein solution was incubated at 15 ˚C, and aliquots were taken at different time points and stored at –80 ˚C. Samples were run on a 2.5 M urea (19%) polyacrylamide (pH 9.5) gel (126), which revealed that both DTT (a known phenomenon (137)) and LpxD enhance the cleavage of the thioester bond of *acyl*-ACP (Fig. 2.7). This observation most likely explains why free β-OH-C_{14} fatty acid was available to bind the *O*-channel of LpxD.

Chapter 3. Crystal Structure of *O*-acyltransferase of Lipid A Biosynthesis Bound to Acyl-Carrier-Protein

3.1 Introduction

The characteristic outer membrane of Gram-negative bacteria is an asymmetric bilayer composed of phospholipids and lipopolysaccharides (LPS) that shield bacteria from noxious compounds (e.g. antibiotic and detergents) (138). The oligosaccharide portion of LPS is anchored into the outer membrane by an essential hexa-acylated glucosamine-based saccharolipid known as lipid A (endotoxin) (5, 138). During infection, lipid A stimulates the mammalian host innate immune system by binding to the toll-like receptor 4/ myeloid differentiation-2 complex (114, 139). Although this event is desirable for clearing infection, overproduction of pro-inflammatory cytokines can lead to septic shock and be lethal (5). Lipid A is required for viability and pathogenesis of Gram-negatives (140, 141) and thus its biosynthesis (Raetz pathway) is an attractive antibacterial drug target.

In *Escherichia coli* nine highly conserved enzymes assemble lipid A that is decorated with two molecules of Kdo sugars (3-deoxy-d-*manno*-oct-2-ulosonic acid) (Fig. 1.5) (5). LpxA is the first enzyme in the assembly line and a validated antibacterial target (109). It catalyzes the transfer of the *R*-3-hydroxymyristoyl to the 3-hydroxyl group of UDP-GlcNAc to generate UDP-3-*O*-(*R*-3-hydroxymyristoyl)-GlcNAc (62). LpxA follows an ordered sequential reaction mechanism, however, the binding order is yet to be determined (99). The acylation reaction is thermodynamically unfavorable (K_{eq} = 0.01) (34), and thus the deacetylation reaction of the LpxA product by LpxC is the committed step of the pathway (142, 143).

The acyltransferases of lipid A biosynthesis (LpxA, –D, –L, and –M) rely on type II acyl-carrier-protein for acyl-chain delivery, suggesting a crucial role of ACP in acyl-substrate recognition (5). Type II *acyl*-ACP diffuses freely in the cytoplasmic matrix, all the while protecting the acyl-cargo that is thioester linked to its 4′-phosphopantetheine group (4′-PPT) within an interior hydrophobic pocket (Fig. 1.11) (50, 58). Upon interaction with partner proteins, ACP must undergo a conformational change to extract and present its cargo to the active site of its partners (50, 56). The carrier-protein interacts with numerous enzymes of the primary and secondary metabolic pathways, however due to the transient nature of ACP interactions and conformational mobility of many ACP domains, the structural information about ACP–protein interaction is very limited.

LpxA is the founding member of a large family of enzymes that adopt a left-handed parallel beta-helix fold (37), and provides an excellent system to study protein:lipid and protein:protein interactions. Previous crystallographic studies of LpxA bound to UDP-GlcNAc (100), and UDP-acyl-GlcNAc (104) revealed key active site residues and the lipid binding pocket, yet failed to identify the binding site of ACP. Our recent success in crystalizing LpxD *N*-acyltransferase bound to ACP at different stages of catalysis (144) prompted us to determine the structure of LpxA in complex with the carrier-protein.

We herein present the 2.1 Å crystal structure of *E. coli* LpxA *O*-acyltransferase in complex with its liberated ACP product (*holo*-ACP). The complex structure revealed that similar to the LpxD:ACP complex (144), ACP is localized to the C-terminal domain of LpxA. Notably, a different binding mode of ACP was observed. On the basis of the structural differences between the two acyltransferases, we hypothesize that the C-terminal domain of LpxA forces ACP to bind differently, and also dictates LpxA specificity for ester-linkage acylation of lipid A precursors as opposed to amide-linkage.

3.2 Results

3.2.1 Overview of the LpxA-ACP complex

To visualize how LpxA recognizes the acyl-carrier-protein, we crystallized the acyltransferase in the presence of a 3-fold molar excess *holo*-ACP, and resolved the co-crystal structure to 2.1 Å resolution (Table 3.1). The structure crystalized in the *H*3 space group and contained one LpxA monomer bound to a single molecule of *holo*-ACP in the asymmetric unit. The biological functional unit of LpxA (37), is generated via crystallographic symmetry operations, forming the homotrimeric structure. Each monomer is related to its adjacent monomer by a 120° rotation around the trimeric axis of symmetry (Fig. 3.1a).

Similar to other known NMR and crystal structures, ACP adopts a four-helix bundle architecture with various loops (L1-L3) that connect the helices (69, 118-120). Three major helices (helix-I: residues 2-15, helix-II: residues 36-50, and helix-IV: residues 65-75) run approximately parallel to each other, forming a hydrophobic scaffold capped by a short helix (helix-III: residues 56-61), which is almost perpendicular to the axes of the other helices (Fig. 3.1a). The role of this hydrophobic pocket is to protect the acyl-chain and the reactive thioester bond located at the end of the phosphopantetheine from hydrolysis (Fig. 1.11). The electron density is weaker in some regions of ACP, particularly at Asp35, and Glu47-Glu53 which flank helix-II (Fig. 3.2). Accordingly, the B-values of these residues are relatively higher than the rest of ACP suggesting conformational mobility in these regions (Fig. 3.3). Moreover, only the 4′-phosphate group of the 4′-phosphopantetheine, which is covalently attached to Ser36, was visualized in the structure, as the electron density for the remaining pantetheine moiety was extremely weak. Therefore, the pantetheine arm was not included in the final model. Nonetheless, the positions of the side-chains were clear at the LpxA–ACP binding interface.

Table 3.1: Data collection and refinement statistics.

	LpxA:*Holo*-ACP
Data collection	
Space group	*H*3
Cell dimensions	
a, *b*, *c* (Å)	104.20, 104.20, 82.09
α, β, γ (°)	90.00, 90.00, 120.00
No. of Reflections	112997
No. of Unique Reflections	19460
Resolution (Å)	20.00-2.10
R_{sym} or R_{merge}	0.07 (0.76)
$I / \sigma I$	29.1 (2.4)
Completeness (%)	100.0 (99.9)
Redundancy	5.8 (5.7)
Refinement	
Resolution (Å)	19.77-2.10
No. reflections	19413
$R_{\text{work}} / R_{\text{free}}$	18.8 / 22.4
No. atoms	
LpxA	3927
ACP	580
Water	100
B-factors	
LpxA	43.3
ACP	70.9
Water	50.3
R.m.s. deviations	
Bond lengths (Å)	0.01
Bond angles (º)	0.68
Ramachandran statistics	
Favored (%)	97.3
Disallowed (%)	0.0

Data were collected from a single crystal for each complex.
*Highest resolution shell is shown in parenthesis.

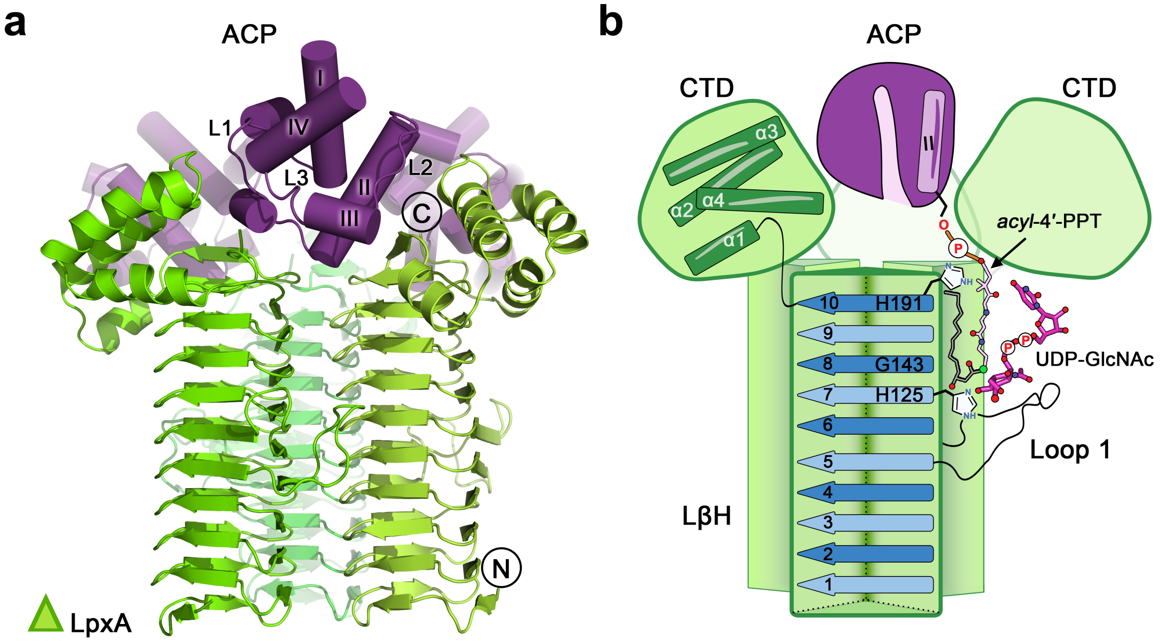

Figure 3.1: ACP bound to LpxA. **(a)** Overall architecture of LpxA:ACP complex. Three *holo*-ACP molecules (purple, cylindrical helices) are bound to the carboxy (C)-terminal helices of LpxA trimer (each monomer is colored by a different shade of green). The amino (N)- terminal end of LpxA is composed mostly of beta strands. **(b)** Cartoon representation of the LpxA ternary complex with *acyl*-ACP, and UDP-GlcNAc. Each monomer of LpxA consists of a left-handed β-helix (LβH), and a C-terminal domain (CTD). LβH and CTD are composed of ten equilateral β-triangles (blue strands), and four α-helices (green). UDP-GlcNAc, ACP and its *acyl*-4′-PPT group are shown. The position of the catalytic base (His125), the oxyanion hole (Gly143), and the hydrocarbon ruler (His191) are indicated within LβH.

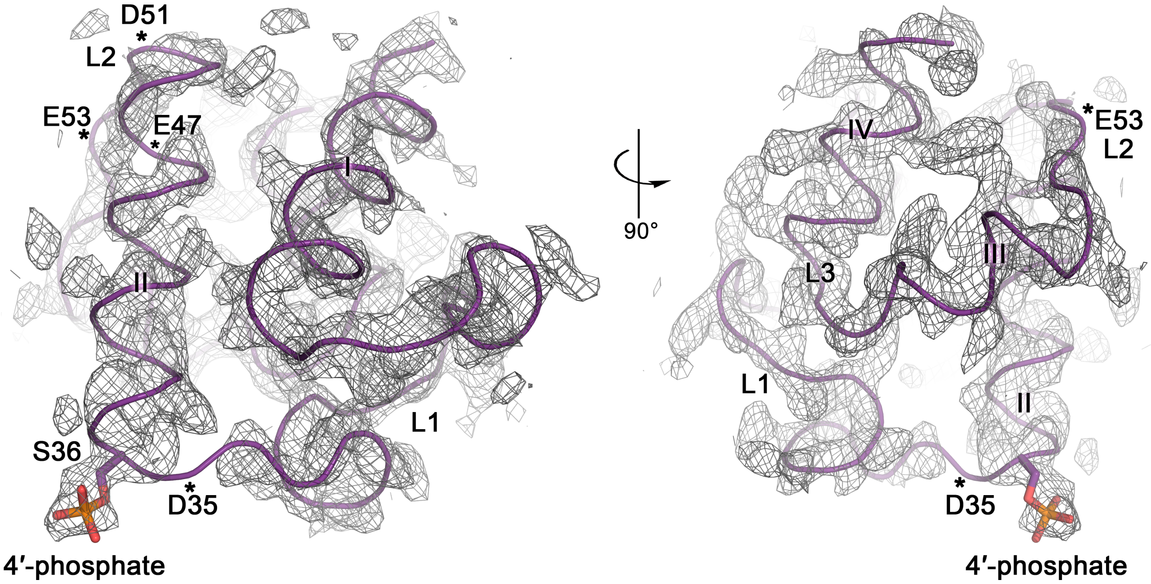

Figure 3.2: The electron density map of *holo*-ACP. $2F_o - F_c$ composite omit electron density covering each α-carbon trace. The map is contoured at 1.5 σ and colored in gray. The asterisk symbol indicates the location of residues with poor electron density.

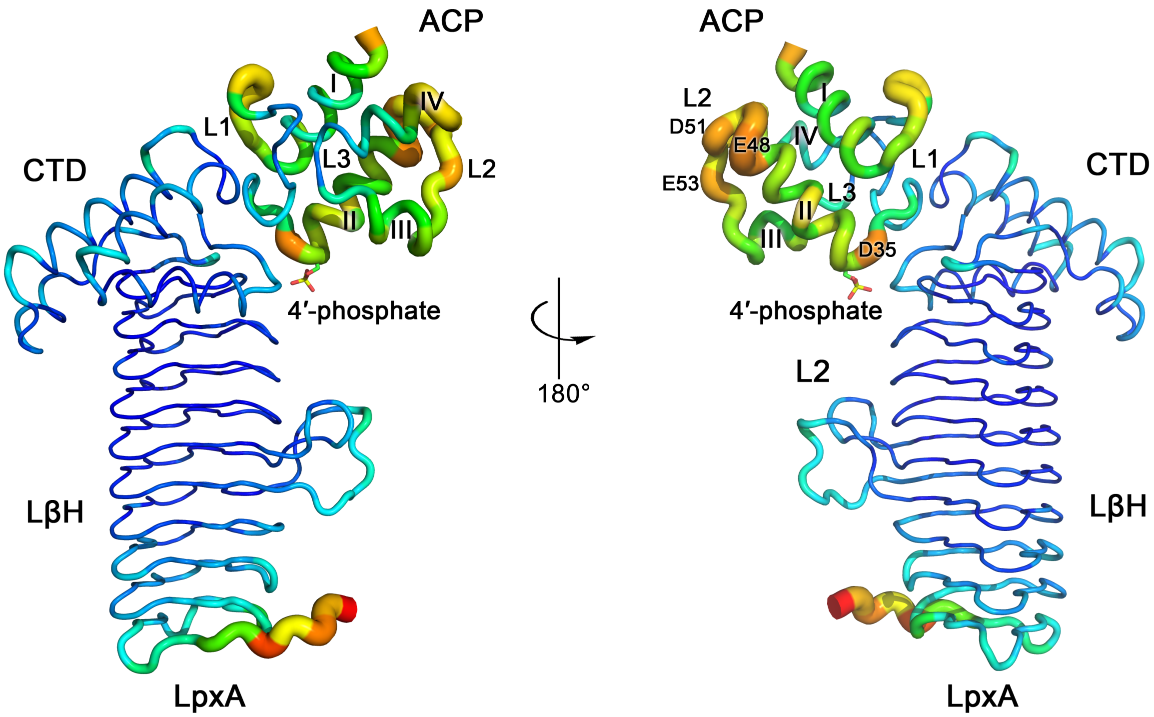

Figure 3.3: Overview of temperature factor distribution of LpxA:*holo*-ACP. Side view of the LpxA:*holo*-ACP complex. A single monomer of LpxA and ACP are represented as ribbon-putty cartoon and colored according to main-chain B value. The thickness and heat-map coloring indicates the regions with least (thin, blue) to highest (thick, red) temperature factor. The subdomains of LpxA and ACP as well as the location of the 4′-phosphate group are indicated.

As depicted in FIGURE 3.1B, each monomer of LpxA is composed of two domains: an N-terminal domain, which adopts an unusual left-handed parallel β-helix fold (LβH, residues 1-186) that extends approximately 50 Å in length, and a globular α-helical C-terminal domain (CTD, residue 187-262). The LβH is composed of ten equilateral triangles that are characterized by three hexapeptide segments with the consensus sequence of [LIV]-[GAED]-X_2-[STAVE]-X (37). For each 18-residue triangle, 6 hydrophobic side-chains are oriented toward the center, where there is no solvent present, and 12 side-chains are directed outward. LpxA possesses a conserved histidine residue (His125) on triangle #7 that acts as a general base and is stabilized by a negatively charged residue, Asp126. In the ternary complex, His125 activates the lipid A precursor by extracting a proton from the 3-hydroxyl group of UDP-GlcNAc which subsequently undergoes nucleophilic attack on the thioester bond of *acyl*-ACP (99). Forming the oxyanion hole is Gly143 that stabilizes the negative charge associated with forming the tetrahedral transition state (104).

Different LpxA orthologs are selective toward different acyl-chain lengths that are delivered by the carrier-protein. In *E. coli*, LpxA is highly specific for *R*-3-hydroxymyristoyl-ACP, yet it can utilize *R*-3-hydroxylauroyl-ACP and *R*-3-hydroxypalmitoyl-ACP, albeit with two orders of magnitude reduction in rate as compared to its natural substrate, demonstrating the existence of a precise molecular hydrocarbon ruler (62, 99, 103). This notion is recapitulated by the fact that in *E. coli* LpxA substitution of Gly173, which is positioned on triangle #9, with an alanine shifts the enzyme's preference to *R*-3-hydroxydecanoyl-ACP (103). Furthermore, the structure of *E. coli* LpxA with its bound lipid product, UDP-3-O-(*R*-3-hydroxymyristoyl)-GlcNAc (UDP-acyl-GlcNAc), has been resolved (104) and identified His191 on triangle #10 as the hydrocarbon ruler that dictates acyl-chain length selectivity (Fig. 3.4).

The CTD domain of LpxA is tethered to the top of the LβH domain and does not appear to play a role in trimerization of the acyltransferase. The bottom side of the CTD is involved in binding the uridine moiety of UDP-GlcNAc, and generates the active site of LpxA along with the adjacent LβH domain and two loops that are inserted into the corners of triangle #5 and #6 (100, 104). Our structure revealed that one ACP molecule is docked between two CTD domains of LpxA, which contradicts an NMR/mutagenesis-directed docking study (107) that had suggested the region between the bottom side of CTD and the two loop insertions to be involved in modulating ACP molecular recognition (Fig. 3.5).

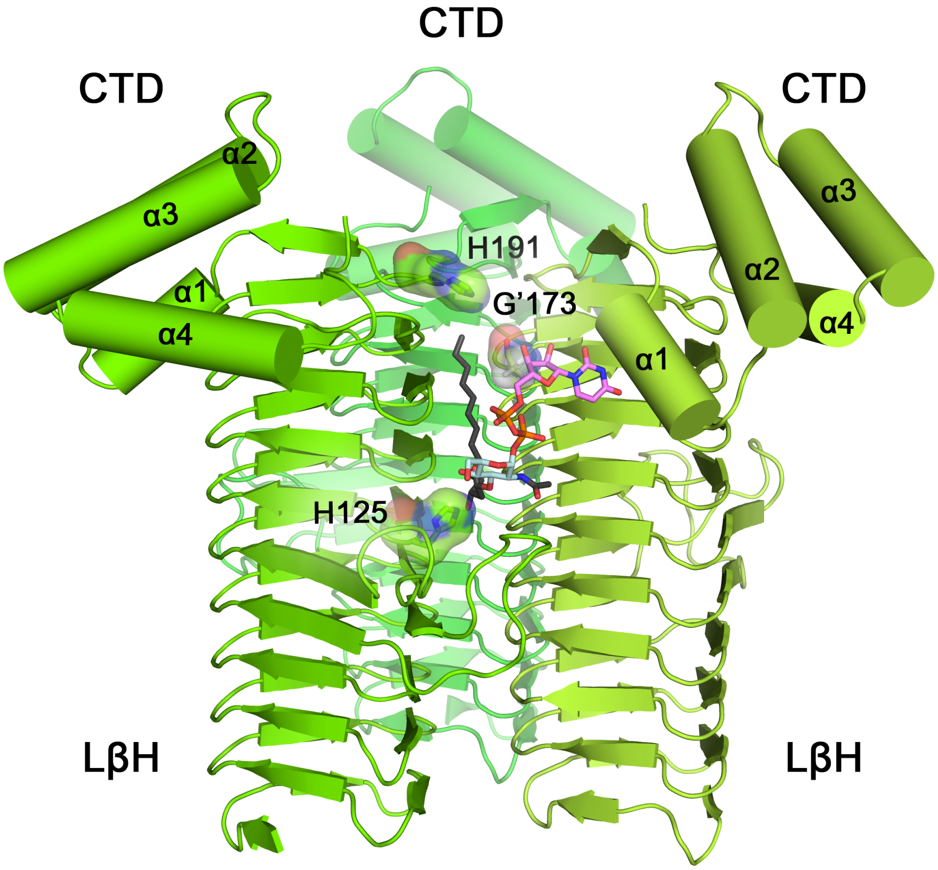

Figure 3.4: The Structure of LpxA solved in complex with UDP-acyl-GlcNAc. The LpxA trimer and a single UDP-acyl-GlcNAc molecule are shown (PDB code: 2QIA). The subdomains of LpxA (different shades of green) are indicated. The side-chain and molecular surface of the catalytic histidine (His125), the hydrocarbon ruler (His191), and glycine 173 are shown. The acyl-chain of the lipid is colored in black. The glucosamine ring and UDP moiety are colored in cyan and pink, respectively.

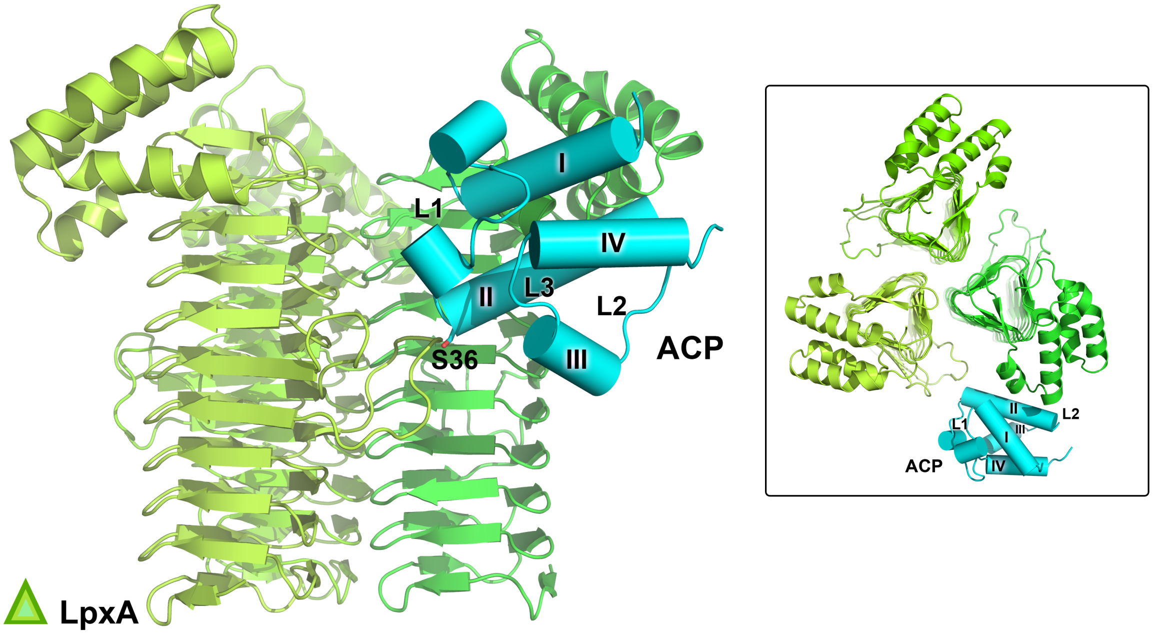

Figure 3.5: The docking model of LpxA:ACP complex. The side view, and the top-down view (inset) of the LpxA:ACP docking model. ACP (cyan) is docked to UDP-GlcNAc binding site.

3.2.2 The LpxA:*holo*-ACP binding interface

Three ACP molecules are bound per LpxA homotrimer (Fig. 3.6a), revealing the stoichiometry of ACP binding to LpxA and suggesting that each active site is capable of transferring acyl-chains simultaneously. Each ACP molecule exclusively contacts two adjacent CTD domains, which provide a binding surface area that measure approximately 630 Å^2. An overlay of the electrostatic surfaces of ACP and LpxA recapitulates the functional relevance of the CTD and shows the charge complementarity between the two protein partners (Fig. 3.6b). Portions of L1 and helix-II in combination with portions of L2 and helix-III form an electronegative surface on ACP that coordinates with two electropositive surface patches on LpxA. Importantly, This interaction orients ACP and its Ser36 towards the active site of LpxA.

The binding surface of LpxA provides a V-shaped groove between the adjoining ARD domains into which ACP is inserted (Fig. 3.6c). There are only a few strong charge-mediated interactions between the two partners that include Asn25, Glu30, and Asp31 from L1 of ACP with Thr228, Glu231, Gln179, Arg262, and Asp230 all exclusively provided by one monomer of LpxA (chain A). Furthermore, His160 and Arg258 that are located on the same LpxA subunit coordinate the 4′-phosphate group, which is covalently attached to Ser36 of ACP. This explains why mutating His160 to alanine or phenylalanine reduces but does not completely abrogate LpxA enzymatic activity (99). There is a multitude of other residues provided by the same LpxA monomer that interact with Ser36 of helix-II and a portion of L1 of ACP. These residues include Gln161, His191, Ala178, Thr257, Gly259, Leu260, and Lys233, some of which are highly conserved (Fig. 3.7). The adjacent LpxA monomer (symmetry related chain A’) provides weak electrostatic as well as van der Waals interactions with helix-II residues and Glu53 and Asp56 that are located on L2 and helix-III of ACP. The residues provided by chain A’ (denoted by prime symbols) are Glu’188, Phe’195, Ile’186, Glu’200, Gly’196, Ile’199, Lys’203, Arg’224, Val’197, Arg’216, Lys’220, and Arg’209.

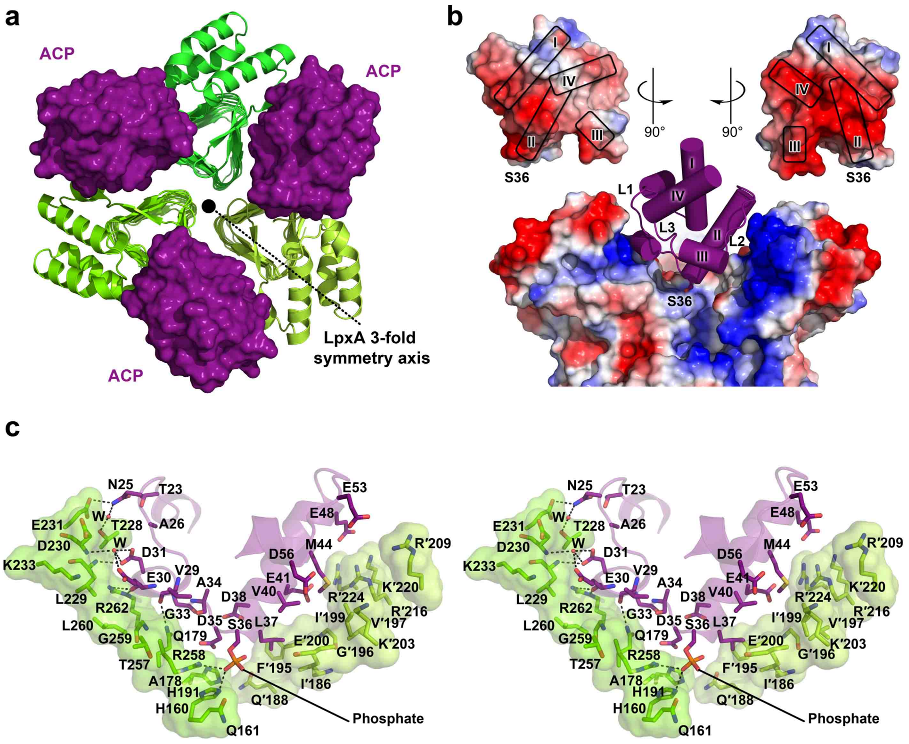

Figure 3.6: Overview of the LpxA:*holo*-ACP interactions. (a) Top-down view of the LpxA:*holo*-ACP complex. Three ACP molecules bind per LpxA trimer. **(b)** Electrostatic surface representation of the CTD and ACP (insets). The surface potential contours were scaled to +79.2 (blue) and -79.2 (red) $k_B T e^{-1}$ (where k_B is the Boltzmann constant, T is temperature and e^{-1} is the charge of an electron). **(c)** Stereoview of the LpxA:*holo*-ACP complex. Residues at the protein-protein interface are shown. The molecular surfaces of LpxA residues are displayed. Electrostatic interactions are indicated by dashed lines.

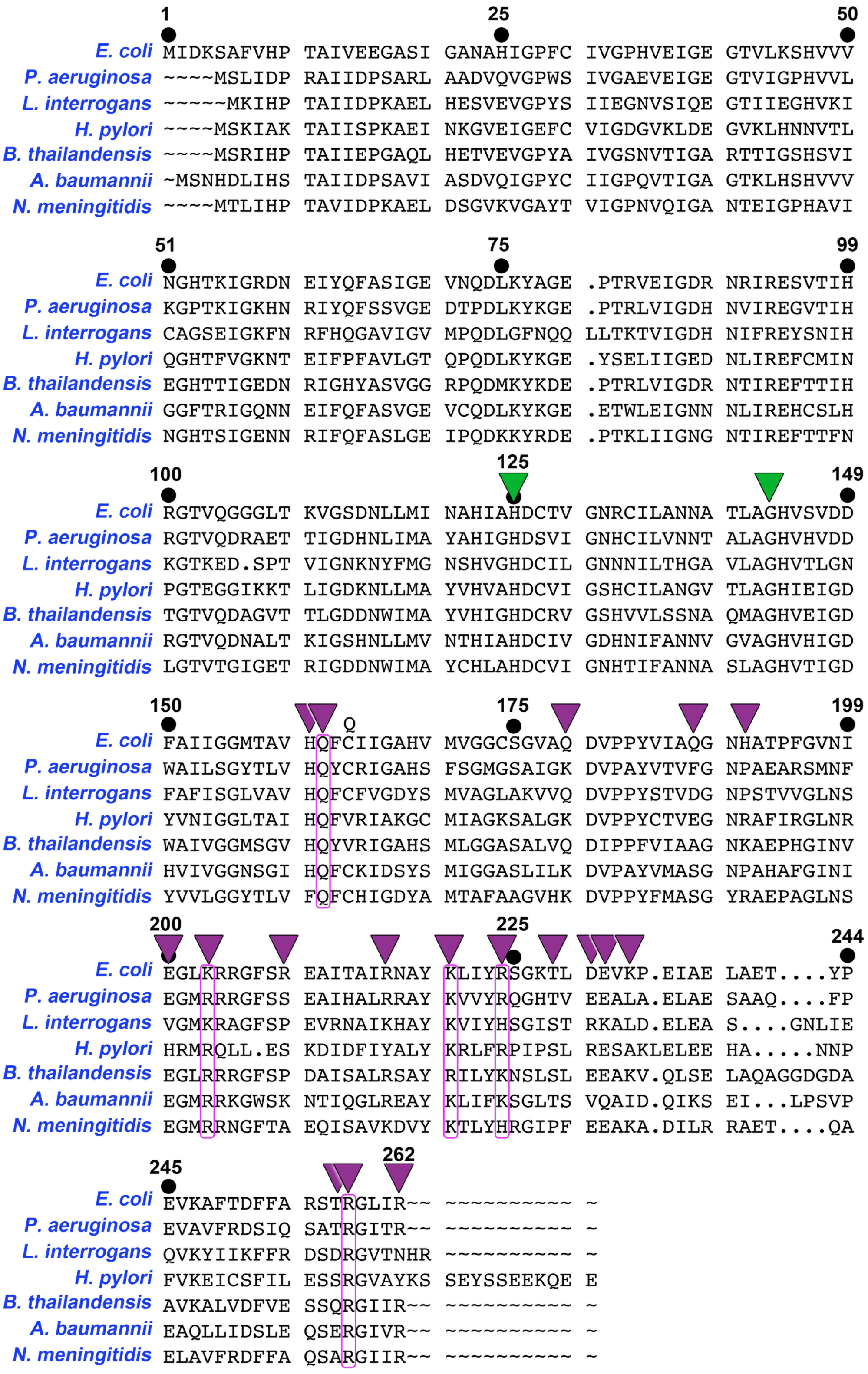

```
                  1                       25                        50
E. coli           MIDKSAFVHP TAIVEEGASI GANAHIGPFC IVGPHVEIGE GTVLKSHVVV
P. aeruginosa     ~~~~MSLIDP RAIIDPSARL AADVQVGPWS IVGAEVEIGE GTVIGPHVVL
L. interrogans    ~~~~~MKIHP TAIIDPKAEL HESVEVGPYS IIEGNVSIQE GTIIEGHVKI
H. pylori         ~~~~MSKIAK TAIISPKAEI NKGVEIGEFC VIGDGVKLDE GVKLHNNVTL
B. thailandensis  ~~~~MSRIHP TAIIEPGAQL HETVEVGPYA IVGSNVTIGA RTTIGSHSVI
A. baumannii      ~MSNHDLIHS TAIIDPSAVI ASDVQIGPYC IIGPQVTIGA GTKLHSHVVV
N. meningitidis   ~~~~MTLIHP TAVIDPKAEL DSGVKVGAYT VIGPNVQIGA NTEIGPHAVI

                  51                      75                        99
E. coli           NGHTKIGRDN EIYQFASIGE VNQDLKYAGE .PTRVEIGDR NRIRESVTIH
P. aeruginosa     KGPTKIGKHN RIYQFSSVGE DTPDLKYKGE .PTRLVIGDH NVIREGVTIH
L. interrogans    CAGSEIGKFN RFHQGAVIGV MPQDLGFNQQ LLTKTVIGDH NIFREYSNIH
H. pylori         QGHTFVGKNT EIFPFAVLGT QPQDLKYKGE .YSELIIGED NLIREFCMIN
B. thailandensis  EGHTTIGEDN RIGHYASVGG RPQDMKYKDE .PTRLVIGDR NTIREFTTIH
A. baumannii      GGFTRIGQNN EIFQFASVGE VCQDLKYKGE .ETWLEIGNN NLIREHCSLH
N. meningitidis   NGHTSIGENN RIFQFASLGE IPQDKKYRDE .PTKLIIGNG NTIREFTTFN

                  100                      125                      149
E. coli           RGTVQGGGLT KVGSDNLLMI NAHIAHDCTV GNRCILANNA TLAGHVSVDD
P. aeruginosa     RGTVQDRAET TIGDHNLIMA YAHIGHDSVI GNHCILVNNT ALAGHVHVDD
L. interrogans    KGTKED.SPT VIGNKNYFMG NSHVGHDCIL GNNNILTHGA VLAGHVTLGN
H. pylori         PGTEGGIKKT LIGDKNLLMA YVHVAHDCVI GSHCILANGV TLAGHIEIGD
B. thailandensis  TGTVQDAGVT TLGDDNWIMA YVHIGHDCRV GSHVVLSSNA QMAGHVEIGD
A. baumannii      RGTVQDNALT KIGSHNLLMV NTHIAHDCIV GDHNIFANNV GVAGHVHIGD
N. meningitidis   LGTVTGIGET RIGDDNWIMA YCHLAHDCVI GNHTIFANNA SLAGHVTIGD

                  150           Q          175                      199
E. coli           FAIIGGMTAV HQFCIIGAHV MVGGCSGVAQ DVPPYVIAQG NHATPFGVNI
P. aeruginosa     WAILSGYTLV HQYCRIGAHS FSGMGSAIGK DVPAYVTVFG NPAEARSMNF
L. interrogans    FAFISGLVAV HQFCFVGDYS MVAGLAKVVQ DVPPYSTVDG NPSTVVGLNS
H. pylori         YVNIGGLTAI HQFVRIAKGC MIAGKSALGK DVPPYCTVEG NRAFIRGLNR
B. thailandensis  WAIVGGMSGV HQYVRIGAHS MLGGASALVQ DIPPFVIAAG NKAEPHGINV
A. baumannii      HVIVGGNSGI HQFCKIDSYS MIGGASLILK DVPAYVMASG NPAHAFGINI
N. meningitidis   YVVLGGYTLV FQFCHIGDYA MTAFAAGVHK DVPPYFMASG YRAEPAGLNS

                  200                      225                      244
E. coli           EGLKRRGFSR EAITAIRNAY KLIYRSGKTL DEVKP.EIAE LAET....YP
P. aeruginosa     EGMRRRGFSS EAIHALRRAY KVVYRQGHTV EEALA.ELAE SAAQ....FP
L. interrogans    VGMKRAGFSP EVRNAIKHAY KVIYHSGIST RKALD.ELEA S....GNLIE
H. pylori         HRMRQLL.ES KDIDFIYALY KRLFRPIPSL RESAKLELEE HA.....NNP
B. thailandensis  EGLRRRGFSP DAISALRSAY RILYKNSLSL EEAKV.QLSE LAQAGGDGDA
A. baumannii      EGMRRKGWSK NTIQGLREAY KLIFKSGLTS VQAID.QIKS EI...LPSVP
N. meningitidis   EGMRRNGFTA EQISAVKDVY KTLYHRGIPF EEAKA.DILR RAET....QA

                  245             262
E. coli           EVKAFTDFFA RSTRGLIR~~ ~~~~~~~~~~ ~
P. aeruginosa     EVAVFRDSIQ SATRGITR~~ ~~~~~~~~~~ ~
L. interrogans    QVKYIIKFFR DSDRGVTNHR ~~~~~~~~~~ ~
H. pylori         FVKEICSFIL ESSRGVAYKS SEYSSEEKQE E
B. thailandensis  AVKALVDFVE SSQRGIIR~~ ~~~~~~~~~~ ~
A. baumannii      EAQLLIDSLE QSERGIVR~~ ~~~~~~~~~~ ~
N. meningitidis   ELAVFRDFFA QSARGIIR~~ ~~~~~~~~~~ ~
```

Figure 3.7: Sequence alignment of LpxA orthologs. Protein sequence alignment of *E. coli* LpxA with *Pseudomonas aeruginosa, Leptospira interrogans, Helicobacter pylori, Burkholderia thailandensis, Acinetobacter baumannii,* and *Neisseria meningitides*. The amino acid numbers are presented above the aligned sequences and marked by black circles. The catalytic histidine (His125 in *E. coli*) and the oxyanion hole (Gly143 in *E.coli*) are indicated by green rectangles above the aligned sequences. The charged and polar residues in the protein–protein interface are indicated by purple triangles. The purple box highlights those polar residues at the binding interface that display absolute charge conservation.

A mutagenesis study of *Vibrio harveyi acyl*-ACP, which shares 86% sequence identity with its *E. coli* counterpart, revealed that neutralizing Asp30 (glutamate in *E. coli*), Asp35, and Asp38 (site A residues) by substituting them to asparagine reduces *E. coli* LpxA activity by 40% as compared to LpxA activity measured in the presence of wild-type *V. harveyi acyl*-ACP (79). Moreover, neutralizing Glu47, Asp51, Glu53, and Asp56 (site B residues) reduces LpxA activity by 95%, implying a role for these residues in LpxA interaction (79). Surprisingly, based on our structure, none of these residues form a salt bridge with LpxA. Our recently published comparison between *holo*-ACP and *acyl*-ACP bound to LpxD *N*-acyltransferase, sheds light on this paradox (144). *Acyl*-ACP binding to LpxD involved electrostatic interaction of Asp35, Asp38, Glu41, Glu48, Glu53, and Asp56 with basic amino acids of LpxD. In contrast, because of considerable conformational change in L2 and helix-III, *holo*-ACP lacked any strong electrostatic contacts at Glu48, Glu53, and Asp56 sites. The collapse of these electrostatic interactions appears to initiate the dissociation event that must occur with *holo*-ACP. In the case of LpxA, perhaps strong electrostatic interactions with site A and B residues could have been visualized had *acyl*-ACP been captured bound to LpxA instead of the *holo*-form.

3.2.3 Mechanism of acyl-chain delivery by ACP

Superimposing *holo*-ACP with the X-ray structure of *E. coli acyl*-ACP (74), whose decanoyl acyl-chain is buried inside the carrier-protein and covalently attached to the 4′-

phosphopantetheine group, suggests that *acyl*-ACP must undergo a conformational change in order to present its cargo to LpxA and properly orient the thioester bond relative to the active site histidine (His125) for acyl-transfer to occur (Fig. 3.8). The crystallographic study of *Leptospira interrogans* LpxA bound to a substrate mimetic, *R*-3-hydroxylauroyl-methyl-phosphopantetheine (*R*-3-OHC$_{12}$-methyl-4′-PPT), has revealed the conformation of 4′-phosphopantetheine as it relates to acyl substrate delivery (105). The electron density was poor in some regions of the phosphopantetheine, and two conformations were modeled for the methyl-phosphopantetheine moiety of the ligand with the 4′-phosphate groups positioned approximately 7 Å apart. Both conformations place the thioester bond in proximity of the catalytic base histidine and pack the acyl-chain inside the hydrophobic pocket formed by adjacent LβH domains. When superimposed with our structure, the location of the 4′-phosphate group associated with conformation 1 overlays with little deviation, indicating its catalytic relevance over the alternate conformation in *E. coli* LpxA (Fig. 3.9).

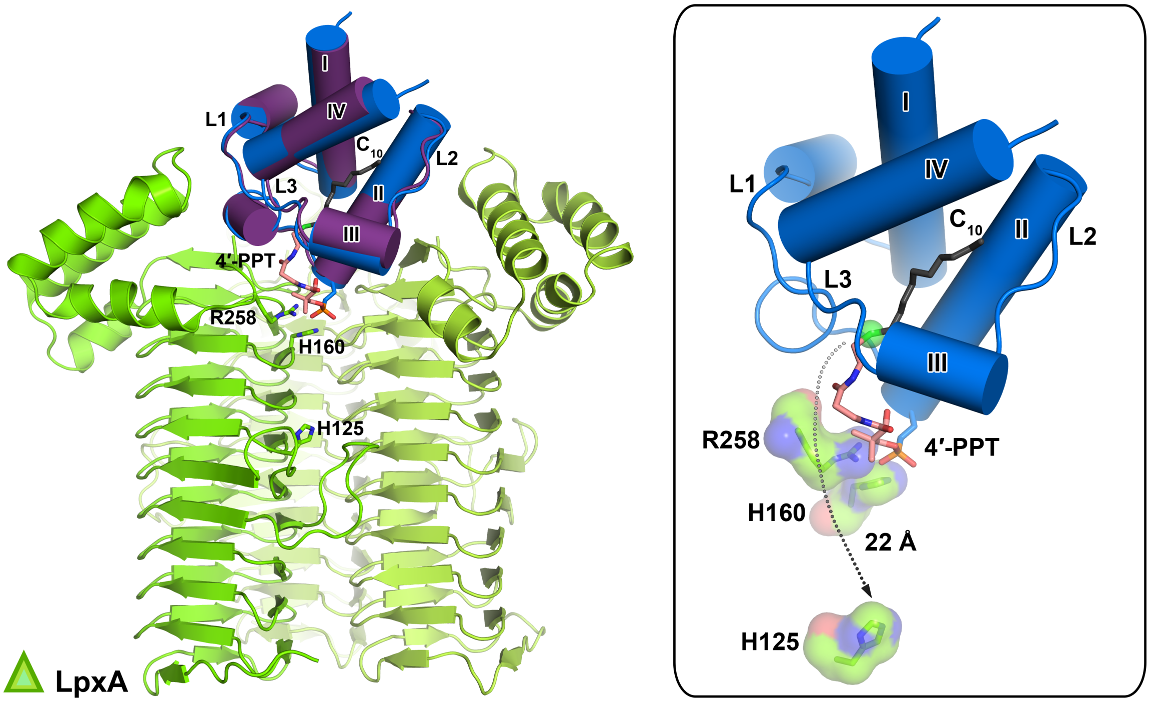

Figure 3.8: Overlay of *acyl*-ACP with LpxA:*holo*-ACP complex. Decanoyl-ACP (blue, PDB code: 2FAE) superimposed with *holo*-ACP (Purple). The two basic residues (His160, and Arg125) that interact with 4′-phosphate of *holo*-ACP and the catalytic base (His125) are shown. ACP needs to eject the acyl-chain (black) to place the thioester bond (green circle) in the active site of LpxA that is approximately 22 Å away (inset).

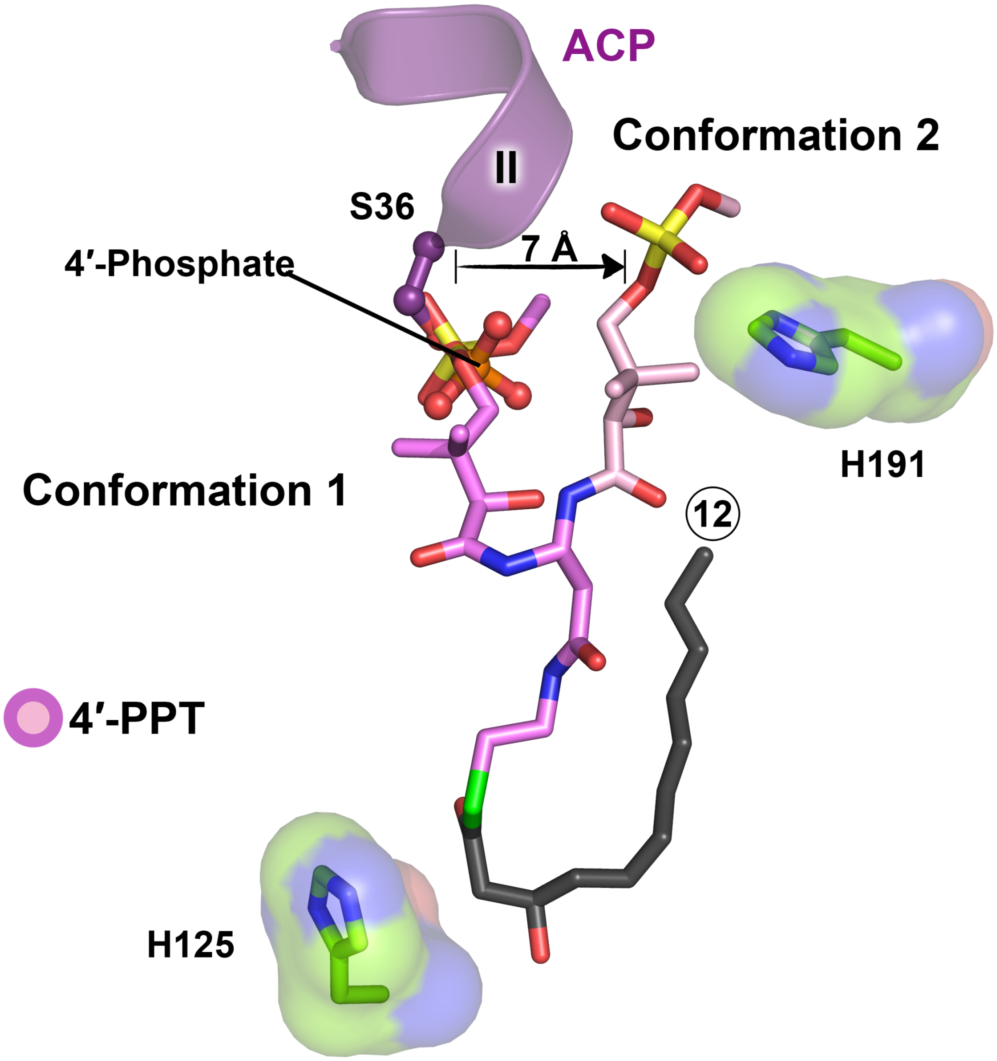

Figure 3.9: Superposition of *R*-3-OHC12-methyl-4′-PPT bound to *L. interrogans* LpxA (PDB code: 3I3A) with the LpxA:*holo*-ACP complex. Two conformations of 4′-PPT moiety are shown by two shades of pink and colored by atom type. The acyl-chain is colored in black with its length indicated. Ser36 of *holo*-ACP and its attached 4′-phosphate group, the catalytic base (His125) and the hydrocarbon ruler (His191) of *E. coli* LpxA are shown and are colored as in figure 3.6. The 4′-phosphate group of conformation 1 overlaps with the phosphate group of *holo*-ACP.

3.2.4 Inhibition of LpxA by peptide-920

As an essential enzyme in the lipid A biosynthesis, LpxA remains a promising candidate for the design of novel antibiotics. It has been shown that a pentadecapeptide inhibitor of LpxA, termed peptide-920 (SSGWMLDPIAGKWSR), when expressed as GST-fusion protein, could inhibit bacterial growth (109). Kinetic studies suggested peptide-920 binds tightly to LpxA (K_i = 50 nM) (108). Moreover, when assayed in the presence of 1 μM UDP-GlcNAc and 1 μM R-3-hydroxymyristoyl-ACP, peptide-920 inhibited LpxA reaction with an IC_{50} of 60 nM. Changing the concentration of *acyl*-ACP in the inhibition assay to 100 μM increased the IC_{50} value by approximately 12-fold to 730 μM, whereas increasing the concentration of UDP-GlcNAc to 5 mM had no major effect on the IC_{50} value. Based on these data, it was concluded that peptide-920 inhibits LpxA reaction by competing with *acyl*-ACP (108). The crystal structure of *E. coli* LpxA with peptide-920 has been reported (108). It is clear from superimposing this structure with LpxA:*holo*-ACP and LpxA:*R*-3-OHC$_{12}$-methyl-4′-PPT complex that peptide-920 competes with the acyl-phosphopantetheine moiety of ACP, and does not prevent direct protein:protein interactions (Fig. 3.10a). Notably, overlaying the structure of LpxA bound to UDP-GlcNAc (100) reveals that Leu6, and Trp13 of peptide-920 occlude the uridine and β-phosphate binding site (Fig. 3.10b). Our study on *holo*-ACP bound to LpxA provides new insights into the optimization of peptide-920 that exploits disruption of the protein:protein interface in an effort to design new antibiotic therapeutics.

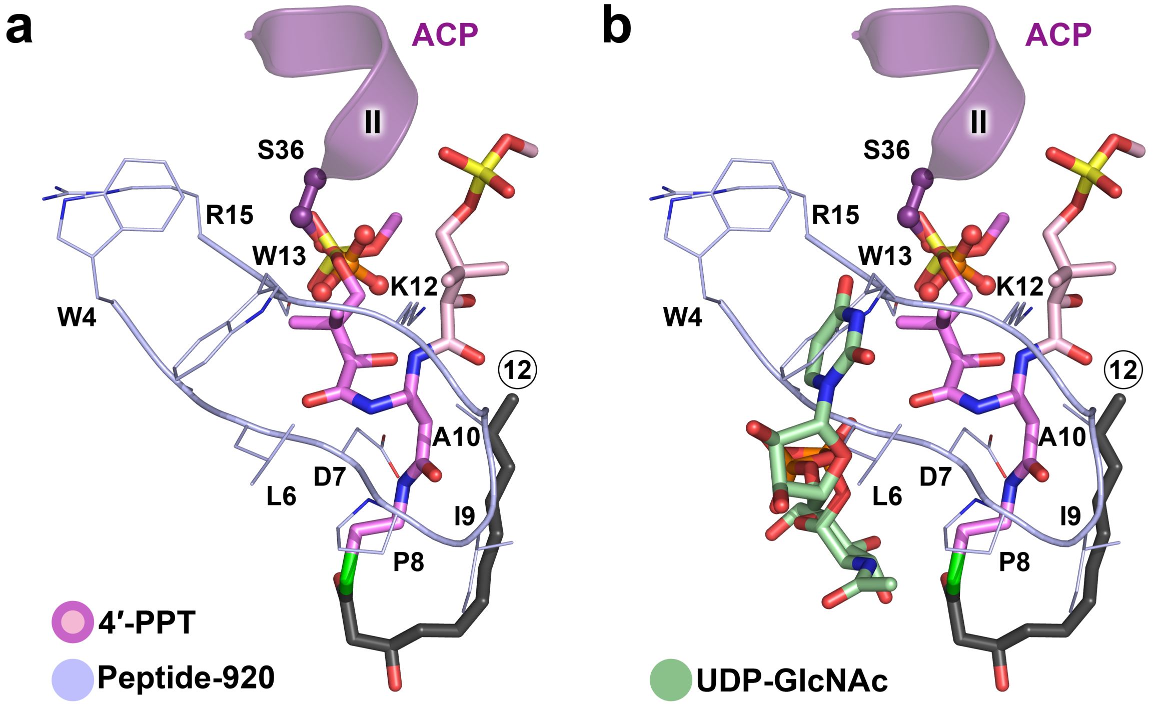

Figure 3.10: Overlay of LpxA:*holo*-ACP with other LpxA complexes. (a) Superposition of peptide-920 complex (PDB code: 2AQ9, blue) with *holo*-ACP and *R*-3-OHC$_{12}$-methyl-4′-PPT complexes. The side chains of peptide-920 are shown and colored by atom. The peptide blocks binding of acyl-4′-PPT to LpxA. **(b)** Superposition of UDP-GlcNAc complex structure (PDB code: 2JF3, green) with peptide-920 complex. Peptide-920 inhibits LpxA activity by binding to the UDP-GlcNAc and acyl-4′-PPT binding sites.

3.2.5 LpxA *O*-acyltransferase versus LpxD *N*-acyltransferase

LpxA and LpxD are closely related acyltransferases that share the unique LβH trimeric structure and the use of *R*-3-hydroxymyristoyl-ACP as a substrate. Two adjacent LβH domains in both LpxA and LpxD form a hydrophobic pocket that accommodates the acyl-chain delivered by ACP (104, 144). We recently identified a second hydrophobic surface feature on LpxD that is formed by a single LβH, accommodating the acyl moiety of its lipid substrate, UDP-acyl-GlcN (Fig. 3.11) (144). In comparing LpxA and LpxD structures, it appears that a similar hydrophobic pocket exists on LpxA that could potentially accommodate an additional acyl-chain (Fig. 3.12a). Given the resemblance between the substrates and products of LpxA and LpxD reactions, as well as the structural similarity between the two acyltransferases, the question arises whether LpxA is able to catalyze the LpxD reaction. Interestingly, when assayed in the presence of LpxD substrates (*acyl*-ACP and UDP-acyl-GlcN), LpxA showed no acyl-transfer activity, indicating its strong specificity for ester-linkage formation (Fig. 3.12b). We hypothesize that the CTD domain of LpxA locks the UDP moiety of the substrate in a conformation that only allows the 3-hydroxyl group to be properly oriented relative to the catalytic residue (His125) in the active site for nucleophilic attack to occur. It is worth mentioning that LpxD utilizes its CTD domain solely for ACP binding and instead has evolved an additional globular domain at its N-terminal end to bind the uridine moiety of UDP-acyl-GlcN such that amide-linkage formation would take place.

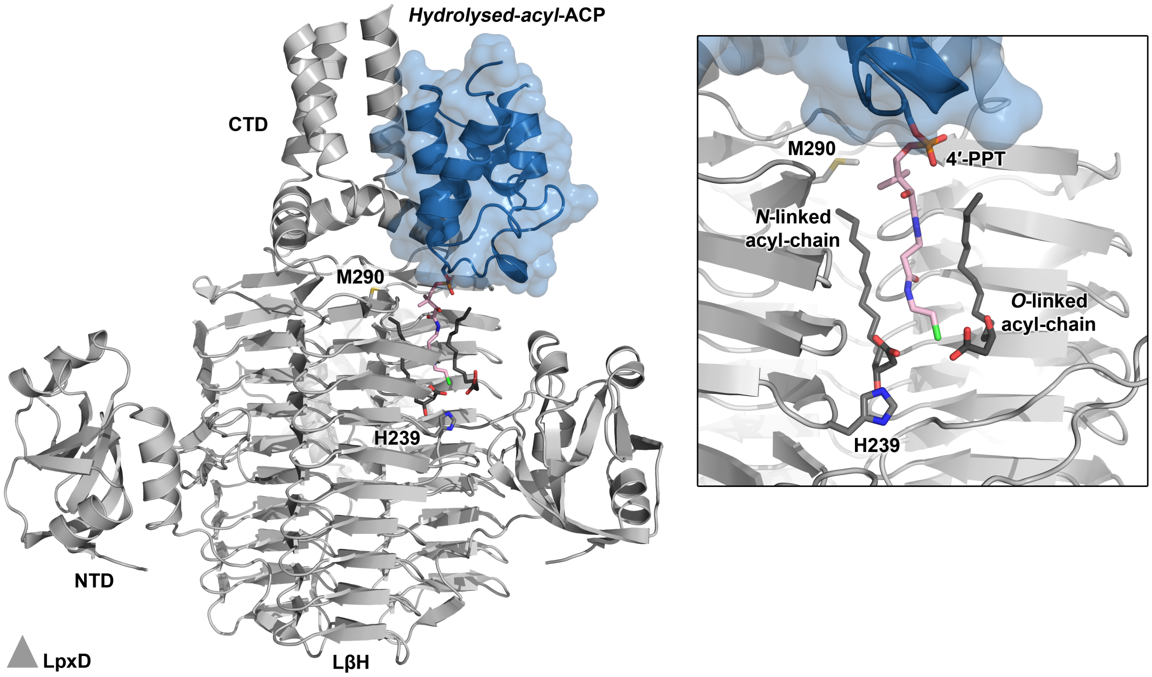

Figure 3.11: Structure of *E. coli* LpxD bound to *hydrolysed-acyl*-ACP. LpxD trimer (gray) and a single molecule of ACP (blue) are shown (PDB code: 4IHG). ACP is bound to the C-terminal helices of LpxD. The thioester bond between the 4′-phosphopantetheine (pink) and the acyl chain (black) delivered by ACP is hydrolyzed. The catalytic base (His239) and the hydrocarbon ruler (M290) are shown. (inset) *N*-linked acyl-chain delivered by ACP is packed into a pocket provided by two neighboring LβH domains. *O*-linked acyl-chain represents the acyl moiety of the LpxD substrate, UDP-acyl-GlcN, and is bound to a single LβH domain.

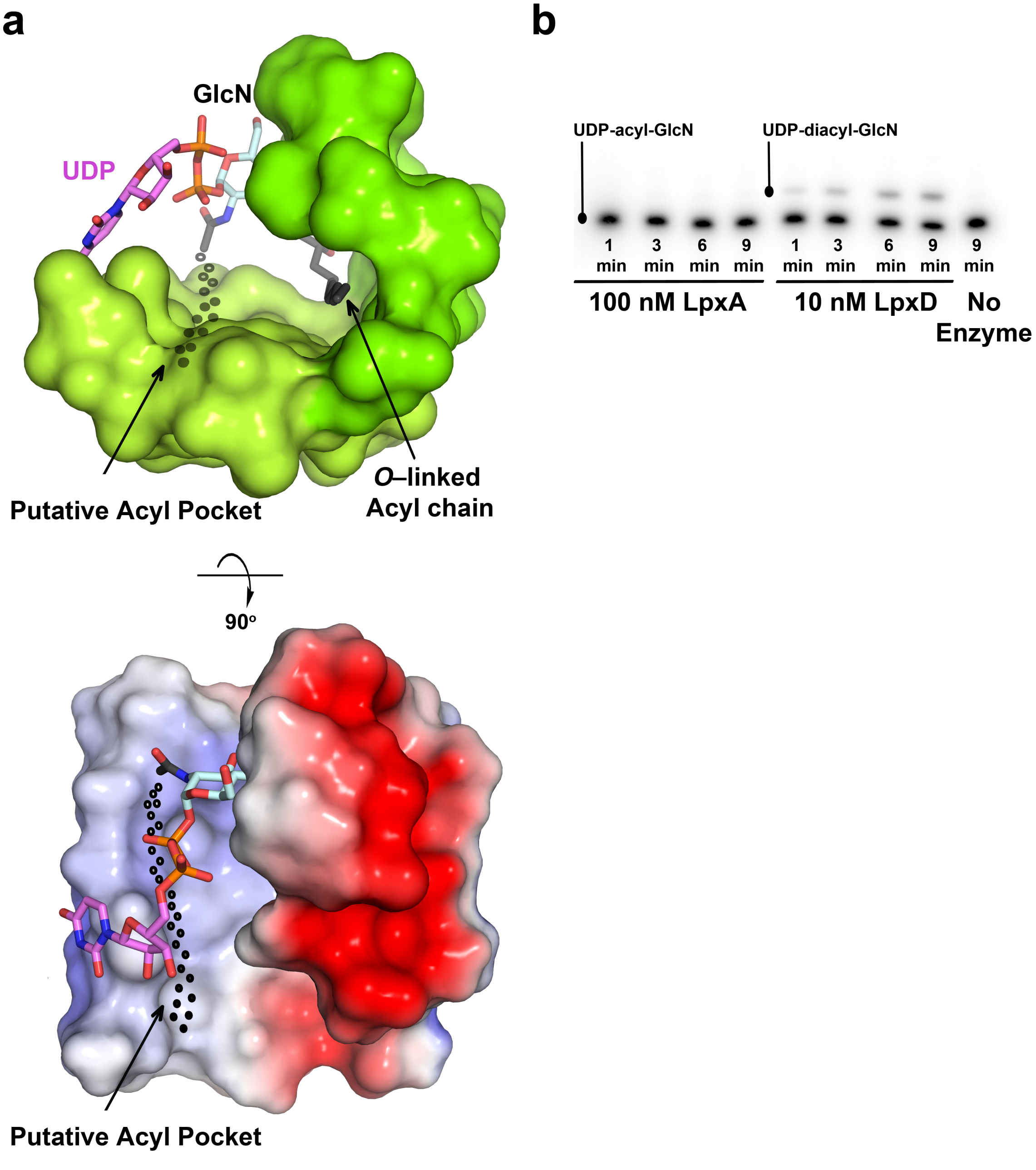
a
GlcN
UDP
Putative Acyl Pocket
O–linked
Acyl chain
90°
Putative Acyl Pocket
b
UDP-acyl-GlcN
UDP-diacyl-GlcN
1 min
3 min
6 min
9 min
1 min
3 min
6 min
9 min
9 min
100 nM LpxA
10 nM LpxD
No Enzyme

Figure 3.12: Functional surface of LpxA and comparison with LpxD. (a) Putative acyl-chain pocket on LpxA surface. The molecular (top) and electrostatic (bottom, scaled to +79.2 (blue) and -79.2 (red) $k_B T e^{-1}$) surfaces of LpxA structure bound to UDP-acyl-GlcNAc are shown (PDB code: 2QIA). The location of the additional acyl-chain pocket is indicated by dots. **(b)** TLC-based radiographic UDP-acyl-GlcN acylation assay. 25 μL assay mixture contained 40 mM HEPES (pH 7.5), 10 μM *R*-3-hydroxymyristoyl-ACP, 10 μM [α-^{32}P]-UDP-3-*O*-(*R*-3-hydroxymyristoyl)-glucosamine (~2×10^4 cpm μL^{-1}), and 1 mg ml^{-1} bovine serum albumin. The reaction was initiated at 30 °C by adding 10 nM LpxD or 100 nM LpxA to the mixture, and time points were taken by spotting 2 μL of the mixture onto a silica gel 60 TLC plate. The plate was developed with chloroform/methanol/water/acetic acid (25:15:4:2, v:v:v:v) and analyzed with a Phosphor Imager. UDP-acyl-GlcN substrate and UDP-diacyl-GlcN product are indicated.

3.3 Discussion

Acyltransferases are the single most abundant class of partner enzymes in Gram-negative microorganisms that associate with ACP (56). The structure presented in this study shows *holo*-ACP engaging LpxA and helps to better understand ACP-based interactions. ACP binding to LpxA and LpxD (144) highlights a remarkable promiscuity that ACP displays towards its numerous partner enzymes (Fig. 3.13). Although helix-II is the key modulator of ACP recognition providing interaction with LpxA and –D, the contribution of helix-III, L1, and L2 to the interfacial contacts is different between the two acyltransferases. Helix-III and L2 provide extensive molecular interaction with LpxD, whereas their contribution in the case of LpxA is subsidiary. Instead, ACP provides more molecular interaction with LpxA along L1. The spatial arrangement of the C-terminal helices of the two enzymes determines what regions on ACP surface participate in binding. The C-terminal helices in LpxA fold back on themselves and interact solely with their respective LβH domain, but the C-terminal helices of LpxD monomers interdigitate to form a three-helix bundle (Fig. 3.14). Nonetheless, ACP relies on "electrostatic steering" and shape complementarity for association.

Crystallizing *acyl*-ACP with LpxA will be invaluable, as it may uncover additional molecular interactions at the protein–protein interface and provide insight into intra-ACP movements. It is an interesting possibility that based on the structural analyses presented here a chimera LβH acyltransferase could be engineered to fulfill the catalytic role of both LpxA and LpxD. Furthermore, given that specific LpxA inhibitors have been reported (109, 145) it is reasonable to envision that the high-resolution structural insights gleaned from our work may facilitate such efforts to design potent anti-bacterial agents.

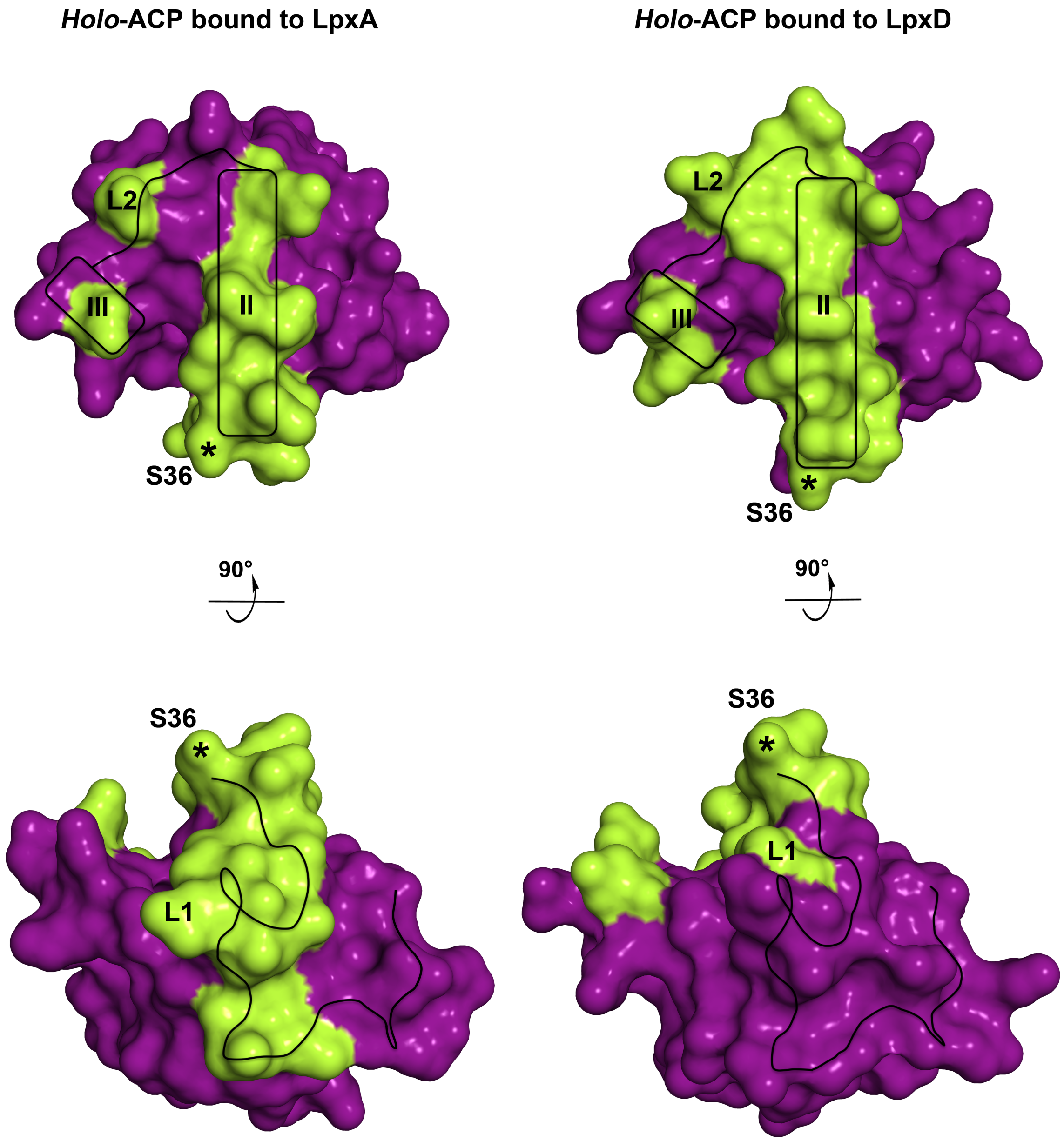

Holo-ACP bound to LpxA

Holo-ACP bound to LpxD

Figure 3.13: Binding surface of *holo*-ACP in LpxA and –D complexes. ACP (purple) binds LpxA and –D differently. Surface residues of *holo*-ACP involved in interaction with LpxA (left) and –D (right, PDB code: 4IHH) are highlighted in green. L1 region of *holo*-ACP makes more contacts with LpxA, whereas helix-II, L2, and helix-III are more involved in interaction with LpxD.

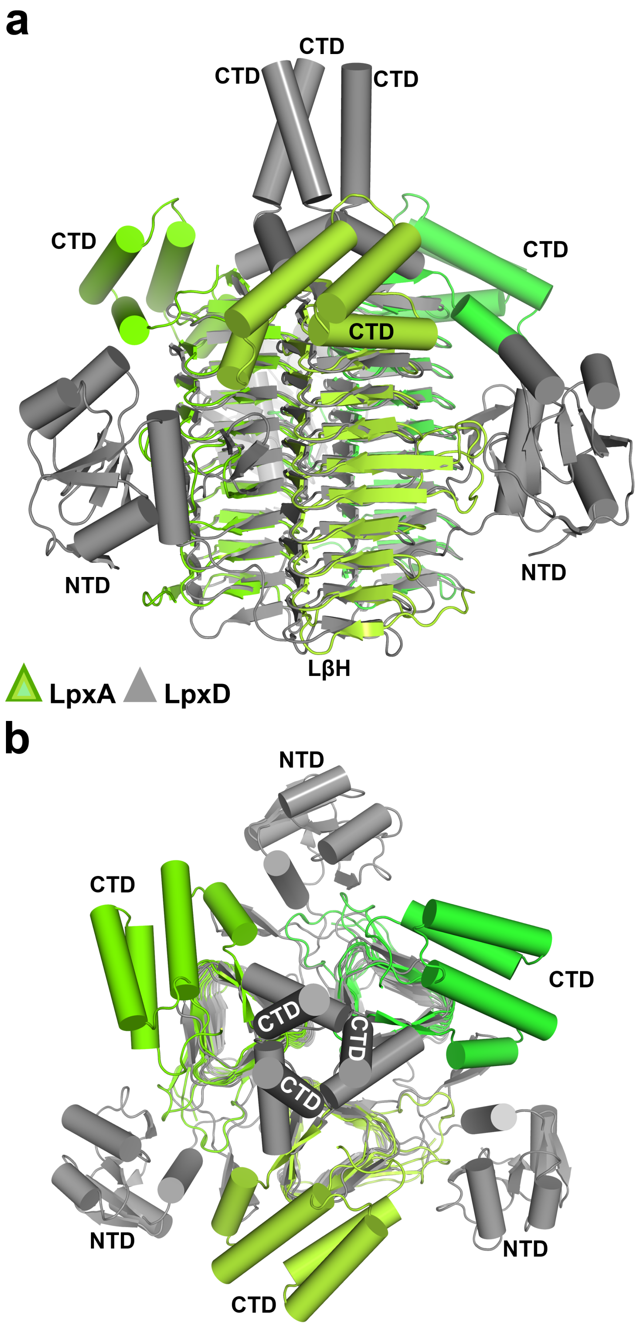

Figure 3.14: Structural comparison of *E. coli* LpxA and LpxD. (a) Side view of LpxA (green) and LpxD (gray) superimposition. The subdomains of each structure are shown. The globular NTD domain of LpxD has no counterpart in LpxA. **(b)** Top-down view of superimposed LpxA and LpxD. The C-terminal helices of LpxD monomers form a three-helix bundle. The CTDs of LpxA monomers are collapsed and interact solely with their representative LβH domains.

3.4 Methods

3.4.1 Cloning of His_6–LpxA

The *lpxA* gene was amplified by polymerase chain reaction (PCR) from *E. coli* W3110A genomic DNA using the KOD Hot Start Kit (EMD Chemicals, CA) and the following primer pair (Integrated DNA Technologies, IA): 5′–GCGCGCGCCATATGGGCCATCATCATCATCATCATGGCATGATTGATAAATCCGCCT–3′ and 5′–GCGCGCGCGGATCCTTAACGAATCAGACCGCGCGT–3′. The former primer was designed to confer an *Nde*I restriction site and a coding region for Met–Gly–His_6–Gly upstream of the *lpxA* start codon. The latter primer introduced a *BamH*I restriction site downstream of the *lpxA* stop codon. The linear PCR product was isolated from an agarose gel following gel electrophoresis using the QIAquick Gel Extraction Kit (Qiagen, CA), and subsequently digested with *Nde*I and *BamH*I (New England Biolabs, MA). The digested linear DNA was purified using the QIAquick PCR Purification Kit (Qiagen, CA), and ligated into a similarly cut pET21b expression vector (EMD Millipore, MA) with T4 DNA ligase (New England Biolabs, MA). The expression vector was transformed into DH5α chemically competent cells (Invitrogen, CA), and transformants were selected on a LB-agar plate supplemented with 100 μg mL^{-1} ampicillin at 37 °C. Minipreparation of the expression vector encoding LpxA with an uncleavable N-terminal histidine-tag (designated pET21b-SAM) was performed with a

Qiagen Mini-Prep Kit (Qiagen, CA), and its sequence was confirmed by DNA sequencing (Eton Bioscience, CA) using T7–promoter and –terminator primers.

3.4.2 Expression and purification of His$_6$–LpxA

A 15 mL culture of C41(DE3) bacterial cells harboring the pET21b-SAM expression vector was grown overnight at 37 °C and used to inoculate 1.5 L of lysogeny broth (LB) supplemented with 100 μg mL^{-1} ampicilin. When the culture reached an OD$_{600}$ of 0.6, the expression of His$_6$–LpxA was induced by the addition of 1 mM isopropyl-β-D-thio-galactoside (IPTG). After 3.5 hours of induction at 37 °C, the cells were harvested by centrifugation at 8,000 × g for 20 minutes at 4 °C, and washed with 20 mM 4-(2-hydroxyethyl)-1-piperazineethanesulfonic acid (HEPES), pH 8.0. The following procedures were carried out at 0-4 °C. Approximately 6 g of wet cell pellet was resuspended in Buffer A (20 mM HEPES, pH 8.0, 500 mM NaCl, 10% glycerol, 1 mM DTT) supplemented with 25 mM imidazole, and lysed by two passage through a FRENCH pressure cell (Spectronic Instruments Inc., NY) at 11,000 psi. The unbroken cells, cell debris, and membranes were removed by centrifugation at 100,000 × g for 1 hour. The soluble fraction was rocked with 5 ml of Ni-NTA (Qiagen, CA) for 30 minutes, and the mixture was loaded onto an empty Econo-Column (Bio-Rad Laboratories, CA). The column was washed with Buffer A and 25 mM imidazole over 10 column-volumes, and His$_6$–LpxA was eluted in one step with 5 column-volumes of Buffer A and 200 mM imidazole. The elution sample, was then concentrated to ~10 mL and loaded onto a High Load 26/60 Superdex 200 gel filtration column (GE Healthcare, WI) attached to an ÄKTA$_{FPLC}$ system (GE Healthcare, WI) and equilibrated with 10 mM Tris-HCl, pH 7.5, 200 mM NaCl, and 10% glycerol. The protein sample was run over the column at a flow rate of 1.0 mL min^{-1}, and the fractions corresponding to the major A_{280} peak were pooled based on their purity as determined by sodium dodecyl sulfate-polyacrylamide gel electrophoresis (SDS-PAGE). His$_6$–LpxA was concentrated to ~67 mg mL^{-1} and saved in aliquots at –80 ˚C.

3.4.3 Production of *holo*-ACP and *acyl*-ACP

E. coli holo-ACP was preloaded with its 4′-PPT prosthetic group by expressing pET16b*-AM vector (144) in C41(DE3) *E. coli* cells (124), cultured at 37 ˚C in 1 L of LB broth, and purified by nickel affinity, anion exchange, covalent chromatography that exploits disulfide bond formation between the 4′-PPT group and Thiopropyl Sepharose resin (Sigma-Aldrich, MO), and finally size-exclusion chromatography as described in Chapter 2. Upon purifying *holo*-ACP to homogeneity it was concentrated to ~19 mg mL^{-1}, and stored in aliquots at −80 ˚C to be utilized for crystallization trials.

To generate *acyl*-ACP, purified *holo*-ACP was charged with *R*-3-hydroxymyristic acid enzymatically using the soluble form of *acyl*-ACP synthetase from *Vibrio harveyi*, and purified as explained in Chapter 2. Purified *acyl*-ACP was concentrated to ~18 mg mL^{-1}, and stored at −80 ˚C in a buffer containing 10 mM Tris-HCl (pH 7.5), and 200 mM NaCl to be used in crystallization trials.

3.4.4 LpxA radioactive substrate prep and *in vitro* assay

The [α-^{32}P]-UDP-GlcNAc substrate was prepared as previously reported (99). The LpxA-catalyzed conversion of [α-^{32}P]-UDP-GlcNAc to [α-^{32}P]-UDP-3-O-(*R*-3-hydroxymyristoyl)-GlcNAc was monitored by thin-layer chromatography (TLC) on a silica gel 60 plate (EMD Chemicals, Germany). The standard reaction mixture (25 μL) contained 40 mM HEPES, pH 7.5, 1 mg mL^{-1} bovine serum albumin (BSA), 10 μM R-3-hydroxymyristoyl-ACP, and 10 μM [α-^{32}P]-UDP-GlcNAc (~2 × 10^4 cpm μL^{-1}). The mixture was equilibrated at 30 °C for 3 minutes, and the reaction was initiated with the addition 10 μM His$_6$–LpxA enzyme. A volume of 2 μL per representative time point of the reaction course was spotted on the TLC plate. The silica gel 60 TLC plate was developed with chloroform/methanol/water/acetic acid (25:15:4:2, v:v:v:v) and analyzed with a Phosphor Imager. The specific activity of His$_6$–LpxA was measured in triplicate (130 nmol min^{-1} mg) and was approximately 3-fold higher than the specific activity of non-tagged *E. coli* LpxA (146).

3.4.5 Thin-layer chromatography based radiographic UDP-acyl-GlcN acylation assay

The [α-^{32}P]-UDP-3-O-(R-3-hydroxymyristoyl)-GlcNAc substrate was prepared as previously reported (36). 25 µL assay mixture contained 40 mM HEPES (pH 7.5), 10 µM R-3-hydroxymyristoyl-ACP, 10 µM [α-32P]-UDP-3-O-(R-3-hydroxymyristoyl)-glucosamine (~2 × 104 cpm µL-1), and 1 mg ml^{-1} BSA. The reaction was initiated at 30 °C by adding 10 nM LpxD or 100 nM LpxA to the mixture, and time points were taken by spotting 2 µL of the mixture onto a silica gel 60 TLC plate (EMD Chemicals, Germany). The plate was developed with chloroform/methanol/water/acetic acid (25:15:4:2, v:v:v:v) and analyzed with a Phosphor Imager.

3.4.6 Crystallization and structure determination of LpxA:*holo*-ACP

Purified His$_6$-LpxA and *holo*-ACP were mixed in various molar ratios (1:1 and 1:3, LpxA:*holo*-ACP) and incubated at 0-4 °C to preform the protein:protein complex prior to crystallization trials. Crystallization experiments were carried out using the sitting-drop vapor diffusion method in 96 well Intelliplates (Art Robbins Instruments, CA) and a Phoenix crystallization robotic system (Art Robbins Instruments, CA) to screen the protein complex against several commercially available screens (Qiagen, CA and Hampton Research, CA). 1 µL sitting drops, containing 1:1, or 1:1.5 v:v ratios of protein to crystallant solution were allowed to equilibrate against 71 µL of crystallant solution at 15 °C and/or 20 °C using the Minstrel HT Incubator Gallery system and

Autoimaging robotics platform (Rigaku, TX). Initial crystallization condition hit consisted of 0.1 M HEPES, pH 7.0, and 40 % (v/v) 2-Methyl-2,4-pentanediol (MPD) was identified from MPD suite (Qiagen, CA) at 15 °C. The crystals were reproduced using the LpxA:*holo*-ACP protein solution (His6-LpxA and *holo*-ACP 9.5 mg ml^{-1}) mixed in equal volume with the crystallant solution at 15 °C . Crystals reached full size in 14 days, and were cryo-protected by adding 2 μL of the crystallant solution to the crystallization drop, and immediately cryo-cooled to −180 °C in liquid nitrogen.

X-ray diffraction data (λ = 1.0 Å) were collected on the SER-CAT 22-BM beamline at the Advanced Photon Source at Argonne National Laboratory. Data were indexed and scaled using the HKL2000 software suite (127) (Table 3.1). The data for LpxA:*holo*-ACP complexes were processed to 2.1 Å, and the structure was solved by molecular replacement using the program PHASER within the PHENIX software suite (128, 129) and the uncomplexed *E. coli* LpxA structure (PDB code: 2AQ9) as the search model. One monomer of His$_6$-LpxA was present in the asymmetric unit. Since ACP was omitted during the molecular replacement process, it was built manually by first rigid-fitting the *E. coli holo*-ACP coordinates (PDB code: 4IHH) (144) into unbiased, contiguous $F_o - F_c$ difference electron density. The model was rebuilt using COOT (131) and iterative structure refinement was carried out using PHENIX (128). Hydrogens were added to the model and refinement was performed with restrained and TLS options, as well as automated optimization of X-ray/stereochemistry and ADP weights selected.

All residues of LpxA (1-262) and residues 2-75 of ACP were modeled. Six additional residues (His_5-Gly) forming a key lattice contact with the neighboring molecule of ACP were also modeled at the N-terminal end of LpxA. A pronounced electron density was observed attached to Ser36 of ACP, which corresponded to the 4′-phosphate group of 4′-phosphopantetheine prosthetic arm. The electron density of the remaining part of 4′-phosphopantetheine was poor and thus the pantetheine moiety was not included in the final model. This implicates conformational heterogeneity of the pantetheine arm throughout the lattice. The overall B-values for the ACP were approximately 2-fold higher than LpxA (Table 3.1, Fig. 3.3).

The final refined model of LpxA:*holo*-ACP complex had R_{work} and R_{free} values of 18.8 and 22.4, respectively. The protein–protein interactions were specified by AREAIMOL calculations within the CCP4 suite (134). The quality of the final model was evaluated using MOLPROBITY server (135), which reported 97.3 % of the residues in the Ramachandran favored regions and 0.0 % in the disallowed regions. The data collection and refinement statistics are summarized in Table 3.1. Molecular figures were generated using PyMOL (136).

Chapter 4. Conclusion and Future Directions

Understanding the transient involvement of ACP in important cellular processes, such fatty acid, phospholipid, and lipid A biosynthesis, is fundamental to primary and secondary metabolism. There are a number of intriguing questions concerning ACP-based interactions that have long puzzled the scientific community, which have not been previously addressed due to the transient nature of ACP-partner complexes, and the high conformational mobility of many ACP domains. Some of these key questions include: i) the detailed molecular basis for recognition of ACP by its multiple partners which leads to complex formation, and how such complexes can be at once specific and temporary; ii) the role of the phosphopantetheine prosthetic group in substrate delivery, and its contribution to both the formation and dissociation of the ACP-based complexes; iii) the way in which the associations between the ACP and its partners are ultimately broken; iv) the detailed molecular view of ACP tied to an overall catalytic cycle; v) how ACP communicates with representative partner enzymes; and vi) the mechanism by which the acyl-substrate is ejected from the hydrophobic core of ACP in order to interact with its partner. Insights into these questions will not only allow us to understand a fundamental aspect of primary metabolism, but they have relevance to elucidating how similar ACP-based communication occurs in the numerous biosynthetic pathways that are of therapeutic value.

ACP delivers the acyl-chains that get incorporated into the glucosamine sugar of lipid A by the essential acyltransferases of the Raetz Pathway, including LpxA and LpxD (5). The biochemical machinery required for the constitutive synthesis of lipid A is a highly conserved process, as lipid A is an essential anchor of lipopolysaccharides (LPS) to the cell envelope of Gram-negative bacteria (4). This glucosamine-based saccharolipid represents one of the most conserved microbial structures that are required for the growth and survival of this class of microorganisms, with few exceptions (4, 13, 14). The endotoxic lipid A molecules are recognized by the TLR4/MD2 receptor during an infection. Although this is desirable for clearing infections, overproduction of pro-inflammatory cytokines inundates the host immune system potentiating the sepsis pathology (4). Thus, lipid A biosynthesis not only provides an ideal model system to glean structural knowledge of ACP-based complexes but also offers an appealing target for developing novel antibiotics against infective bacteria.

The structural and biochemical studies presented in Chapter 2 make a substantial contribution to resolving the questions concerning ACP-based interactions, namely those labeled i-v, for the interaction between a representative bacterial ACP from *E. coli* and one of its enzymatic partners, the *N*-acyltransferase LpxD from lipid A biosynthesis pathway. Our study represents the first to have captured several stalled complexes of ACP along its acyl-delivery reaction coordinate: *intact-acyl*-ACP, *hydrolysed-acyl*-ACP, and *holo*-ACP. Moreover, these structures are the first to show ACP engaging LpxD, or any acyltransferase for that matter, which are the single most abundant class of partner enzymes that associate with carrier-protein (56).

The ACP complexes revealed the stoichiometry of ACP binding to LpxD, and the amino acid residues on both partners that form the interaction interface. The interaction with ACP takes place on the C-terminal end of LpxD, and is predominantly of hydrophilic character. Three electropositive patches on the C-terminal helices of LpxD bind three molecules of ACP, and orient the phosphopantetheinylated serine residue relative to the active site of LpxD. The *intact*- and *hydrolysed-acyl*-ACP revealed the 4′-phosphopantetheine disengages from ACP to bury the acyl-chain inside a hydrophobic pocket, termed the *N*-channel, which is located between two adjacent LβH domains of LpxD. This conformation corroborated the previously proposed catalytic mechanism that was deduced from mutagenesis studies, and also revealed the molecular basis for the specificity of LpxD for 14-carbon chains containing a β-hydroxyl group, and the role of Met290 as a hydrocarbon ruler. Fortuitously, an additional fatty acid was observed bound to the surface of LpxD, which likely represents the *O*-channel that binds the acyl-chain of the UDP-*O*-acyl-GlcN. Determining the structure of LpxD in complex with UDP-*O*-acyl-GlcN will complete the “molecular landscape” of the active site that will facilitate the design and optimization of compounds for developing novel antibiotics against infective bacteria.

ACP binding to LpxD is unusually tight (K_d = 59 nM) (110), which suggests a 'molecular trigger' is required to initiate the collapse of protein–protein interactions following acyl-delivery (117). Moreover, the 4′-phosphopantetheine closes off the *N*-channel and raises a key question as to how the lipid product of LpxD reaction, UDP-2,3-diacyl-GlcN, is able to dissociate from the enzyme prior to *holo*-ACP as inferred by kinetic studies (110). Comparison of the *intact-acyl*- and *holo*-ACP structures shed light on this matter and revealed that the liberated 4′-PPT group of the *holo*-ACP is able to form new interactions at the far end of the *N*-channel, which necessitates a 15 Å displacement of the thiol end of the arm. This movement has several consequences. Firstly, it opens the catalytic chamber to solvent, allowing the product UDP-2,3-diacyl-GlcN to leave the active site prior to the ACP domain, in accordance with the ordered catalytic mechanism. Product exit is apparently aided by a steric clash between the newly-positioned terminal thiol and the acyl-chain. And finally, the 4′-PPT motion provokes a substantial conformational change in the ACP domain, downstream of the recognition helix II. This structural shift breaks the electrostatic contacts of 'region II' with LpxD, a loss which is likely responsible for the dissociation of the ACP domain. Thus, the catalytic mechanism of LpxD has been shown to depend strongly on the presence of the ACP domain, exploiting both the chemical nature and mobility of the prosthetic group, and the dynamic character of the protein.

Chapter 3 reports another example of *holo*-ACP bound to LpxA acyltransferase, which also contains a similar LβH core. The structure revealed the stoichiometry of ACP binding, and the identity of residues that contribute to ACP recognition. Three ACP molecules utilize a binding mode different from the *holo*-ACP:LpxD complex to complement electropositive patches presented by the C-terminal helices of LpxA trimer. This structural study revealed that the functional role of the C-terminal domain of LpxA is 2-fold: ACP recognition and UDP-GlcNAc binding. The structural comparison of LpxA with LpxD shows how their variation of domain construction at the N- and C-termini allows them to acylate the glucosamine ring at a specific site. LpxA adds an acyl-chain to the 3-hydroxy group, whereas LpxD transfers an acyl-chain to the 2-amino group of the glucosamine ring. By adopting a rather extended conformation, the C-terminal helices of LpxD untie themselves from UDP binding, and alternatively the N-terminal globular domain, which has no counterpart in LpxA, takes over this role to orient the glucosamine ring such that *N*-acyltransfer takes place.

Targeting enzymes within the Raetz pathway of lipid A biosynthesis represents an important therapeutic approach for the development of novel antibiotics. All of the structural insights gleaned from Chapter 2 and 3 will feed into our global effort in discovering antibiotics that target lipid A biosynthesis. Recently, Jenkins *et*. *al*. reported a high-throughput fluorescence polarization binding assay for LpxA and LpxD acyltransferases, which utilizes fluorescein-labeled peptides known to bind to these enzymes by competing with *acyl*-ACP (145). This competitive binding assay can be utilized to screen for compounds that reduce the fluorescence polarization through binding to LpxA or LpxD and displacing the labeled peptide. Candidate inhibitors can be further characterized by our established radioactivity-based assay, and fed into crystallization trials for the iterative process of compound evaluation and optimization.

To complete our structural knowledge of ACP-mediated acyl delivery in lipid A biosynthesis, it is our vision that similar structural studies could be performed with the remaining two acyltransferase, LpxL and LpxM, whose structures are unknown. LpxL and –M are integral membrane enzymes that display a significant sequence homology to each other but not to LpxA or LpxD (5). Solving the structure of LpxL and LpxM with ACP at different stages of catalysis is important not only for understanding the mechanism of acyl-chain delivery by ACP, but also for expanding our limited structural knowledge of membrane-bound enzymes.

Bibliography

1. Nikaido H (2003) Molecular basis of bacterial outer membrane permeability revisited. *Microbiol Mol Biol Rev* 67(4):593-656.

2. Papo N & Shai Y (2005) A molecular mechanism for lipopolysaccharide protection of Gram-negative bacteria from antimicrobial peptides. *J Biol Chem* 280(11):10378-10387.

3. Sutcliffe IC (2010) A phylum level perspective on bacterial cell envelope architecture. *Trends Microbiol* 18(10):464-470.

4. Raetz CRH & Whitfield C (2002) Lipopolysaccharide endotoxins. *Annu Rev Biochem* 71:635-700.

5. Raetz CRH, Reynolds CM, Trent MS, & Bishop RE (2007) Lipid A modification systems in gram-negative bacteria. *Annu Rev Biochem* 76:295-329.

6. Stenutz R, Weintraub A, & Widmalm G (2006) The structures of Escherichia coli O-polysaccharide antigens. *FEMS Microbiol Rev* 30(3):382-403.

7. Vorachek-Warren MK, Ramirez S, Cotter RJ, & Raetz CRH (2002) A triple mutant of Escherichia coli lacking secondary acyl chains on lipid A. *J Biol Chem* 277(16):14194-14205.

8. Reynolds CM & Raetz CRH (2009) Replacement of lipopolysaccharide with free lipid A molecules in Escherichia coli mutants lacking all core sugars. *Biochemistry* 48(40):9627-9640.

9. Weiser JN, Love JM, & Moxon ER (1989) The molecular mechanism of phase variation of H. influenzae lipopolysaccharide. *Cell* 59(4):657-665.

10. Ames GF, Spudich EN, & Nikaido H (1974) Protein composition of the outer membrane of Salmonella typhimurium: effect of lipopolysaccharide mutations. *J Bacteriol* 117(2):406-416.

11. Koplow J & Goldfine H (1974) Alterations in the outer membrane of the cell envelope of heptose-deficient mutants of Escherichia coli. *J Bacteriol* 117(2):527-543.

12. Tran AX, Lester ME, Stead CM, Raetz CRH, Maskell DJ, McGrath SC, Cotter RJ, & Trent MS (2005) Resistance to the antimicrobial peptide polymyxin requires myristoylation of Escherichia coli and Salmonella typhimurium lipid A. *J Biol Chem* 280(31):28186-28194.

13. Steeghs L, den Hartog R, den Boer A, Zomer B, Roholl P, & van der Ley P (1998) Meningitis bacterium is viable without endotoxin. *Nature* 392(6675):449-450.

14. Vinogradov E, Perry MB, & Conlan JW (2002) Structural analysis of Francisella tularensis lipopolysaccharide. *Eur J Biochem* 269(24):6112-6118.

15. Wang XY, Ribeiro AA, Guan ZQ, McGrath SC, Cotter RJ, & Raetz CRHH (2006) Structure and biosynthesis of free lipid A molecules that replace lipopolysaccharide in Francisella tularensis subsp novicida. *Biochemistry* 45(48):14427-14440.

16. Takeda K (2009) The lipid A receptor. *Adv Exp Med Biol* 667:53-58.

17. Andra J, Gutsmann T, Muller M, & Schromm AB (2009) Interactions between Lipid A and Serum Proteins. *Lipid a in Cancer Therapy* 667:39-51.

18. Gangloff M & Gay NJ (2004) MD-2: the Toll 'gatekeeper' in endotoxin signalling. *Trends Biochem Sci* 29(6):294-300.

19. Bryant CE, Spring DR, Gangloff M, & Gay NJ (2010) The molecular basis of the host response to lipopolysaccharide. *Nat Rev Microbiol* 8(1):8-14.

20. Park BS, Song DH, Kim HM, Choi BS, Lee H, & Lee JO (2009) The structural basis of lipopolysaccharide recognition by the TLR4-MD-2 complex. *Nature* 458(7242):1191-U1130.

21. O'Neill LAJ & Bowie AG (2007) The family of five: TIR-domain-containing adaptors in Toll-like receptor signalling. *Nat Rev Immunol* 7(5):353-364.

22. Le Bon A & Tough DF (2002) Links between innate and adaptive immunity via type I interferon. *Curr Opin Immunol* 14(4):432-436.

23. Arvidsson S, Falt K, & Haglund U (1984) Acute gastric mucosal ulceration in septic shock. An experimental study on pathogenic mechanisms. *Acta Chir Scand* 150(7):541-547.

24. Kong Q, Six DA, Liu Q, Gu L, Roland KL, Raetz CRH, & Curtiss R, 3rd (2011) Palmitoylation state impacts induction of innate and acquired immunity by the Salmonella enterica serovar typhimurium msbB mutant. *Infect Immun* 79(12):5027-5038.

25. Kong Q, Six DA, Liu Q, Gu L, Wang S, Alamuri P, Raetz CRH, & Curtiss R, 3rd (2012) Phosphate groups of lipid A are essential for Salmonella enterica serovar Typhimurium virulence and affect innate and adaptive immunity. *Infect Immun* 80(9):3215-3224.

26. Hajjar AM, Ernst RK, Tsai JH, Wilson CB, & Miller SI (2002) Human Toll-like receptor 4 recognizes host-specific LPS modifications. *Nat Immunol* 3(4):354-359.

27. Saitoh S, Akashi S, Yamada T, Tanimura N, Kobayashi M, Konno K, Matsumoto F, Fukase K, Kusumoto S, Nagai Y, Kusumoto Y, Kosugi A, & Miyake K (2004) Lipid A antagonist, lipid IVa, is distinct from lipid A in interaction with Toll-like receptor 4 (TLR4)-MD-2 and ligand-induced TLR4 oligomerization. *Int Immunol* 16(7):961-969.

28. Mata-Haro V (2007) The vaccine adjuvant monophosphoryl lipid A as a TRIF-biased agonist of TLR4 (June, pg 1628, 2007). *Science* 317(5841):1036-1036.

29. Vacchelli E, Galluzzi L, Eggermont A, Fridman WH, Galon J, Sautes-Fridman C, Tartour E, Zitvogel L, & Kroemer G (2012) Trial watch FDA-approved Toll-like receptor agonists for cancer therapy. *Oncoimmunology* 1(6):894-907.

30. Albrecht SJ, Fishman NO, Kitchen J, Nachamkin I, Bilker WB, Hoegg C, Samel C, Barbagallo S, Arentzen J, & Lautenbach E (2006) Reemergence of gram-negative health care-associated bloodstream infections. *Arch Intern Med* 166(12):1289-1294.

31. Nicasio AM, Kuti JL, & Nicolau DP (2008) The current state of multidrug-resistant gram-negative bacilli in North America. *Pharmacotherapy* 28(2):235-249.

32. Spellberg B, Guidos R, Gilbert D, Bradley J, Boucher HW, Scheld WM, Bartlett JG, & Edwards J, Jr. (2008) The epidemic of antibiotic-resistant infections: a call to action for the medical community from the Infectious Diseases Society of America. *Clin Infect Dis* 46(2):155-164.

33. Walsh C (2003) Where will new antibiotics come from? *Nature reviews. Microbiology* 1(1):65-70.

34. Anderson MS, Bull HG, Galloway SM, Kelly TM, Mohan S, Radika K, & Raetz CRH (1993) UDP-N-acetylglucosamine acyltransferase of Escherichia coli. The first step of endotoxin biosynthesis is thermodynamically unfavorable. *J Biol Chem* 268(26):19858-19865.

35. Jackman JE, Raetz CRHH, & Fierke CA (1999) UDP-3-O-(R-3-hydroxymyristoyl)-N-acetylglucosamine deacetylase of Escherichia coli is a zinc metalloenzyme. *Biochemistry* 38(6):1902-1911.

36. Kelly TM, Stachula SA, Raetz CRH, & Anderson MS (1993) The firA gene of Escherichia coli encodes UDP-3-O-(R-3-hydroxymyristoyl)-glucosamine N-acyltransferase. The third step of endotoxin biosynthesis. *J Biol Chem* 268(26):19866-19874.

37. Raetz CRH & Roderick SL (1995) A left-handed parallel beta helix in the structure of UDP-N-acetylglucosamine acyltransferase. *Science* 270(5238):997-1000.

38. Whittington DA, Rusche KM, Shin H, Fierke CA, & Christianson DW (2003) Crystal structure of LpxC, a zinc-dependent deacetylase essential for endotoxin biosynthesis. *P Natl Acad Sci USA* 100(14):8146-8150.

39. Bartling CM & Raetz CRH (2009) Crystal structure and acyl chain selectivity of Escherichia coli LpxD, the N-acyltransferase of lipid A biosynthesis. *Biochemistry* 48(36):8672-8683.

40. Babinski KJ, Ribeiro AA, & Raetz CRH (2002) The Escherichia coli gene encoding the UDP-2,3-diacylglucosamine pyrophosphatase of lipid A biosynthesis. *J Biol Chem* 277(29):25937-25946.

41. Crowell DN, Anderson MS, & Raetz CRH (1986) Molecular cloning of the genes for lipid A disaccharide synthase and UDP-N-acetylglucosamine acyltransferase in Escherichia coli. *J Bacteriol* 168(1):152-159.

42. Garrett TA, Kadrmas JL, & Raetz CRH (1997) Identification of the gene encoding the Escherichia coli lipid A 4'-kinase. Facile phosphorylation of endotoxin analogs with recombinant LpxK. *J Biol Chem* 272(35):21855-21864.

43. Clementz T & Raetz CRH (1991) A gene coding for 3-deoxy-D-manno-octulosonic-acid transferase in Escherichia coli. Identification, mapping, cloning, and sequencing. *J Biol Chem* 266(15):9687-9696.

44. Clementz T, Bednarski JJ, & Raetz CRH (1996) Function of the htrB high temperature requirement gene of Escherchia coli in the acylation of lipid A: HtrB catalyzed incorporation of laurate. *J Biol Chem* 271(20):12095-12102.

45. Karow M & Georgopoulos C (1992) Isolation and characterization of the Escherichia coli msbB gene, a multicopy suppressor of null mutations in the high-temperature requirement gene htrB. *J Bacteriol* 174(3):702-710.

46. Whitfield C, Kaniuk N, & Frirdich E (2003) Molecular insights into the assembly and diversity of the outer core oligosaccharide in lipopolysaccharides from Escherichia coli and Salmonella. *J Endotoxin Res* 9(4):244-249.

47. Doerrler WT, Gibbons HS, & Raetz CRHH (2004) MsbA-dependent translocation of lipids across the inner membrane of Escherichia coli. *Journal of Biological Chemistry* 279(43):45102-45109.

48. Samuel G & Reeves P (2003) Biosynthesis of O-antigens: genes and pathways involved in nucleotide sugar precursor synthesis and O-antigen assembly. *Carbohyd Res* 338(23):2503-2519.

49. Bowyer A, Baardsnes J, Ajamian E, Zhang LH, & Cygler M (2011) Characterization of interactions between LPS transport proteins of the Lpt system. *Biochem Bioph Res Co* 404(4):1093-1098.

50. Crosby J & Crump MP (2012) The structural role of the carrier protein--active controller or passive carrier. *Nat Prod Rep* 29(10):1111-1137.

51. Lambalot RH & Walsh CT (1995) Cloning, overproduction, and characterization of the Escherichia coli holo-acyl carrier protein synthase. *J Biol Chem* 270(42):24658-24661.

52. Chan DI & Vogel HJ (2010) Current understanding of fatty acid biosynthesis and the acyl carrier protein. *Biochem J* 430(1):1-19.

53. Maier T, Leibundgut M, & Ban N (2008) The crystal structure of a mammalian fatty acid synthase. *Science* 321(5894):1315-1322.

54. Jenni S, Leibundgut M, Maier T, & Ban N (2006) Architecture of a fungal fatty acid synthase at 5 A resolution. *Science* 311(5765):1263-1267.

55. Gago G, Diacovich L, Arabolaza A, Tsai SC, & Gramajo H (2011) Fatty acid biosynthesis in actinomycetes. *FEMS Microbiol Rev* 35(3):475-497.

56. Byers DM & Gong H (2007) Acyl carrier protein: structure-function relationships in a conserved multifunctional protein family. *Biochem Cell Biol* 85(6):649-662.

57. Maier T, Jenni S, & Ban N (2006) Architecture of mammalian fatty acid synthase at 4.5 A resolution. *Science* 311(5765):1258-1262.

58. White SW, Zheng J, Zhang YM, & Rock (2005) The structural biology of type II fatty acid biosynthesis. *Annu Rev Biochem* 74:791-831.

59. Rock CO & Jackowski S (1982) Regulation of phospholipid synthesis in Escherichia coli. Composition of the acyl-acyl carrier protein pool in vivo. *J Biol Chem* 257(18):10759-10765.

60. Shen B, Summers RG, Gramajo H, Bibb MJ, & Hutchinson CR (1992) Purification and characterization of the acyl carrier protein of the Streptomyces glaucescens tetracenomycin C polyketide synthase. *J Bacteriol* 174(11):3818-3821.

61. Stein T, Vater J, Kruft V, Otto A, Wittmann-Liebold B, Franke P, Panico M, McDowell R, & Morris HR (1996) The multiple carrier model of nonribosomal peptide biosynthesis at modular multienzymatic templates. *J Biol Chem* 271(26):15428-15435.

62. Anderson MS & Raetz CRH (1987) Biosynthesis of lipid A precursors in Escherichia coli. A cytoplasmic acyltransferase that converts UDP-N-acetylglucosamine to UDP-3-O-(R-3-hydroxymyristoyl)-N-acetylglucosamine. *J Biol Chem* 262(11):5159-5169.

63. Schaefer AL, Val DL, Hanzelka BL, Cronan JE, Jr., & Greenberg EP (1996) Generation of cell-to-cell signals in quorum sensing: acyl homoserine lactone synthase activity of a purified Vibrio fischeri LuxI protein. *Proc Natl Acad Sci U S A* 93(18):9505-9509.

64. Jordan SW & Cronan JE, Jr. (1997) A new metabolic link. The acyl carrier protein of lipid synthesis donates lipoic acid to the pyruvate dehydrogenase complex in Escherichia coli and mitochondria. *J Biol Chem* 272(29):17903-17906.

65. Issartel JP, Koronakis V, & Hughes C (1991) Activation of Escherichia coli prohaemolysin to the mature toxin by acyl carrier protein-dependent fatty acylation. *Nature* 351(6329):759-761.

66. Rumley MK, Therisod H, Weissborn AC, & Kennedy EP (1992) Mechanisms of regulation of the biosynthesis of membrane-derived oligosaccharides in Escherichia coli. *J Biol Chem* 267(17):11806-11810.

67. Butland G, Peregrin-Alvarez JM, Li J, Yang W, Yang X, Canadien V, Starostine A, Richards D, Beattie B, Krogan N, Davey M, Parkinson J, Greenblatt J, & Emili A (2005) Interaction network containing conserved and essential protein complexes in Escherichia coli. *Nature* 433(7025):531-537.

68. Holak TA, Nilges M, Prestegard JH, Gronenborn AM, & Clore GM (1988) Three-dimensional structure of acyl carrier protein in solution determined by nuclear magnetic resonance and the combined use of dynamical simulated annealing and distance geometry. *European journal of biochemistry / FEBS* 175(1):9-15.

69. Roujeinikova A, Baldock C, Simon WJ, Gilroy J, Baker PJ, Stuitje AR, Rice DW, Slabas AR, & Rafferty JB (2002) X-ray crystallographic studies on butyryl-ACP reveal flexibility of the structure around a putative acyl chain binding site. *Structure* 10(6):825-835.

70. Ploskon E, Arthur CJ, Evans SE, Williams C, Crosby J, Simpson TJ, & Crump MP (2008) A mammalian type I fatty acid synthase acyl carrier protein domain does not sequester acyl chains. *J Biol Chem* 283(1):518-528.

71. Bunkoczi G, Pasta S, Joshi A, Wu X, Kavanagh KL, Smith S, & Oppermann U (2007) Mechanism and substrate recognition of human holo ACP synthase. *Chem Biol* 14(11):1243-1253.

72. Leibundgut M, Jenni S, Frick C, & Ban N (2007) Structural basis for substrate delivery by acyl carrier protein in the yeast fatty acid synthase. *Science* 316(5822):288-290.

73. Perez DR & Wider G (2009) 1H, 15N, 13C resonance assignment of the acyl carrier protein subunit of the Saccharomyces cerevisiae fatty acid synthase. *Biomol NMR Assign* 3(1):133-136.

74. Roujeinikova A, Simon WJ, Gilroy J, Rice DW, Rafferty JB, & Slabas AR (2007) Structural studies of fatty acyl-(acyl carrier protein) thioesters reveal a hydrophobic binding cavity that can expand to fit longer substrates. *J Mol Biol* 365(1):135-145.

75. Rock CO & Cronan JE, Jr. (1979) Re-evaluation of the solution structure of acyl carrier protein. *J Biol Chem* 254(19):9778-9785.

76. Tener DM & Mayo KH (1990) Divalent cation binding to reduced and octanoyl acyl-carrier protein. *European journal of biochemistry / FEBS* 189(3):559-565.

77. Frederick AF, Kay LE, & Prestegard JH (1988) Location of divalent ion sites in acyl carrier protein using relaxation perturbed 2D NMR. *FEBS Lett* 238(1):43-48.

78. Keating MM, Gong H, & Byers DM (2002) Identification of a key residue in the conformational stability of acyl carrier protein. *Biochim Biophys Acta* 1601(2):208-214.

79. Gong H, Murphy A, McMaster CR, & Byers DM (2007) Neutralization of acidic residues in helix II stabilizes the folded conformation of acyl carrier protein and variably alters its function with different enzymes. *J Biol Chem* 282(7):4494-4503.

80. Zhang YM, Wu B, Zheng J, & Rock CO (2003) Key residues responsible for acyl carrier protein and beta-ketoacyl-acyl carrier protein reductase (FabG) interaction. *J Biol Chem* 278(52):52935-52943.

81. Zhang YM, Rao MS, Heath RJ, Price AC, Olson AJ, Rock CO, & White SW (2001) Identification and analysis of the acyl carrier protein (ACP) docking site on beta-ketoacyl-ACP synthase III. *J Biol Chem* 276(11):8231-8238.

82. Arthur CJ, Williams C, Pottage K, Ploskon E, Findlow SC, Burston SG, Simpson TJ, Crump MP, & Crosby J (2009) Structure and malonyl CoA-ACP transacylase binding of streptomyces coelicolor fatty acid synthase acyl carrier protein. *ACS Chem Biol* 4(8):625-636.

83. Worsham LM, Earls L, Jolly C, Langston KG, Trent MS, & Ernst-Fonberg ML (2003) Amino acid residues of Escherichia coli acyl carrier protein involved in heterologous protein interactions. *Biochemistry* 42(1):167-176.

84. Gong H & Byers DM (2003) Glutamate-41 of Vibrio harveyi acyl carrier protein is essential for fatty acid synthase but not acyl-ACP synthetase activity. *Biochem Biophys Res Commun* 302(1):35-40.

85. Rafi S, Novichenok P, Kolappan S, Zhang X, Stratton CF, Rawat R, Kisker C, Simmerling C, & Tonge PJ (2006) Structure of acyl carrier protein bound to FabI, the FASII enoyl reductase from Escherichia coli. *J Biol Chem* 281(51):39285-39293.

86. Parris KD, Lin L, Tam A, Mathew R, Hixon J, Stahl M, Fritz CC, Seehra J, & Somers WS (2000) Crystal structures of substrate binding to Bacillus subtilis holo-(acyl carrier protein) synthase reveal a novel trimeric arrangement of molecules resulting in three active sites. *Structure* 8(8):883-895.

87. Cryle MJ & Schlichting I (2008) Structural insights from a P450 Carrier Protein complex reveal how specificity is achieved in the P450(BioI) ACP complex. *P Natl Acad Sci USA* 105(41):15696-15701.

88. Nguyen C, Haushalter RW, Lee DJ, Markwick PR, Bruegger J, Caldara-Festin G, Finzel K, Jackson DR, Ishikawa F, O'Dowd B, McCammon JA, Opella SJ, Tsai SC, & Burkart MD (2014) Trapping the dynamic acyl carrier protein in fatty acid biosynthesis. *Nature* 505(7483):427-431.

89. Ploskon E, Arthur CJ, Kanari AL, Wattana-amorn P, Williams C, Crosby J, Simpson TJ, Willis CL, & Crump MP (2010) Recognition of intermediate functionality by acyl carrier protein over a complete cycle of fatty acid biosynthesis. *Chem Biol* 17(7):776-785.

90. Vaara M (1992) Eight bacterial proteins, including UDP-N-acetylglucosamine acyltransferase (LpxA) and three other transferases of Escherichia coli, consist of a six-residue periodicity theme. *FEMS Microbiol Lett* 76(3):249-254.

91. Brown K, Pompeo F, Dixon S, Mengin-Lecreulx D, Cambillau C, & Bourne Y (1999) Crystal structure of the bifunctional N-acetylglucosamine 1-phosphate uridyltransferase from Escherichia coli: a paradigm for the related pyrophosphorylase superfamily. *Embo J* 18(15):4096-4107.

92. Wang XG, Olsen LR, & Roderick SL (2002) Structure of the lac operon galactoside acetyltransferase. *Structure* 10(4):581-588.

93. Beaman TW, Blanchard JS, & Roderick SL (1998) The conformational change and active site structure of tetrahydrodipicolinate N-succinyltransferase. *Biochemistry* 37(29):10363-10369.

94. Beaman TW, Sugantino M, & Roderick SL (1998) Structure of the hexapeptide xenobiotic acetyltransferase from Pseudomonas aeruginosa. *Biochemistry* 37(19):6689-6696.

95. Olsen LR, Huang B, Vetting MW, & Roderick SL (2004) Structure of serine acetyltransferase in complexes with CoA and its cysteine feedback inhibitor. *Biochemistry* 43(20):6013-6019.

96. Sugantino M & Roderick SL (2002) Crystal structure of Vat(D): an acetyltransferase that inactivates streptogramin group A antibiotics. *Biochemistry* 41(7):2209-2216.

97. Kisker C, Schindelin H, Alber BE, Ferry JG, & Rees DC (1996) A left-hand beta-helix revealed by the crystal structure of a carbonic anhydrase from the archaeon Methanosarcina thermophila. *Embo J* 15(10):2323-2330.

98. Ning B & Elbein AD (2000) Cloning, expression and characterization of the pig liver GDP-mannose pyrophosphorylase. Evidence that GDP-mannose and GDP-Glc pyrophosphorylases are different proteins. *Eur J Biochem* 267(23):6866-6874.

99. Wyckoff TJ & Raetz CRH (1999) The active site of Escherichia coli UDP-N-acetylglucosamine acyltransferase. Chemical modification and site-directed mutagenesis. *J Biol Chem* 274(38):27047-27055.

100. Ulaganathan V, Buetow L, & Hunter WN (2007) Nucleotide substrate recognition by UDP-N-acetylglucosamine acyltransferase (LpxA) in the first step of lipid A biosynthesis. *J Mol Biol* 369(2):305-312.

101. Dotson GD, Kaltashov IA, Cotter RJ, & Raetz CRH (1998) Expression cloning of a Pseudomonas gene encoding a hydroxydecanoyl-acyl carrier protein-dependent UDP-GlcNAc acyltransferase. *J Bacteriol* 180(2):330-337.

102. Sweet CR, Williams AH, Karbarz MJ, Werts C, Kalb SR, Cotter RJ, & Raetz CRH (2004) Enzymatic synthesis of lipid A molecules with four amide-linked acyl chains. LpxA acyltransferases selective for an analog of UDP-N-acetylglucosamine in which an amine replaces the 3"-hydroxyl group. *J Biol Chem* 279(24):25411-25419.

103. Wyckoff TJ, Lin S, Cotter RJ, Dotson GD, & Raetz CRH (1998) Hydrocarbon rulers in UDP-N-acetylglucosamine acyltransferases. *J Biol Chem* 273(49):32369-32372.

104. Williams AH & Raetz CRH (2007) Structural basis for the acyl chain selectivity and mechanism of UDP-N-acetylglucosamine acyltransferase. *P Natl Acad Sci USA* 104(34):13543-13550.

105. Robins LI, Williams AH, & Raetz CRH (2009) Structural basis for the sugar nucleotide and acyl-chain selectivity of Leptospira interrogans LpxA. *Biochemistry* 48(26):6191-6201.

106. Sweet CR, Lin S, Cotter RJ, & Raetz CRH (2001) A Chlamydia trachomatis UDP-N-acetylglucosamine acyltransferase selective for myristoyl-acyl carrier protein. Expression in Escherichia coli and formation of hybrid lipid A species. *J Biol Chem* 276(22):19565-19574.

107. Jain NU, Wyckoff TJ, Raetz CRH, & Prestegard JH (2004) Rapid analysis of large protein-protein complexes using NMR-derived orientational constraints: the 95 kDa complex of LpxA with acyl carrier protein. *J Mol Biol* 343(5):1379-1389.

108. Williams AH, Immormino RM, Gewirth DT, & Raetz CRH (2006) Structure of UDP-N-acetylglucosamine acyltransferase with a bound antibacterial pentadecapeptide. *P Natl Acad Sci USA* 103(29):10877-10882.

109. Benson RE, Gottlin EB, Christensen DJ, & Hamilton PT (2003) Intracellular expression of Peptide fusions for demonstration of protein essentiality in bacteria. *Antimicrob Agents Chemother* 47(9):2875-2881.

110. Bartling CM & Raetz CRH (2008) Steady-state kinetics and mechanism of LpxD, the N-acyltransferase of lipid A biosynthesis. *Biochemistry* 47(19):5290-5302.

111. Buetow L, Smith TK, Dawson A, Fyffe S, & Hunter WN (2007) Structure and reactivity of LpxD, the N-acyltransferase of lipid A biosynthesis. *P Natl Acad Sci USA* 104(11):4321-4326.

112. Galloway SM & Raetz CRH (1990) A mutant of Escherichia coli defective in the first step of endotoxin biosynthesis. *J Biol Chem* 265(11):6394-6402.

113. Belunis CJ, Clementz T, Carty SM, & Raetz CRH (1995) Inhibition of lipopolysaccharide biosynthesis and cell growth following inactivation of the kdtA gene in Escherichia coli. *J Biol Chem* 270(46):27646-27652.

114. Poltorak A, He X, Smirnova I, Liu MY, Van Huffel C, Du X, Birdwell D, Alejos E, Silva M, Galanos C, Freudenberg M, Ricciardi-Castagnoli P, Layton B, & Beutler B (1998) Defective LPS signaling in C3H/HeJ and C57BL/10ScCr mice: mutations in Tlr4 gene. *Science* 282(5396):2085-2088.

115. Akira S, Uematsu S, & Takeuchi O (2006) Pathogen recognition and innate immunity. *Cell* 124(4):783-801.

116. Onishi HR, Pelak BA, Gerckens LS, Silver LL, Kahan FM, Chen MH, Patchett AA, Galloway SM, Hyland SA, Anderson MS, & Raetz CRH (1996) Antibacterial agents that inhibit lipid A biosynthesis. *Science* 274(5289):980-982.

117. Nooren IM & Thornton JM (2003) Diversity of protein-protein interactions. *Embo J* 22(14):3486-3492.

118. Holak TA & Prestegard JH (1986) Secondary structure of acyl carrier protein as derived from two-dimensional 1H NMR spectroscopy. *Biochemistry* 25(19):5766-5774.

119. Kim Y & Prestegard JH (1990) Refinement of the NMR structures for acyl carrier protein with scalar coupling data. *Proteins* 8(4):377-385.

120. Xu GY, Tam A, Lin L, Hixon J, Fritz CC, & Powers R (2001) Solution structure of B. subtilis acyl carrier protein. *Structure* 9(4):277-287.

121. Agarwal V, Lin S, Lukk T, Nair SK, & Cronan JE (2012) Structure of the enzyme-acyl carrier protein (ACP) substrate gatekeeper complex required for biotin synthesis. *P Natl Acad Sci USA* 109(43):17406-17411.

122. Kraut DA, Carroll KS, & Herschlag D (2003) Challenges in enzyme mechanism and energetics. *Annu Rev Biochem* 72:517-571.

123. Babu M, Greenblatt JF, Emili A, Strynadka NC, Reithmeier RA, & Moraes TF (2010) Structure of a SLC26 anion transporter STAS domain in complex with acyl carrier protein: implications for E. coli YchM in fatty acid metabolism. *Structure* 18(11):1450-1462.

124. Miroux B & Walker JE (1996) Over-production of proteins in Escherichia coli: mutant hosts that allow synthesis of some membrane proteins and globular proteins at high levels. *J Mol Biol* 260(3):289-298.

125. Jiang Y, Chan CH, & Cronan JE (2006) The soluble acyl-acyl carrier protein synthetase of Vibrio harveyi B392 is a member of the medium chain acyl-CoA synthetase family. *Biochemistry* 45(33):10008-10019.

126. Rock CO, Cronan JE, Jr., & Armitage IM (1981) Molecular properties of acyl carrier protein derivatives. *J Biol Chem* 256(6):2669-2674.

127. Otwinowski Z & Minor W (1997) Processing of X-ray diffraction data collected in oscillation mode. *Method Enzymol* 276:307-326.

128. Adams PD, Afonine PV, Bunkoczi G, Chen VB, Davis IW, Echols N, Headd JJ, Hung LW, Kapral GJ, Grosse-Kunstleve RW, McCoy AJ, Moriarty NW, Oeffner R, Read RJ, Richardson DC, Richardson JS, Terwilliger TC, & Zwart PH (2010) PHENIX: a comprehensive Python-based system for macromolecular structure solution. *Acta Crystallogr D Biol Crystallogr* 66(Pt 2):213-221.

129. McCoy AJ, Grosse-Kunstleve RW, Adams PD, Winn MD, Storoni LC, & Read RJ (2007) Phaser crystallographic software. *J Appl Crystallogr* 40(Pt 4):658-674.

130. Qiu X & Janson CA (2004) Structure of apo acyl carrier protein and a proposal to engineer protein crystallization through metal ions. *Acta Crystallogr D Biol Crystallogr* 60(Pt 9):1545-1554.

131. Emsley P & Cowtan K (2004) Coot: model-building tools for molecular graphics. *Acta Crystallogr D* 60:2126-2132.

132. Schuttelkopf AW & van Aalten DM (2004) PRODRG: a tool for high-throughput crystallography of protein-ligand complexes. *Acta Crystallogr D Biol Crystallogr* 60(Pt 8):1355-1363.

133. Brunger AT, Adams PD, Clore GM, DeLano WL, Gros P, Grosse-Kunstleve RW, Jiang JS, Kuszewski J, Nilges M, Pannu NS, Read RJ, Rice LM, Simonson T, & Warren GL (1998) Crystallography & NMR system: A new software suite for macromolecular structure determination. *Acta Crystallogr D Biol Crystallogr* 54(Pt 5):905-921.

134. Winn MD, Ballard CC, Cowtan KD, Dodson EJ, Emsley P, Evans PR, Keegan RM, Krissinel EB, Leslie AG, McCoy A, McNicholas SJ, Murshudov GN, Pannu NS, Potterton EA, Powell HR, Read RJ, Vagin A, & Wilson KS (2011) Overview of the CCP4 suite and current developments. *Acta Crystallogr D Biol Crystallogr* 67(Pt 4):235-242.

135. Chen VB, Arendall WB, 3rd, Headd JJ, Keedy DA, Immormino RM, Kapral GJ, Murray LW, Richardson JS, & Richardson DC (2010) MolProbity: all-atom structure validation for macromolecular crystallography. *Acta Crystallogr D Biol Crystallogr* 66(Pt 1):12-21.

136. Schrodinger, LLC (2010) The PyMOL Molecular Graphics System, Version 1.3r1.

137. Stokes GB & Stumpf PK (1974) Fat metabolism in higher plants. The nonenzymatic acylation of dithiothreitol by acyl coenzyme A. *Arch Biochem Biophys* 162(2):638-648.

138. Needham BD & Trent MS (2013) Fortifying the barrier: the impact of lipid A remodelling on bacterial pathogenesis. *Nat Rev Microbiol* 11(7):467-481.

139. Shimazu R, Akashi S, Ogata H, Nagai Y, Fukudome K, Miyake K, & Kimoto M (1999) MD-2, a molecule that confers lipopolysaccharide responsiveness on Toll-like receptor 4. *J Exp Med* 189(11):1777-1782.

140. Croxen MA & Finlay BB (2010) Molecular mechanisms of Escherichia coli pathogenicity. *Nat Rev Microbiol* 8(1):26-38.

141. Miller SI, Ernst RK, & Bader MW (2005) LPS, TLR4 and infectious disease diversity. *Nat Rev Microbiol* 3(1):36-46.

142. Anderson MS, Robertson AD, Macher I, & Raetz CRH (1988) Biosynthesis of lipid A in Escherichia coli: identification of UDP-3-O-[(R)-3-hydroxymyristoyl]-alpha-D-glucosamine as a precursor of UDP-N2,O3-bis[(R)-3-hydroxymyristoyl]-alpha-D-glucosamine. *Biochemistry* 27(6):1908-1917.

143. Young K, Silver LL, Bramhill D, Cameron P, Eveland SS, Raetz CRH, Hyland SA, & Anderson MS (1995) The envA permeability/cell division gene of Escherichia coli encodes the second enzyme of lipid A biosynthesis. UDP-3-O-(R-3-hydroxymyristoyl)-N-acetylglucosamine deacetylase. *J Biol Chem* 270(51):30384-30391.

144. Masoudi A, Raetz CRH, Zhou P, & Pemble CWt (2014) Chasing acyl carrier protein through a catalytic cycle of lipid A production. *Nature* 505(7483):422-426.

145. Jenkins RJ & Dotson GD (2012) Dual targeting antibacterial peptide inhibitor of early lipid A biosynthesis. *ACS Chem Biol* 7(7):1170-1177.

146. Joo SH, Chung HS, Raetz CRH, & Garrett TA (2012) Activity and crystal structure of Arabidopsis thaliana UDP-N-acetylglucosamine acyltransferase. *Biochemistry* 51(21):4322-4330.

Biography

S. Ali Masoudi was born December 31, 1983 in Tehran, Iran. After graduating from high school, he immigrated to the United States and attended University of Washington at Seattle, WA. Ali pursued an undergraduate research position in the lab of Dr. Miqin Zhang within the Material Science and Engineering department and worked on nanoparticle synthesis for specific cell-targeting applications. Ali graduated in 2007 with a Bachelor's of Science in Biochemistry and joined Seattle Biomedical Research Institute, where he was involved in production and purification of protein targets for Seattle Structural Genomic Center for Infectious Disease. In 2009, Ali matriculated in the Department of Biochemistry at Duke University, and joined the Raetz lab in March of 2010. His publications at Duke University include:

Masoudi A, Raetz CRH, Zhou P, Pemble IV CW. (2014) Chasing acyl carrier protein through a catalytic cycle of lipid A production. *Nature* **505**, *7483.*

Li Y, Powell DA, Shaffer SA, Rasko DA, Pelletier MR, Leszyk JD, Scott AJ, **Masoudi A**, Goodlett DR, Wang X, Raetz CRH, Ernst RK. (2012) LPS remodeling is an evolved survival strategy for bacteria. *Proc. Natl. Acad. Sci. USA* **109**, 8716.

Ingram BO, **Masoudi A**, Raetz CRH. (2010) *Escherichia coli* mutants that synthesize dephosphorylated lipid A molecules. *Biochemistry* **49**, 8325.